**Title**
Measurements of plasma bremsstrahlung and plasma energy density produced by electron cyclotron resonance ion source plasmas



**Author**
Noland, Jonathan David

**Publication Date**
2011

Peer reviewed|Thesis/dissertation

**Measurements of plasma bremsstrahlung and plasma energy density produced by electron cyclotron resonance ion source plasmas**

by

Jonathan David Noland

A dissertation submitted in partial satisfaction of the
requirements for the degree of
Doctor of Philosophy

in

Engineering-Applied Science and Technology

in the

Graduate Division
of the
University of California, Berkeley

Committee in charge:
Professor John Verboncoeur, Co-chair
Professor Michael Lieberman, Co-chair
Professor David Attwood
Professor Ka-Ngo Leung

Spring 2011

**Measurements of plasma bremsstrahlung and plasma energy density produced by electron cyclotron resonance ion source plasmas**

## Abstract

Measurements of plasma bremsstrahlung and plasma energy density produced by electron cyclotron resonance ion source plasmas

by

Jonathan David Noland
Doctor of Philosophy in Engineering-Applied Science and Technology

University of California, Berkeley

Professor John Verboncoeur, Co-chair

Professor Michael Lieberman, Co-chair

The goal of this dissertation was to gain an understanding on the relative importance of microwave power, neutral pressure, and magnetic field configuration on the behavior of the hot electrons within an Electron Cyclotron Resonance Ion Source (ECRIS) plasma. This was carried out through measurement of plasma bremsstrahlung with both NaI(Tl) ($h\nu > 30$ keV) and CdTe (2 keV $< h\nu <$ 70 keV) x-ray detectors, and through measurement of the plasma energy density with a diamagnetic loop placed around the plasma chamber. We also examined the anisotropy in x-ray power by simultaneously measuring the x-ray spectra in two orthogonal directions: radially and axially, using NaI(Tl) detectors.

We have seen that for a 6.4 GHz ECRIS, both the x-ray power produced by confined electrons and the plasma energy density behave logarithmically with microwave power. The x-ray flux created by electrons lost from the plasma, however, does not saturate. Thus, the small increase in plasma density that occurred at high microwave powers (> 150 W on a 6.4 GHz ECRIS) was accompanied by a large increase in total x-ray power. We suggest that the saturation of x-ray power and plasma energy density was due to rf-induced pitch-angle scattering of the electrons. X-ray power and plasma energy density were also shown to saturate with neutral pressure, and to increase nearly linearly as the gradient of the magnetic field in the resonance zone was decreased. All of these findings were in agreement with the theoretical models describing ECRIS plasmas.

We have discussed the use of a diamagnetic loop as a means of exploring various plasma time scales on a relative basis. Specifically, we focused much of our attention on studying how changing ion source parameters, such as microwave power and neutral pressure, would effect the rise and decay of the integrated diamagnetic signal, which can be related to plasma energy density. We showed that increasing microwave power lowers the e-fold times at both the leading edge and the trailing edge of the microwave pulse. Microwave power, however, had almost no impact on the ignition times of the plasma.

The plasma energy density e-fold times were insensitive to both neutral pressure and magnetic field setting. Neutral pressure, however, had a dramatic effect on the time of first appearance of the diamagnetic signal ("plasma ignition time"). In addition to neutral pressure,

ignition times were also a function the relative abundance of electrons in the plasma chamber at the beginning of a microwave pulse. In all instances, the rise time of the integrated diamagnetic signal was seen to be faster than the decay time.

By comparing the unintegrated diamagnetic signal to the ratio of reflected to forward microwave power we theorized that the initial, exponential rise in the diamagnetic signal at the leading edge of a microwave pulse was due to rapid changes in both the average electron energy and density. During the slowly decaying portion of the diamagnetic loop signal, only the hot tail of the electron population was increasing. This theory was supported by time resolved, low energy x-ray measurements that showed that the period of rapid change of the ratio of reflected to forward microwave power coincided with a rapid change in average photon energy.

We have also showed that x-rays production in an ECRIS plasma was highly anisotropic, with radial x-ray counts being much greater than axial x-ray counts. This was shown to be true for both the "ECR" (operating at 6.4 GHz) and the higher performance "AECR-U" (operating at 14 GHz). Based on this, we can make the qualitative statement that the electron energy was also highly anisotropic, with a much larger perpendicular energy than parallel energy. The degree of anisotropy was shown to increase with the operating frequency of the ion source. This increase was most likely attributable to the higher power density and greater confinement associated with higher performance machines, and implies that superconducting ECRIS operating at very high frequencies will have extremely anisotropic x-ray power deposition.

The radial spectral temperature on the "AECR-U" was over twice as large as the axial spectral temperature. However, in the "ECR" the radial and axial spectral temperatures were similar. Hence, the anisotropy in spectral temperature also showed dependence on the magnetic field strength and operating frequency of the ECRIS. The combination of higher energies, and intensity of high energy x-rays in the radial direction has important implications in the x-ray heat load estimates for superconducting ECR ion source cryostats.

To my parents. We finally have a “Dr.” in the family.

# Contents

**Bibliography** **102**

# List of Figures

# Acknowledgments

I would like to thank Prof. John Verboncoeur for giving me the opportunity to pursue a graduate degree, and for all of his guidance, humor, and support throughout.

I would like to thank Dr. Daniela Leitner for giving me the chance to work in the ECR ion source group at Lawrence Berkeley National Laboratory. Her guidance and patience were invaluable in becoming a better experimentalist.

I would like to also thank Dr. Michel Kireeff Covo for the countless hours he spent helping me setup the diamagnetic loop experiment.

Janilee Benitez and Markus Strohmeier both deserve my thanks for helping me tune the ion sources and for helping me set up my various experiments.

I owe much to the members of the Building 88 machine shop and electronics shop, without whose help I would have never finished my dissertation.

I owe a debt of gratitude to Dr. Olli Tarvainen, who, during a month long visit to Lawrence Berkeley National Laboratory, helped me obtain much of the data presented in this dissertation.

I would like to thank everyone at JYFL at the University of Jyvaskyla for hosting me twice over the course of my studies.

To anyone I may have forgotten, but that helped me along the way: Thank you!

Lastly, a great, big, huge thank you to my beautiful wife and daughter, Rieko and Nanami, for putting up with me for five years (or three years, in the case of my daughter) as I worked to complete my PhD, and providing me with so much love and happiness!

# Chapter 1

# Introduction

## 1.1 Background

Electron Cyclotron Resonance ion sources (ECRIS) are magnetized plasma ion sources used to produce multiply charged ions (MCI's)[16, 23]. Magnetic confinement of the plasma in modern ECRIS generally consists of a mirror field combined with a multipole (e.g., sextupole) field. A picture showing the magnet arrangement in a majority of ECRIS is shown in Fig. 1.1.1. Microwaves are injected into the plasma chamber, typically parallel to magnetic field lines, and in such a way that they are propagating from a region of high magnetic field strength into a region of lower magnetic field strength. Electrons move back and forth between mirror points along magnetic field lines, and absorb energy from the electromagnetic wave, whenever they are in a region where the local cyclotron frequency in the electrons frame of reference is equal to the microwave frequency and they are in correct phase with respect to the microwave electric field. MCI's are created as the cold, electrostatically confined electrons transition to higher energies through the ECR heating process. Higher and higher ionic charge states are created in a stepwise fashion through multiple collisions with energetic electrons.

The superposition of an axial magnetic mirror field and the sextupole field creates a "min-B" field that is resistant to interchange instabilities, and helps to improve plasma confinement[16]. The strength of the magnetic field increases in all directions from the center of the plasma chamber. Magnetic field lines in a min-B structure are open, while the mod-B surfaces are closed with an ellipsoidal shape.

The combination of low operating pressure (typically $10^{-7}$-$10^{-6}$ Torr) and the ECR heating process can allow a significant population of electrons within the plasma to reach very high energies. The presence of these high energy electrons causes an unfortunate side effect. Namely, ECRIS tend to emit large amounts of x-rays. The x-rays are created primarily in electron-ion collisions in the plasma, or when unconfined electrons strike the vacuum structure. Generally, in low density plasmas, such as ECR plasmas, the intensity of x-rays created by electron-wall collisions is orders of magnitude greater than that of x-rays created in the plasma volume[33].

The x-rays present hazards to personnel, and in the case of modern, superconducting ECRIS, can cause local heating of the superconducting magnets, which can lead to quenches. In addition, the x-rays are partially absorbed in the coldmass, which adds dynamic heat loads

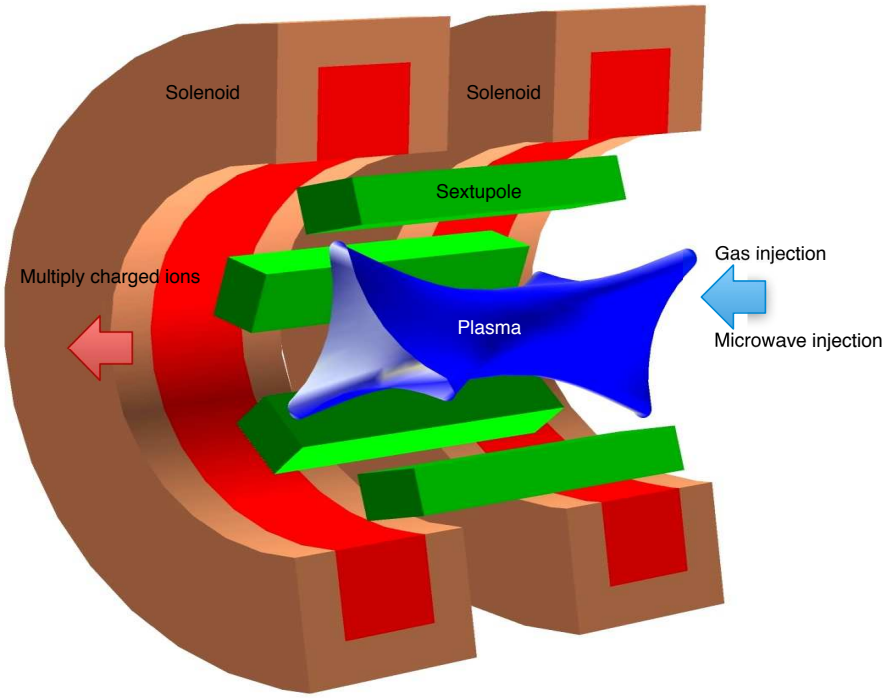


Figure 1.1.1: Typical magnet arrangement found in modern ECRIS.

of several watts to the cryostat. Experimental heat loads of more than 1 W per kW of input microwave power have been measured for 28 GHz ECRIS[34]. In order to adequately design the cyrostat for future ECRIS the heat load added by x-rays from the plasma needs to be better understood. To understand the production mechanisms of x-rays, one needs to understand the electron heating mechanism in ECR produced plasmas. Also, understanding how the axial and radial x-ray fluxes scale with microwave frequency and power is important for the design of future, superconducting ECRIS.

Two common, non-invasive, high temperature plasma diagnostics used to study high energy electrons are measurement of the plasma bremsstrahlung and measurement of the plasma diamagnetism with a diamagnetic loop. Plasma bremsstrahlung spectra can be used to estimate x-ray power, and to qualitatively learn about the distribution of electron energies in the plasma (a more quantitative distribution would require deconvolution of the recorded x-ray spectra). Plasma diamagnetism is related to the energy density of all charged particles in the plasma, with the largest contribution coming from the warm and hot electrons.

Measurements of plasma bremsstrahlung and the diamagnetic current in electron cyclotron resonance plasmas have been made as early as the late 1960's[12]. In that study, a hydrogen discharge was produced by pulsing (1 $\mu$sec) up to 100 kW of S-band power into a cylindrical conducting box. Plasma confinement was achieved with a magnetic mirror field. Two distinct modes of operation were observed. At low pressure ($< 10^{-4}$ Torr) the discharge was very unstable and x-ray flux was high. At higher pressure the discharge was observed to be very stable with an attendant decrease in x-ray flux. Plasma energy density, measured with a diamagnetic

loop, was estimated to have a decay time constant on the order of 100 $\mu$sec. Measurement of plasma bremsstrahlung has since become a standard way of characterizing ECR ion source plasmas.

An extensive set of plasma bremsstrahlung measurements was done by Bernhardi *et al.* [6, 7]in the late 1970's and early 1980's. In those studies up to 2.4 kW of 9.72 GHz microwaves were fed in radially into a copper resonator cavity. Heating could be made either continuous or pulsed. The magnetic field configuration was a simple mirror field, with no multipole field. Additionally, Bernhardi developed a method for the deconvolution of the recorded x-ray spectra in order to obtain the electron energy distribution function[5]. Measurements of x-rays in the radial and axial directions showed the the count rate of detected x-rays radially were larger than those axially. The hot electron population was also observed to depend on the neutral pressure, and its density increased with decreasing pressure. It was also observed that the slope of the x-ray spectra was insensitive to further increases of microwave power at microwave powers above 1 kW.

More recently, time resolved measurements of high energy x-rays produced by ECRIS were made by Ropponen *et al*. [42, 43, 44]. In those studies the effects of magnetic field strength, neutral pressure, microwave power, and microwave pulse pattern on production of x-rays were examined. The neutral pressure was observed to affect the time at which bremsstrahlung emission began, with higher neutral pressures leading to faster times. Microwave power and magnetic field strength, however, were shown to have little effect on the timescale of high energy x-ray production. The time to reach steady values of x-ray counts changed little with neutral pressure, microwave power, and magnetic field strength. The type of gas used, though, was shown to change the timescale for reaching steady state significantly.

Measurements of the plasma diamagnetism, as well as bremsstrahlung, in an ECRIS was performed by Barue *et al.* [3, 4]. The plasma energy density, based on the diamagnetic signal, was shown to increase continuously from a microwave power of 100 W to 1000 W. Conversely, the time for the diamagnetic signal to decay was shown to decrease as the microwave power was increased.

## 1.2 Description of ion sources used for this dissertation

The majority of the data that is presented in this dissertation was taken on two ion sources at Lawrence Berkeley National Laboratory (LBNL): the 6.4 GHz ECR and the 14 GHz Advanced Electron Cyclotron Source-Upgraded (AECR-U). Operational parameters of these sources are given in Table 1.1 and Table 1.2.

The ECR[37] uses Nd-Fe permanent magnets, arranged in a sextupole structure, and solenoid coils for confinement of the plasma. Energy is added to the plasma electrons by injecting between 200 - 600 W of 6.4 GHz microwaves into the main plasma chamber, parallel to the source axis. The plasma chamber is approximately 40 cm in length by 9 cm in diameter. Typical operating neutral pressures in the plasma chamber are in the $10^{-7}$-$10^{-6}$ Torr range. The source is usually run at an extraction voltage of 10 kV. The ECR uses a small injection stage. The plasma created in this stage diffuses into the primary chamber, and thus helps to initiate and sustain the

| | |
|---|---|
| Heating frequency | 6.4 GHz |
| Power level | 200-600 W |
| Chamber volume | 360 $cm^3$ |
| Operating pressure | $10^{-7}$-$10^{-6}$ Torr |
| Extraction voltage | 10 kV |
| Axial field | 0.48 T (injection) and 0.35 T (extraction) |
| Radial field | 0.4 T at inner surface of plasma chamber |
| Resonance field | 0.229 T |

Table 1.1: Summary of ECR operating parameters.

| | |
|---|---|
| Heating frequency | 14.3 GHz and 10.75-12.75 GHz |
| Power level | up to 1.2 kW at 14.3 GHz |
| Chamber volume | 228 $cm^3$ |
| Operating pressure | $10^{-8}$-$10^{-7}$ Torr |
| Extraction voltage | 12 kV |
| Axial field | 1.5 T (injection) and 1.0 T (extraction) |
| Radial field | 0.75 T at inner surface of plasma chamber |
| Resonance field | 0.511 T (14.3 GHz) |

Table 1.2: Summary of AECR-U operating parameters.

main stage plasma. It has been shown previously [15] that the injection stage plasma primarily provides cold electrons to the main stage plasma, which enhances ion confinement time. Thus, modern ECRIS, such as the AECR-U, have replaced the injection stage with a "bias disk," which is simply an electrode that is biased negatively relative to the plasma source potential. Low energy, secondary electrons are created as plasma particles collide with the bias disk. It is mainly the low energy electrons that are needed, and hence, one could replace the first stage with any source of low energy electrons, such as an electron gun[55].

The AECR-U[54], a diagram of which is shown in Fig. 1.2.1, is a second generation ECRIS. This source can operate with microwave frequencies of 10.4 GHz, 10.75 - 12.75 GHz using a travelling wave tube amplifier, and 14.3 GHz. The magnetic field is, again, a superposition of an axial field, created by a pair of solenoids, and a radial field, created by a NdFeB permanent magnet sextupole. The maximum axial field at the injection side is approximately 1.5 T and 1.0 T at the extraction side. The radial field has a magnitude of approximately 0.75 T at the inner surface of the plasma chamber. Operating pressures in the AECR-U are typcially in the $10^{-8}$-$10^{-7}$ Torr range. Over 1 kW of 14.3 GHz microwave power can be injected into the plasma chamber.

Both the ECR and AECR-U have a similar beam line and analyzing system (Fig. 1.2.2). Following extraction from the plasma chamber, the ions pass through a Glaser magnet that focuses the beam through a set of slits into a Faraday cup. A set of attenuators follows the Faraday cup. Next, the ions pass through a 90-degree bend magnet that analyzes and refocuses

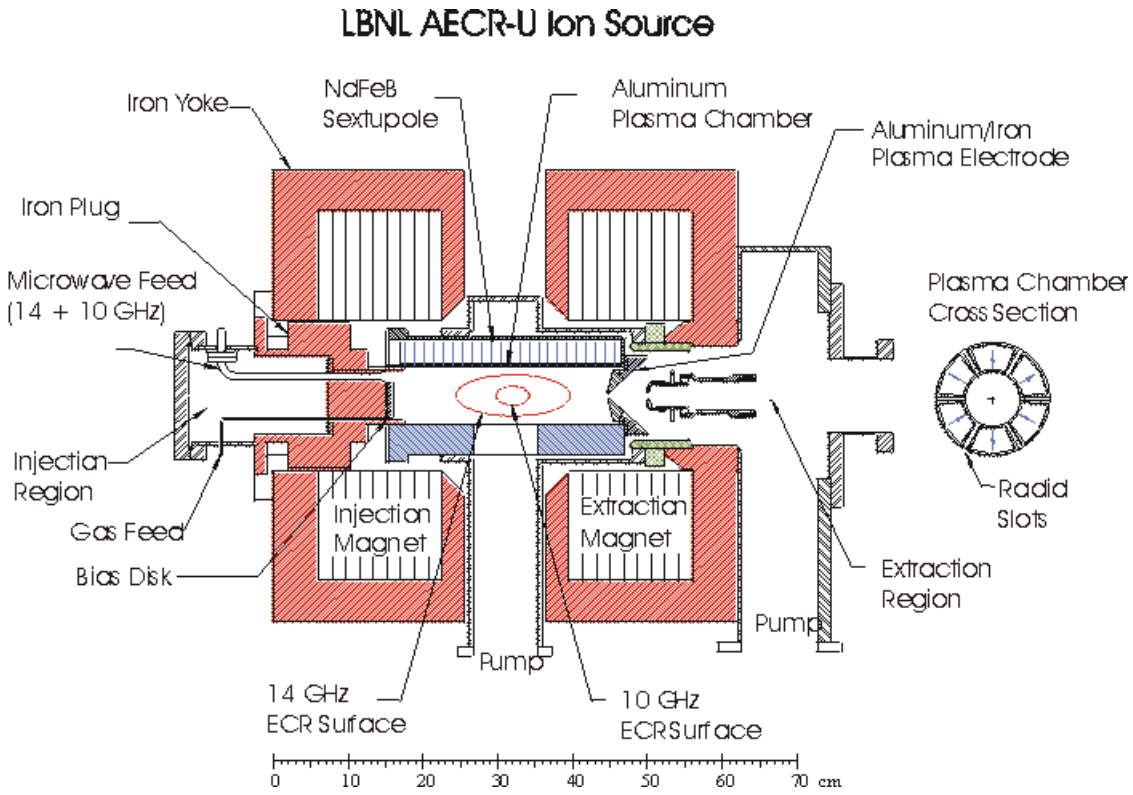


Figure 1.2.1: Diagram of the LBNL AECR-U ECRIS.

the beam through a second set of slits into the second Faraday cup. It is this second Faraday cup that we use to record the currents of various ionic species.

## 1.3 Purpose of dissertation

The original goal of this work was to explore the scaling of x-ray energies and intensities with microwave frequency on ECRIS operating within a frequency range of 6.4 GHz to 28 GHz. This goal was not entirely met because of the lack of availability of the highest performance ECRIS, that operates at frequencies of 18 GHz and 28 GHz. We were, however, able to measure plasma bremsstrahlung on the 6.4 GHz ECR and the 14 GHz AECR-U, and a comparison between these sources is discussed in Chapter 5.

Instead, this dissertation has evolved into an examination of how ion source settings such as microwave power, neutral pressure, and magnetic field setting affect the x-ray spectra, x-ray power anisotropy, and the plasma energy density. The analysis is qualitative and focuses on the comparison of different data points in an effort to discover trends. In the limited time frame it was not possible to calculate an exact plasma density or to determine a precise electron energy distribution function (although having precise estimates for these would be quite valuable, of course).

The main focus of this work was placed on understanding how the high energy electron

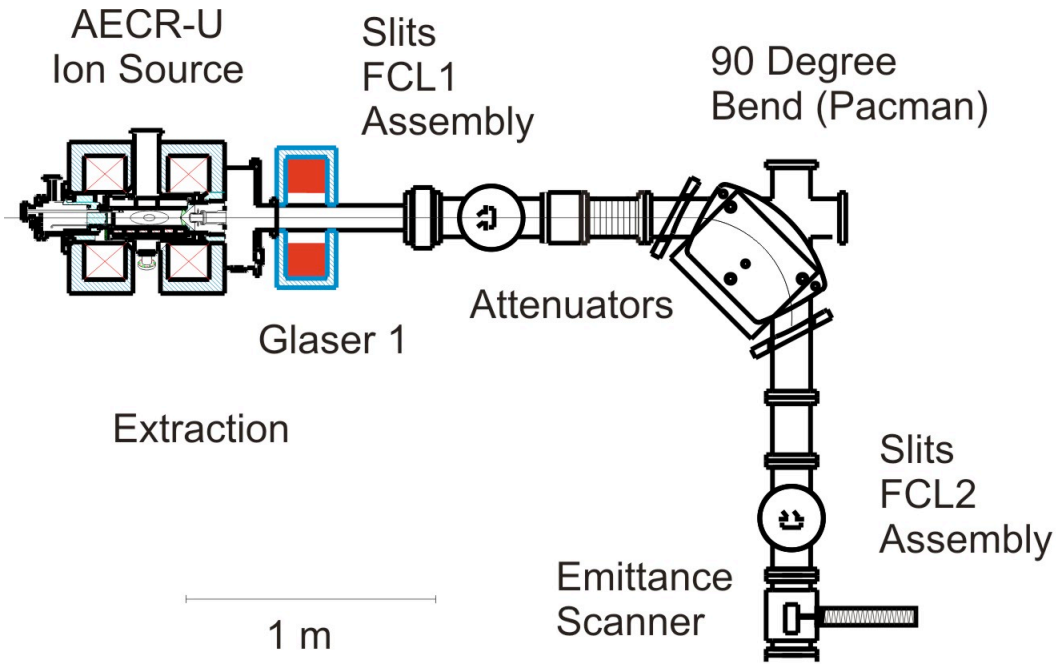


Figure 1.2.2: AECR-U beamline (ECR beamline is similar).

population, which is responsible for the creation of x-rays, responds to changes in microwave power, neutral pressure, and magnetic field setting. The electron energy distribution function (EEDF) is related to the recorded x-ray spectra through bremsstrahlung cross sections and detector response functions. Without a full deconvolution of the recorded x-ray spectra to remove the effects of the detector and cross sections, we cannot give quantitative results. However, even if we did perform the deconvolution, the results may still be of limited usefulness[11]. Regardless, we can still make qualitative statements about how the relative population of electrons may change in response to changes in ion source settings, and this is still worthwhile.

As mentioned earlier, both diamagnetic loop measurements and plasma bremsstrahlung measurements have been made previously by other researchers, so development and application of those diagnostics does not represent an original contribution to field of ECRIS plasma physics. However, this is the first time that both low energy x-ray measurements and diamagnetic loop measurements have been carried out simultaneously on a 6.4 GHz min-B ECR ion source. Hence, it represents a useful data point for qualitative comparison to the many x-ray measurements carried out on both lower and higher frequency sources (for example[12, 4, 29, 34]), as well as to the diamagnetic loop measurements that were performed on an 18 GHz ECRIS[4].

Moreover, we present for the first time a comparison of both radial and axial x-ray power produced by two ECRIS, one operating at 6.4 GHz and the other at 14 GHz. Typically, x-ray measurements are taken from one direction (usually axially, because radial access is often limited). Both the LBNL ECR and AECR-U allow access to the plasma in both the radial and axial directions, and hence, we were provided with a unique opportunity to study how the driving frequency affects the anisotropy in radial and axial x-ray power in min-B ECR ion

sources.

## 1.4 Outline of dissertation

This dissertation is divided into four major chapters. In Chapter 2 we provide a brief, theoretical background to familiarize the reader with important concepts that are useful in understanding the experimental results in later chapters. The chapter will discuss topics such as fundamental time and length scales in plasmas, single particle motion in a magnetic mirror, and power absorption in an ECR plasma. The next three chapters present both the various experimental setups and the results of the experiments, and constitute the bulk of the dissertation. In Chapter 3 measurements of low energy x-rays and plasma diamagnetism taken on the 6.4 GHz ECR are presented with an emphasis on an observed saturation of x-ray power and plasma energy density with microwave power. Chapter 4 uses the diamagnetic loop measurements to examine how ion source settings affect the formation and decay of the plasma energy density, we compare Argon and Helium ion timescales to the diamagnetic loop signal, and we compare the diamagnetic loop signal to a measurement of reflected microwave power. Differences in axial and radial x-ray production on the 6.4 GHz ECR and 14 GHz AECR-U are discussed in Chapter 5. Finally, some general conclusions are discussed and suggestions for future work are given in Chapter 6.

## 1.5 Published articles

The following publications were completed as part of this dissertation work:

1. Journal articles (refereed):

   (a) J. Noland, O. Tarvainen, J. Benitez, D. Leitner, C. Lyneis and J. Verboncoeur, "Studies of electron heating on a 6.4 GHz ECR ion source through measurment of diamagnetic current and plasma bremsstrahlung," submitted to *Plasma Sources Science and Technology.*

   (b) J. Noland, J. Benitez, M. Kireeff Covo, D. Leitner, O. Tarvainen, and J. Verboncoeur, "Measurement of the diamagnetic current and low energy x-ray spectra on a 6.4 GHz ECR ion source," submitted to *Journal of Instrumentation*.

   (c) T. Ropponen, O. Tarvainen, G. Machicoane, D. Leitner, J. Noland, V. Toivanen, H. Koivisto, T. Kalvas, P. Peura, P. Jones, I. Izotov, V. Skalyga and V. Zorin, "Studies of plasma breakdown and electron heating on a 14 GHz ECR ion source through measurement of plasma bremsstrahlung," to be submitted to *Plasma Sources Science and Technology.*

2. Conference proceedings (refereed):

(a) J. Noland, J. Y. Benitez, D. Leitner, C. Lyneis and J. Verboncoeur, "Measurement of radial and axial high energy x-ray spectra in electron cyclotron resonance ion source plasmas," *Review of Scientific Instruments* (2010), pp. 02A308

(b) T. Ropponen, O. Tarvainen, V. Toivanen, P. Peura, P. Jones, T. Kalvas, H. Koivisto, J. Noland, and D. Leitner, "The effect of rf pulse pattern on bremsstrahlung and ion current time evolution of an ecris," *Review of Scientific Instruments* (2010), pp. 02A302

(c) O. Tarvainen, T. Ropponen, T. Thuillier, J. Noland, V. Toivanen, T. Kalvas, and H. Koivisto, "The role of seed electrons on the plasma breakdown and preglow of electron cyclotron resonance ion source," *Review of Scientific Instruments* (2010), pp. 02A303

3. Conference proceedings (non-refereed):

(a) J. Noland, J. Benitez, M. Kireeff Covo, D. Leitner, C. Lyneis, O. Tarvainen, and J. Verboncoeur, "Measurement of the diamagnetic current on the LBNL 6.4 GHz ECR ion source," in Proceedings of the l9th International Workshop on ECR Ion Sources, 2010.

(b) J. Y. Benitez, J.D. Noland, D. Leitner, C. Lyneis, D.S. Todd, and J. Verboncoeur, "High energy component of x-ray spectra in ECR ion sources," in Proceedings of the 18th International Workshop on ECR Ion Sources, 2008.

# Chapter 2

# Theoretical considerations

The purpose of this chapter is not to give a rigorous theoretical explanation of the physics associated with ECRIS plasmas. We wish to familiarize the reader with concepts and parameters that are important in trying to understand the experimental results discussed later in this dissertation. In this chapter we briefly discuss basic plasma theory and the theory of electron heating in an ECR plasma. We begin with a description of important, fundamental time and length scales in a plasma, and then move on to a discussion of ECR heating, magnetic mirrors, and plasma particle and power balance. This discussion is followed with a description of a simple, single particle ECR heating model in Section 2.2. We conclude with a short examination of physics involved in production of photons in a Coulomb collision between two charged particles in Section 2.3.

## 2.1 Important concepts in ECR plasma physics

### 2.1.1 Fundamental time and length scales

A plasma can be loosely defined as a collection of charged particles. Non-neutral plasmas consist of particles of a single charge type, either positive or negative. Neutral plasmas, on the other hand, consist of both positive and negative charges. In a stricter sense, a plasma is defined as an electrically quasi-neutral collection of charged particles that is subject to collective effects. By "electrically quasi-neutral," we mean that number densities of electrons and ions are approximately equal: $n_e \approx \sum_s Z_s n_{i_s}$, where $Z$ is the average charge state of ionic species $s$. "Collective effects" implies that each charged particle in a plasma is influenced by many nearby charged particles. The time scale and length scale that predict the importance of collective effects is defined by the plasma frequency and the Debye length, respectively.

The fundamental time scale in a plasma is the plasma frequency. The plasma frequency describes the frequency at which a given species will oscillate at after being perturbed by some external force which causes charge separation. If we consider the response of the plasma as a

whole (including all species), we may write the plasma frequency as:

$$\omega_P^2 = \sum_s \frac{e^2 n_s}{m_s \varepsilon_0}, \tag{2.1.1}$$

where $e$ is the charge of an electron, $n_s$ is the number density (number of particles per unit volume) of the species, $m_s$ is the mass of an individual particle of species $s$, and the sum is over all species present in the plasma. We see that the plasma frequency is essentially proportional to the square root of the density of the plasma. In a plasma consisting of electrons and one species of ion, we can write the plasma frequency as:

$$\omega_P = \left(\omega_{P_e}^2 + \omega_{P_i}^2\right)^{1/2}. \tag{2.1.2}$$

Because the mass of an ion is much larger than the mass of an electron ($m_i/m_e \sim 10,000$), Eq. 2.1.2 can be approximated as $\omega_P \approx \omega_{P_e}$. That is, when we speak of plasma frequency, we generally imply electron plasma frequency. For timescales on the order of a plasma period or less we cannot assume that that electrical neutrality will hold.

The fundamental length scale in a plasma is the Debye length. The electron and ion Debye lengths can be written:

$$\lambda_{D_{e,i}} = \sqrt{\frac{\varepsilon_0 T_{e,i}}{n_0 e^2}}, \tag{2.1.3}$$

where $n_0$ is the plasma number density. If the electron temperature is much greater than the ion temperature, as is typically the case in ECRIS, then the Debye length is approximated as the electron Debyle length in Eq. 2.1.3. The Debye length is independent of particle mass, but depends on both plasma temperature and density. We can think of the Debye length as a characteristic length scale over which the requirement for electrical neutrality is not satisfied. In other words, the distance over which significant electric fields can exist in the plasma. The Debye length is related to the plasma frequency as follows:

$$\lambda_D \omega_P = \sqrt{\frac{k_B T}{m}}. \tag{2.1.4}$$

Collective effects are important if $L >> \lambda_D$ and $\tau >> \tau_P$, where L is the characteristic length scale, and $\tau$ is the characteristic time scale of the system being considered.

The plasma parameter, $\Lambda$, describes the number of particles contained a sphere of radius equal to the Debye length:

$$\Lambda = \frac{4}{3}\pi n_0 \lambda_D^3. \tag{2.1.5}$$

The magnitude of $\Lambda$ determines the relative importance of particle kinetic energy and interparticle potential energy. In general, typical plasmas are dominated by kinetic energy.

In a magnetized plasma, two other parameters become important: the cyclotron frequency and the plasma beta. Charged particles orbit around field lines at the cyclotron frequency. The

magnitude of this frequency is given by:

$$\omega_c = \frac{|q|B}{m}, \tag{2.1.6}$$

where $q$ is the charge of the particle. This equation shows that the cyclotron frequency is directly proportional to the magnitude of the magnetic field and particle charge, and inversely proportional to the mass of the particle. Electron cyclotron frequencies are typically in the GHz range, while ion cyclotron frequencies tend to be in the MHz range. If the electrons in the plasma are relativistic then Eq. 2.1.6 is written:

$$\omega_c = \frac{|q|B}{m\gamma}, \tag{2.1.7}$$

where $\gamma$ is the Lorentz factor given by:

$$\gamma = \frac{1}{\sqrt{1 - v^2/c^2}}.$$

The plasma beta defines the relative importance of plasma kinetic energy density to magnetic energy density:

$$\beta_s = \frac{n_s k_B T_s}{B^2/2\mu_0}. \tag{2.1.8}$$

A different $\beta$ is defined for each species, $s$, present in the plasma, and the total $\beta$ is simply the sum.

We can estimate the magnitude of some of these parameters in an ECRIS plasma if we assume values for quantities like electron number density and temperture. For example, if the electron number density is in the range of $10^9$-$10^{11}$ cm$^{-3}$, and we use the resonant magnetic field strength of 0.23 T (corresponding to 6.4 GHz), then the electron cyclotron frequency, $f_{ce}$, is approximately 6 GHz, while the electron plasma frequency, $f_e$, is between 0.3 GHz and 3 GHz. For a plasma with a temperature of 1 keV and a plasma density, again, in the range of $10^9$-$10^{11}$ cm$^{-3}$, the electron Debye length is between 7.4 mm to 0.74 mm, both well below the size of the plasma chamber in the ECR and AECR-U.

### 2.1.2 Collisions

#### Fully ionized plasma

In a fully ionized plasma collisions can occur between electrons, ions, and between electrons and ions. The collisions are long-range (interactions occur on length scales greater than an atomic radius) because of the Coulomb force. Each charged particle is interacting with many other charged particles within a Debye length. Plasmas are dominated by small angle collisions, i.e., collisions that cause a change in the particles direction of less than 90 degrees. The large difference in mass between electrons and ions can cause each species to have very different collision frequencies. Estimates for the collision frequencies in a fully ionized plasma

are given in the following equations[19]:

$$\langle \nu_{ei} \rangle = \frac{\sqrt{2} n_i Z^2 e^4 ln\Lambda}{12\pi^{3/2}\varepsilon_0^2 \sqrt{m} T_e^{3/2}} \tag{2.1.9}$$

$$\langle \nu_{ee} \rangle = \frac{\langle \nu_{ei} \rangle}{n_i Z^2 / n_e} \tag{2.1.10}$$

$$\langle \nu_{ii} \rangle = \frac{n_i Z^4 e^4 ln\Lambda}{12\pi^{3/2}\varepsilon_0^2 \sqrt{M} T_i^{3/2}}. \tag{2.1.11}$$

Here $\langle \nu_{ei} \rangle$ is the average collision frequency of electrons off of ions, $\langle \nu_{ee} \rangle$ is the average collision frequency of electrons off of other electrons, and $\langle \nu_{ii} \rangle$ is the average collision frequency of ions off of other ions (the temperatures in these equations must expressed in Joules). Examination of the above equations shows that collision frequency varies as $T^{-3/2}$. In hot, fully ionized plasmas collisional phenomena may occur relatively slowly, and because of this they are often not in thermal equilibrium. In partially ionized plasmas, discussed below, individual species are also often not equilibrium, depending now, not only on the Coulomb collision rate but also the collision rate with neutrals.

In a hydrogen plasma Eq. 2.1.9 can be approximated[19]:

$$\langle \nu_{ei} \rangle \sim 5 \times 10^{-11} \frac{n}{T_e^{3/2}}, \tag{2.1.12}$$

where $n$ is the plasma number density in particles per cubic meter, and $T_e$ is the electron temperature in eV. Using Eq. 2.1.12, we can estimate collisional times in a typical ECRIS hydrogen plasma for the hot electrons. Hence, for a plasma density in the range $10^9$-$10^{11}$ cm$^{-3}$and an electron temperature of 1 keV the electron-ion collisional time is on the order of 1 Hz to 100 Hz. The electron cyclotron frequencies are typically on the order of GHz in modern ECRIS, and so, even for plasmas with many different ionic charge states, the hot electron population can be considered nearly collisionless ($f_{ce} \gg \nu_{ei}$).

**Partially ionized plasma**

In addition to Coulomb collisions, in a partially ionized plasma collisions between neutrals and charged particles are also important . Collisions are categorized as either elastic (no change in internal energy of the neutral) or inelastic. Examples of inelastic collisions include ionization and excitation. The collision frequency is defined simply as:

$$\nu = n_g \sigma v, \tag{2.1.13}$$

where $n_g$ is the number density of "target" particles, $\sigma$ is the cross section of a particular interaction, and $v$ is the velocity of a monoenergetic beam of projectile particles. The nontrivial part of calculating the collision frequency is determination of the cross section. For

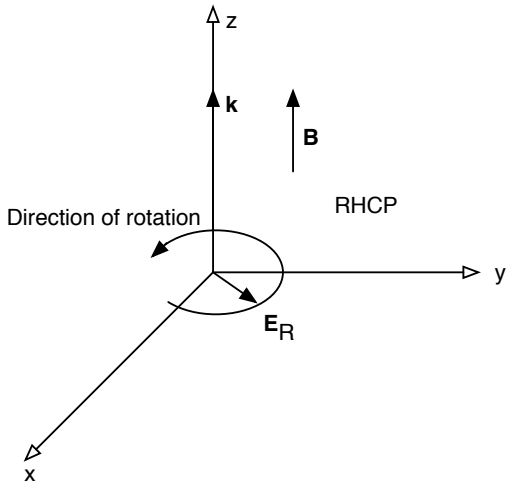


Figure 2.1.1: Illustration indicating direction of rotation for a RHCP electromagnetic wave.

ionization at high energy, the Thomson cross section is often used:

$$\sigma_{iz} = \pi \left( \frac{e}{4\pi\varepsilon_0} \right)^2 \frac{1}{\varepsilon} \left( \frac{1}{\varepsilon_{iz}} - \frac{1}{\varepsilon} \right). \tag{2.1.14}$$

The Thomson cross section has a maximum at approximately $2\varepsilon_{iz}$, and falls off as $1/\varepsilon$ for $\varepsilon \gg \varepsilon_{iz}$. Very high energy electrons, therefore, participate rarely in ionization events.

### 2.1.3 Electron cyclotron heating

When the cyclotron frequency, Eq. 2.1.6, of a charged particle is equal to the frequency of the injected right hand circularly polarized electromagnetic wave, energy is added to the particle in a resonant fashion. As long as an electron or ion remains in a region where $\omega_{ce} = \omega$, energy can be continually gained by the particle. Because we are interested in adding energy only to the electrons in ECRIS plasmas, the frequency of the electromagnetic waves used is typically GHz.

There are a large number of possible waves that can propagate in a plasma, indeed, whole books have been written on this topic[47]. We focus our attention on only one of these waves, the "R-wave." For propagation of an electromagnetic wave such that its wave vector, $\mathbf{k}$, is parallel to the magnetic field the following dispersion relationship can be derived[9]:

$$n^2 = \frac{c^2 k^2}{\omega^2} = 1 - \frac{\omega_P^2/\omega^2}{1 - (\omega_c/\omega)}. \tag{2.1.15}$$

The "R-wave" is named as such because it has right hand circular polarization (RHCP), i.e., its electric field rotates in a clockwise direction when viewed along the direction of the magnetic field (Fig. 2.1.1). From Eq.2.1.15 we see that the wave number, $k$, becomes infinite when $\omega_c =$

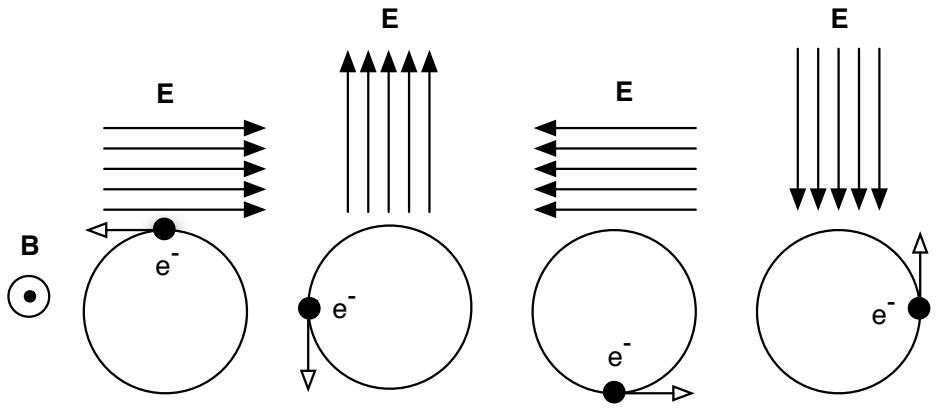


Figure 2.1.2: ECR heating. Interaction of an electron with RHCP wave.

$\omega$, corresponding to a resonance point (in actuality, the wave is damped near the resonance point, but Eq. 2.1.15 is derived assuming a cold plasma, and thus does not take damping into account). Because electrons rotate around magnetic field lines in the same direction as the electric field vector, it is possible for electrons to absorb energy from the wave, so long as the condition for resonance is met. It is possible for an electron to gain net energy outside of resonance so long as $\mathbf{F} \cdot \mathbf{v}$ is positive ($\mathbf{F}$ is the net force acting on the particle, and $\mathbf{v}$ is the electron velocity). The basic principle of ECR heating is illustrated in Fig. 2.1.2. An electron interacting with a wave that has left hand circular polarization (LHCP) would be alternately accelerated and decelerated, and so it would not gain energy.

We can estimate the average energy gained by an electron as it passes through the resonance zone with the following equation[36]:

$$W_{ecr} = \frac{\pi e^2 E_r^2}{m\omega\,|\alpha|\,v_{res}}, \tag{2.1.16}$$

where $E_r$ is the magnitude of the RHCP wave, $v_{res}$ is the parallel speed of the electron at resonance, and

$$\alpha = \frac{1}{\omega_c}\left(\frac{\partial \omega_c}{\partial z'}\right)_{res}. \tag{2.1.17}$$

Because the cyclotron frequency is directly proportional to the strength of the magnetic field, $\alpha$, in Eq. 2.1.17 is proportional to the gradient of the magnetic field in the resonance zone. From Eq. 2.1.16 we see that increasing the strength of the electric field increases the average energy gained. On the other hand, increasing the wave frequency, the slope in the resonance zone, or the velocity of the electron at the resonance point all lead to a decrease in the average energy gained.

According to the simple model given above, the velocity of the electron is increased primarily in a direction perpendicular to the local magnetic field. It is possible that the microwave power can be coupled into an electron parallel velocity through collisions. However, as the velocity of the particle becomes larger and larger, this becomes increasingly unlikely. As a

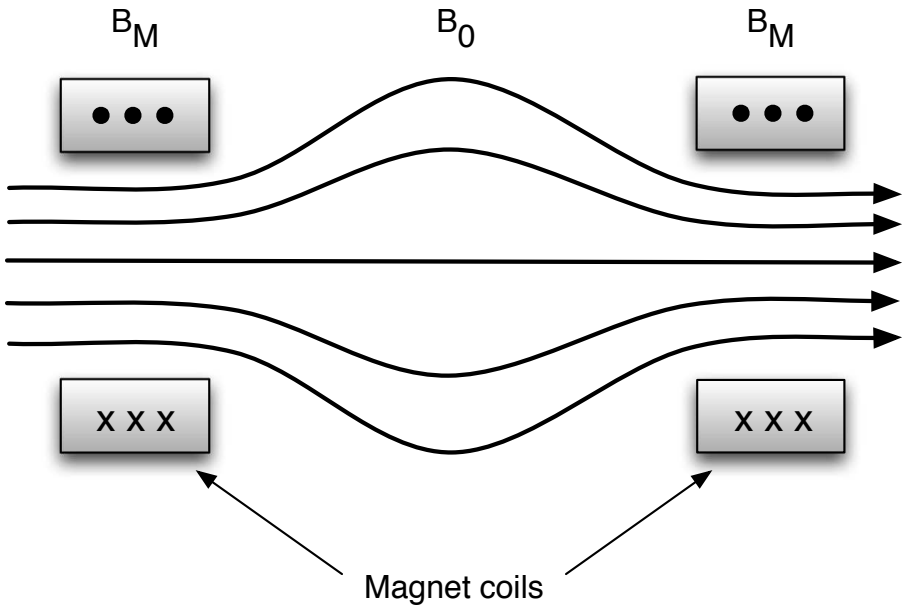


Figure 2.1.3: Magnetic mirror field lines.

particles velocity is increased, the cross section for a 90 degree (from perpendicular to parallel) change in momentum varies as $1/v^4$[36].

### 2.1.4 Particle confinement in a mirror field

A simple plasma confinement scheme, used in early fusion devices, is the "magnetic mirror." In practice, a magnetic mirror can be created by using two solenoid coils separated axially by some distance, as shown in Fig. 2.1.3. The field strength has maxima, $B_M$, in the vicinity of the coils, and a minimum, $B_0$, near the axial center point, between the coils.

The equation of motion for a non-relativistic charged particle moving in a static magnetic field is:

$$\mathbf{F} = m\frac{d\mathbf{v}}{dt} = q\mathbf{v}\times\mathbf{B}, \tag{2.1.18}$$

where $\mathbf{v}$ is the velocity vector of the particle and $\mathbf{B}$ is the magnetic field vector. In cylindrical coordinates this is written in component form as:

$$F_r = qv_\phi B_z \tag{2.1.19}$$
$$F_\phi = -qv_r B_z + qv_z B_r \tag{2.1.20}$$
$$F_z = -qv_\phi B_r. \tag{2.1.21}$$

In the case of the simple mirror field shown in Fig. 2.1.3, $B_\phi$ is zero, and terms that included this quantity have been dropped. Equation 2.1.19 and the first term on the right hand side of Eq. 2.1.20 cause charge particles to rotate around the axial magnetic field component. We can determine $B_r$ knowing that the divergence of the magnetic field must be zero, i.e., $\nabla\cdot\mathbf{B} = 0$. In

cylindrical coordinates the divergence equation is:

$$\frac{1}{r}\frac{\partial}{\partial r}(rB_r)+\frac{1}{r}\frac{\partial B_\phi}{\partial \phi}+\frac{\partial B_z}{\partial z}=0. \tag{2.1.22}$$

The middle term on the left hand side of Eq. 2.1.22 is equal to zero if we assume the magnetic field is axisymmetric, leaving:

$$\frac{1}{r}\frac{\partial}{\partial r}(rB_r)+\frac{\partial B_z}{\partial z}=0. \tag{2.1.23}$$

Integration of this equation with respect to the variable $r$, assuming that $\partial B_z/\partial z$ does not vary rapidly with $r$, yields:

$$B_r \approx -\frac{r}{2}\frac{\partial B_z}{\partial z}. \tag{2.1.24}$$

Substitution of Eq. 2.1.24 into Eq. 2.1.21 gives:

$$F_z=\frac{qv_\phi r}{2}\frac{\partial B_z}{\partial z}. \tag{2.1.25}$$

Often we are only interested in the motion of the guiding center of the particle, and not its detailed motion. If we average Eq. 2.1.25 over a gyro-orbit we obtain an equation for the average force acting on a charged particle:

$$F_z=-\frac{1}{2}\frac{mv_\perp^2}{B}\frac{\partial B_z}{\partial z}, \tag{2.1.26}$$

where $v_\perp$ is the speed of the particle perpendicular to the local direction of the magnetic field. Equation 2.1.26 shows that an axial force exists as long as the charged particle has a component of velocity in the perpendicular direction, and the charged particle is in a region with a magnetic field gradient. The force acts to push charged particles into regions of lower magnetic field strength, regardless of particle charge, and hence, acts to confine both electrons and ions. This confinement, though, is not perfect.

The quantity:

$$\mu=\frac{\frac{1}{2}mv_\perp^2}{B} \tag{2.1.27}$$

is the magnetic moment of the particle. The magnetic moment can be shown to be an invariant of motion as long as the magnetic field does not change significantly over one gyro-orbit. We can use the magnetic moment's property of invariance to define a "loss cone" for a given magnetic mirror field configuration. With reference to Fig. 2.1.3, we can write:

$$\frac{\frac{1}{2}mv_{\perp 0}^2}{B_0}=\frac{\frac{1}{2}mv_{\perp M}^2}{B_M}. \tag{2.1.28}$$

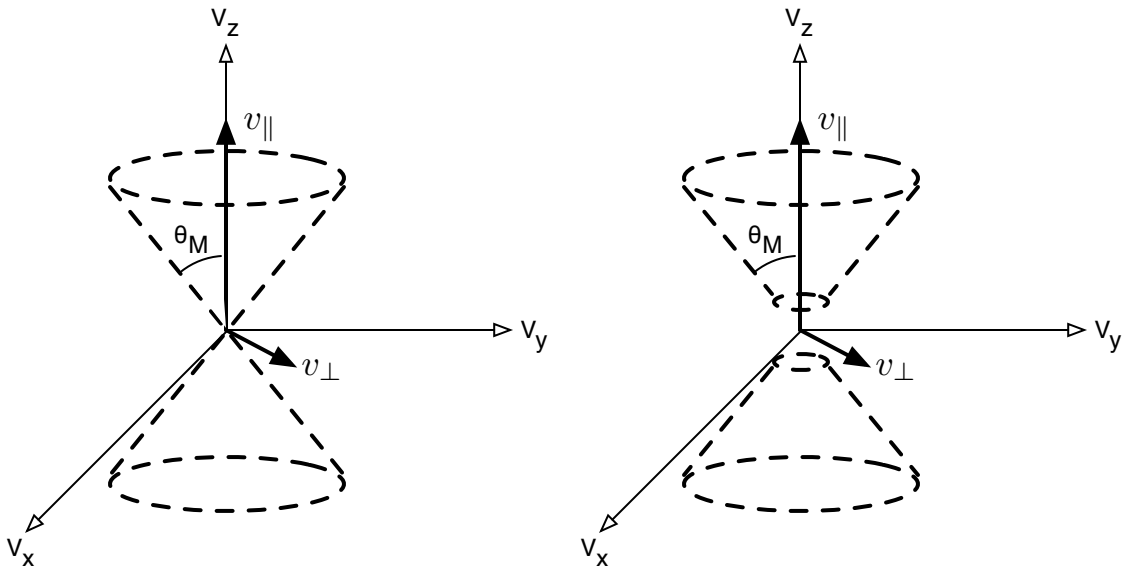


Figure 2.1.4: Left: loss cone. Right: loss cone in ECRIS plasma.

We will also need the following two equations:

$$\begin{aligned} sin^2\theta &= \frac{v_\perp^2}{v^2} \\ v^2 &= v_\perp^2 + v_{\parallel.}^2 \end{aligned}$$

Substitution of the above equations into Eq. 2.1.28 gives:

$$sin^2\theta_M = \frac{B_0}{B_M} = \frac{1}{R_M}, \tag{2.1.29}$$

where $R_M$ is defined as the mirror ratio. Equation 2.1.29 describes the loss cone in velocity space, given values of $B_0$ and $B_M$. Particles with a pitch angle, $\theta$, at the midpoint of the mirror that is smaller than $\theta_M$ will be within the loss cone (Fig. 2.1.4), and will be lost from the plasma. Essentially, charged particles with a large parallel velocity (i.e., a small pitch angle) will have enough parallel kinetic energy to overcome the force given in Eq. 2.1.26, and will be able to escape confinement.

In the absence of collisions, both ions and electrons will bounce back and forth between mirror points indefinitely, as long as they are located outside of the loss cone. With collisions, particles can be scattered into the loss cone if their pitch angle is decreased too much during an interaction. Low energy electrons, with their large collision frequency, tend to be lost at a faster rate than ions

In an ECR plasma, electrons that are just inside the velocity space loss cone can be moved out of it through the ECR heating mechanism. This is because ECR heating primarily increases the perpendicular component of an electrons kinetic energy, and so the ratio of $v_\perp^2/v^2$

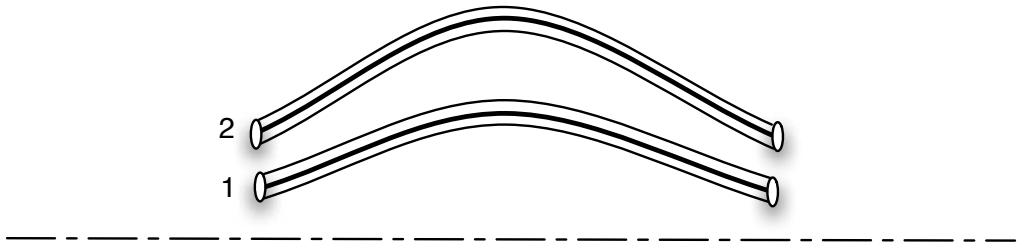


Figure 2.1.5: Neighboring flux tubes.

will increase, which, in turn, will cause $\theta$ to become larger than $\theta_M$. Additionally, low energy electrons are confined because the plasma potential, which was experimentally found to be on the order of 40 to 50 V for an oxygen plasma[51], is positive with respect to the chamber walls. Hence, the simple loss cone shown on the left of Fig. 2.1.4 is modified somewhat in an ECRIS plasma. As shown on the right hand side of Fig. 2.1.4, a small volume of the loss cone, near the origin, corresponding to electrons of low energy, is removed.

### 2.1.5 Instability of the simple mirror field

A simple mirror field is subject to a plasma magnetohydrodynamic (MHD) instability known as an "interchange instability." One requirement for a plasma to be MHD stable is[39]:

$$\delta W_p = \delta V \delta P > 0. \tag{2.1.30}$$

Here $\delta W_p$ is a small change in internal plasma energy due to some disturbance, $\delta V$ is the volume of a magnetic flux tube, and $\delta P$ is the change in pressure. The model is based the interchange of two neighboring magnetic flux tubes, as shown in Fig. 2.1.5. If when moving from flux tube 1 to 2 (Fig. 2.1.5), there is a net decrease in plasma pressure (caused by a decrease in density, for example) an instability will occur if the volume of the flux tube increases. Equation 2.1.30 can be used to derive the following condition for instability:

$$\delta \int \frac{dl}{B} > 0, \tag{2.1.31}$$

where $dl$ is a differential path length, and $B$ is the strength of the magnetic field. Equation 2.1.31, in essence, defines the curvature that a magnetic field must have in order to be stable. A mirror field, as shown in Fig. 2.1.3, has the "wrong" curvature, i.e., the magnetic field lines curve toward the plasma. One method of having the correct curvature is to combine the solenoidal field with a multipole field. The resultant magnetic field configuration is such that magnetic field lines curve away from the plasma everywhere, and hence are resistant to interchange instability. In addition, the magnetic field strength increases in all directions as one moves away from the center of the plasma ("minimum-B"). All MCI ECRIS use this minimum-B configuration.

### 2.1.6 Plasma power and particle balance

It is useful to have a general understanding of what determines the particle density and electron temperature in a plasma. Estimates for these can be obtained using simple power and particle balances. The following discussion is based on material from Lieberman and Lichtenberg, second edition[36]. The model assumes a cylindrical plasma, a nearly uniform plasma density in the bulk, and Maxwellian electrons. The validity of some of these assumptions, as applied to the plasmas found in a typical ECRIS, is questionable. For example, it has been shown that the electron energy distribution function is non-Maxwellian[41]. In spite of this shortcoming, the model is still useful in understanding the basic parameters that control plasma density and electron temperature.

The electron temperature is estimated using a particle balance in which the creation of electron-ion pairs in the bulk plasma is balanced by their losses to the walls:

$$n_0 u_B A_{eff} = K_{iz} n_g n_0 \pi R^2 l. \tag{2.1.32}$$

In this equation $n_0$ is the plasma density, $u_B$ is the Bohm speed, $A_{eff}$ is an effective area for loss of particles, $K_{iz}$ is the ionization rate constant, $n_g$ is the neutral density, and $R$ and $l$ are the radius and length of the plasma. The left hand side of the above equation corresponds to electron-ion pair loss, and the right hand side corresponds to electron-ion pair creation. Equation 2.1.32 can be rearranged into the following form:

$$\frac{K_{iz}(T_e)}{u_B(T_e)} = \frac{1}{n_g d_{eff}}, \tag{2.1.33}$$

where

$$d_{eff} = \frac{\pi R^2 l}{A_{eff}}. \tag{2.1.34}$$

Equation 2.1.33 can be used to determine the electron temperature, if we know the behavior of the ionization rate constant as a function of temperature, given a value of $n_g d_{eff}$. At high energies, much greater than the ionization potential of an atom, the left hand side of Eq. 2.1.33 will be a monotonically decreasing function of electron temperature. In ECRIS plasmas it is possible for the electrons to reach temperatures of over 1 MeV[34] due to the heating mechanism, and the fact that collisionality decreases as electrons gain energy. We expect, then, that for the population of electrons we are studying (high energy) , the left hand side of Eq. 2.1.33 will indeed be a decreasing function of electron temperature. Hence, we can predict that either an increase in neutral gas density, $n_g$, or an increase in $d_{eff}$ will lead to a decrease in the electron temperature.

The central plasma density is estimated with a power balance, equating absorbed power to the power carried away by electron-ion pairs leaving the plasma:

$$P_{abs} = e n_0 u_B A_{eff} \varepsilon_{T,} \tag{2.1.35}$$

where $\varepsilon_T$ is the total energy carried away by each electron-ion pair lost from the plasma. Rear-

ranging Eq. 2.1.35 one obtains an equation for the plasma density:

$$n_0 = \frac{P_{abs}}{eu_B A_{eff} \varepsilon_T}, \tag{2.1.36}$$

showing that, in general, as the absorbed power increases the plasma density also increases, and that as the effective loss area, $A_{eff}$, increases the plasma density decreases. Unlike in the case of electron temperature, particle density does not explicitly depend on neutral gas density.

In a low pressure discharge, such that the ion mean free path is greater than the characteristic dimensions of the plasma, $A_{eff}$ is essentially independent of pressure. The Bohm speed, $u_B$, and the energy loss term, $\varepsilon_T$, both depend on pressure through their relationship to electron temperature: both increase as electron temperature increases. Using Eq. 2.1.33 one can show that, for a given value of $d_{eff}$, as gas pressure ($n_g$) is increased, electron temperature decreases. Hence, $u_B$ and $\varepsilon_T$ will decrease as gas pressure increases. Using Eq. 2.1.36, we see that at low neutral pressures and for a given absorbed power, an increase in neutral gas pressure will increase the plasma density.

The power absorbed by the plasma, $P_{abs}$, in Eq. 2.1.36 is not the power delivered to the plasma chamber. To estimate the absorbed power in an ECR heated plasma, one can use the theory proposed by Budden[8]. For a wave propagating into a decreasing magnetic field, the ratio of absorbed power to incoming power is given by:

$$\frac{P_{abs}}{P_{inc}} = 1 - e^{-\pi\eta}, \tag{2.1.37}$$

with

$$\eta = \frac{\omega_{pe}^2}{\omega c \, |\alpha|}. \tag{2.1.38}$$

The quantity $\alpha$ is proportional to the spatial derivative of the magnetic field near the resonance zone. $P_{inc}$ in Eq. 2.1.37 refers to the power delivered to the plasma chamber. For a given microwave frequency and spatial derivative, Eq. 2.1.37 shows that the ratio of absorbed power to incoming power will increase as the plasma density increases. For a given microwave frequency and plasma density, decreasing the spatial derivative in the resonance zone will lead to more efficient power absorption. This trend has been observed in many ECRIS experiments where the effect of the magnetic field confinguration was being studied[14, 34, 56].

### 2.1.7 Plasma diamagnetism

In a magnetized plasma, such as those found in ECRIS, charged particles orbit around the magnetic field lines in such a way that the magnetic field created by their motion opposes the externally applied magnetic field. If a plasma is uniform, i.e., no density or temperature gradients, then the currents created by neighboring charged particles will cancel, and no net current will exist. If, on the other hand, gradients are present in a plasma a net current can arise. This macroscopic current creates a magnetic field that acts to decrease any external magnetic field, and is thus called a “diamagnetic” current. A common method of measuring

the diamagnetic current is to exploit Faraday's law by using a loop of wire that is wrapped around the plasma.

As the plasma in an ECR ion source forms or decays, the changing current creates a time varying magnetic field that opposes the steady, external magnetic field. By Faraday's law, an electric field is created. The electric field is responsible for creating a voltage across the leads of the diamagnetic loop, which is what is ultimately measured.

The electromotive force (emf) in the diamagnetic loop can be written

$$\varepsilon_P = -N\frac{d\phi}{dt}, \tag{2.1.39}$$

where $N$ is the number of turns in the diamagnetic loop, and $\phi$ is the magnetic flux passing through the loop. We can rewrite Eq. 2.1.39 as

$$\varepsilon_P = -N\frac{d}{dt}\oint_S (\mathbf{B_0} + \mathbf{B_P}) \cdot \mathbf{dS}, \tag{2.1.40}$$

where $\mathbf{B_0}$ is the externally applied magnetic field, and $\mathbf{B_P}$ is the magnetic field due to the plasma. If we next integrate Eq. 2.1.40 with respect to time it becomes

$$\int^t \varepsilon_P dt = -N\oint_S \mathbf{B_P} \cdot \mathbf{dS}, \tag{2.1.41}$$

where we have made use of the fact that external field, $\mathbf{B_0}$, does not vary with time. Equation 2.1.41 relates the integrated diamagnetic signal to magnetic flux created by the diamagnetic current.

The magnetic field due to the plasma, $\mathbf{B_P}$, can be related to the plasma energy density[9]:

$$\int^t \varepsilon_P dt = \frac{\pi\mu_0 r_0^2 N}{B_0} n_0 kT, \tag{2.1.42}$$

where $r_0$ is the plasma radius, and $n_0kT$ is the plasma energy density due to all charged particles in the plasma. To arrive at this equation it is assumed that the density profile is given by $n = n_0 exp\left[-(r/r_0)^2\right]$, the velocity distribution is isotropic so that the pressure tensor reduces to a scalar, and that the plasma can be represented by the ideal MHD equilibrium equation $\nabla p = \mathbf{j} \times \mathbf{B}$ (see [9] Chapter 6, problem 6-5 for details of the derivation of Eq. 2.1.42).

## 2.2 Single particle ECR heating model

The physics of energy absorption in an ECR plasma is complicated and not fully understood. However, many useful insights into the energy transfer mechanism in an ECR plasma can be obtained by examining a simple, single particle heating model. In this section we will use such a model to predict how different physical parameters affect the energy gained by an electron as it moves in a magnetic mirror field.

The magnetic field configuration is a simple magnetic mirror described by the following equations[27]:

$$B_x(x,y,z) = -xbB_0\left(\frac{\pi}{L}\right)\sin\left(\frac{2\pi z}{L}\right) \quad (2.2.1)$$

$$B_y(x,y,z) = -ybB_0\left(\frac{\pi}{L}\right)\sin\left(\frac{2\pi z}{L}\right) \quad (2.2.2)$$

$$B_z(x,y,z) = B_0\left[1-\left[1+\left(\frac{\pi r}{L}\right)^2\right]b\cos\left(\frac{2\pi z}{L}\right)\right], \quad (2.2.3)$$

with

$$b = \left(\frac{R_m-1}{R_m+1}\right)$$
$$r^2 = x^2+y^2.$$

The mirror ratio is $R_m$, $B_0$ is a magnetic field magnitude, and L is the distance between mirror points.

The electric field of the injected microwaves is modeled with the following equations:

$$E_x(z,t) = E\left[\cos(\omega t - kz + \delta_1) + \rho\cos(\omega t + kz + \delta_2)\right] \quad (2.2.4)$$

$$E_y(z,t) = E\left[\sin(\omega t - kz + \delta_1) + \rho\sin(\omega t + kz + \delta_2)\right] \quad (2.2.5)$$

$$E_z(z,t) = 0 \quad (2.2.6)$$

Here, E is the magnitude of the electric field, $\omega$ is the driving frequency, $\rho$ is a constant, and $\delta$ is a phase difference. RHCP travelling or standing waves can be modelled with these equations by choosing an appropriate value for $\rho$ and $\delta$. For example, one possible way of creating standing waves is by setting $\rho = 1$, $\delta_1 = 0$, and $\delta_2 = 90$.

The relativistic equations of motions are given by:

$$\frac{d\mathbf{r}}{dt} = \mathbf{v} \quad (2.2.7)$$

$$\frac{d\mathbf{v}}{dt} = \frac{e}{m\gamma}\left[\mathbf{E} + \mathbf{v}\times\mathbf{B} - \frac{\mathbf{v}}{c^2}(\mathbf{E}\cdot\mathbf{v})\right] \quad (2.2.8)$$

$$\gamma = \left(1-\frac{v^2}{c^2}\right)^{-1/2}. \quad (2.2.9)$$

The equations of motion, along with Eqn. 2.2.1-2.2.3 and Eqn. 2.2.4-2.2.6 can solved simultaneously to obtain the position and velocity of a charged particle as a function time. We have chosen to use Mathematica version 6 to perform the required calculations.

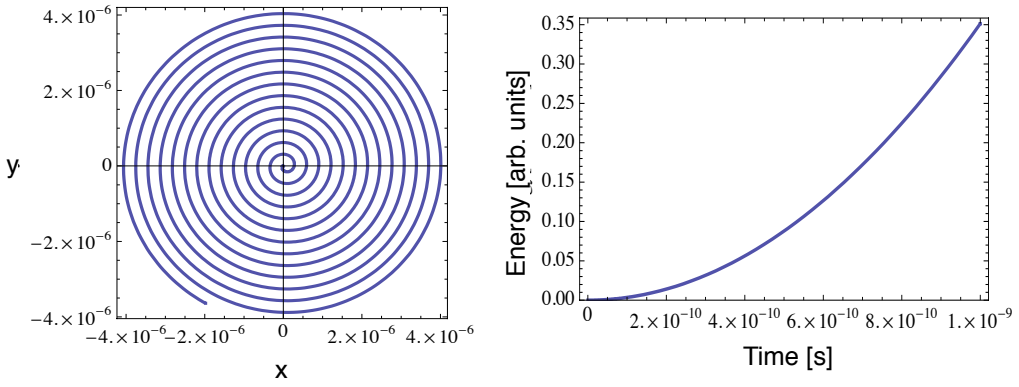


Figure 2.2.1: Interaction of a RHCP wave with an electron in a constant magnetic field. Left: position of electron as function of time. Right: electron energy as function of time.

### 2.2.1 Model results

One of the simplest cases we can examine is the interaction of a RHCP wave with an electron in a spatially and temporally invariant magnetic field. The frequency of the RHCP is chosen to match the cyclotron frequency. Figure 2.2.1 shows the results of this interaction. The electron, which starts at the origin with a speed equal to zero, is seen to continually gain energy as the RHCP wave transfers energy to it. As the electron is gaining energy, it spirals away from the origin at larger and larger radii. Why this happens becomes immediately obvious if one recalls the equation for the Larmor radius of a charged particle: $r_{L,r>0} = {}^{mv_\perp}/_{eB}$.

We can also examine the interaction between a LHCP wave and an electron. The magnetic field is again constant in both space and time, and the frequency of the LHCP wave is set equal to the cyclotron frequency. From Fig. 2.2.2 we can see that instead of a continuous energy gain, the electron energy instead oscillates in time, and that, on average, its energy does not change. From the plot on the left side of Fig. 2.2.2 we see that the phase angle (defined as the angle between the velocity vector of the electron and the electric field vector) also oscillates in time around an average value of 90 degrees. When comparing the plot of phase angle to the plot of energy, we see that when the phase angle is greater than 90 degrees the electron gains energy, and whenever the phase angle is less than 90 degrees the electron loses energy. This can be understood by deriving a simple equation for the power delivered to a non-relativistic electron:

$$\begin{aligned} P &= \mathbf{F}\cdot\mathbf{v} \\ &= -e(\mathbf{E}+\mathbf{v}\times\mathbf{B})\cdot\mathbf{v} \\ &= -eEv\cos\phi. \end{aligned}$$

Hence, whenever the phase angle, $\phi$, is less than 90 degrees, then the cos of that angle is positive, and the power is negative. The opposite is true when $\phi$ is larger than 90 degrees.

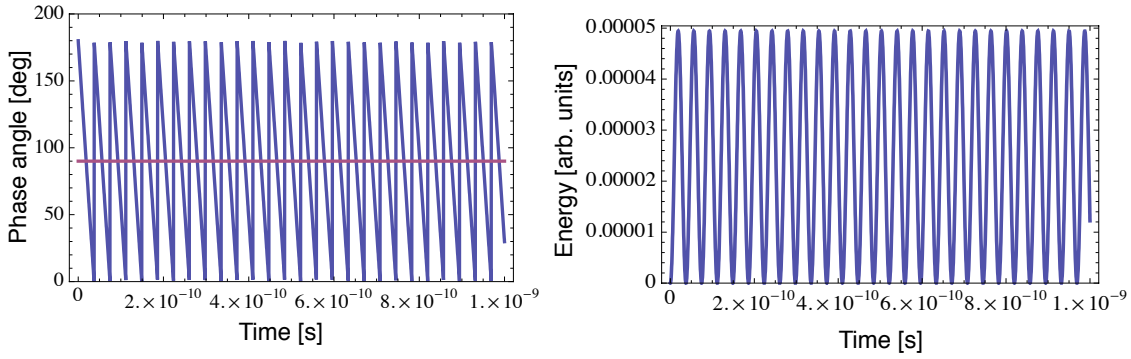


Figure 2.2.2: Interaction of a LHCP wave with an electron in a constant magnetic field. Left: phase angle as function of time. Right: electron energy as function of time.

Finally, we study the more complicated situation of an electron moving in a mirror field and interacting with a travelling RHCP wave. The magnetic field is modeled by Eqn. 2.2.1 to 2.2.3, with values for $R_m$, $L$, and $B_0$ shown in in Fig. 2.2.3. The electric field is given by the following equations (obtained by setting $\rho = 0$ and all phase differences to zero in Eqn. 2.2.4 and 2.2.5):

$$\begin{aligned} E_x(z,t) &= E\left[\cos\left(\omega t - kz\right)\right] \\ E_y(z,t) &= E\left[\sin\left(\omega t - kz\right)\right] \\ E_z(z,t) &= 0, \end{aligned}$$

with a driving frequency,$\omega$, of 28 GHz. The magnitude of the electric field, $E$, is arbitrarily set to 50 kV/m. We note, that the cyclotron damping of the electric field at the resonance point is not modeled.

The electron is started at a position of $(x_0, y_0, z_0) = (0, 0 + r_L, 0)$, with an initial velocity (in units of *m/s*) of $(u_0, v_0, w_0) = \left(-2.0 \times 10^6, 0.0, 6.0 \times 10^6\right)$. The model is run for a time of $3.5 \times 10^{-8}$ s, enough time for the electron to make a single pass through one resonance zone. The results are shown in Fig. 2.2.4. Far from the resonance zone we see that the electron total kinetic energy oscillates in time, but does not gain or lose energy, on average. As the particle approaches the resonance zone, the total kinetic energy oscillations grow larger, the parallel kinetic energy slowly decreases, and the average perpendicular kinetic energy slowly increases. The slow decrease in parallel kinetic energy is caused by the force given in Eq. 2.1.26. When the electron is finally in resonance, there is a large increase in total kinetic energy, from an average energy slightly above 100 eV, to approximately 420 eV. Once through the resonance zone, the electron parallel kinetic energy decreases at a faster rate. Again, we can explain this by studying Eq. 2.1.26, which shows us that the axial force felt by the electron is proportional to its perpendicular kinetic energy.

If we allow the simulation to run for a longer period of time we can observe the behavior

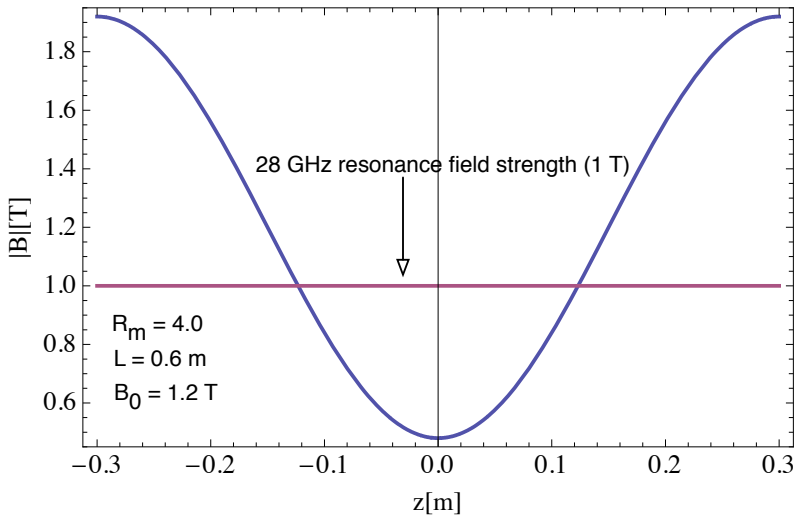


Figure 2.2.3: Magnetic mirror field used in model.

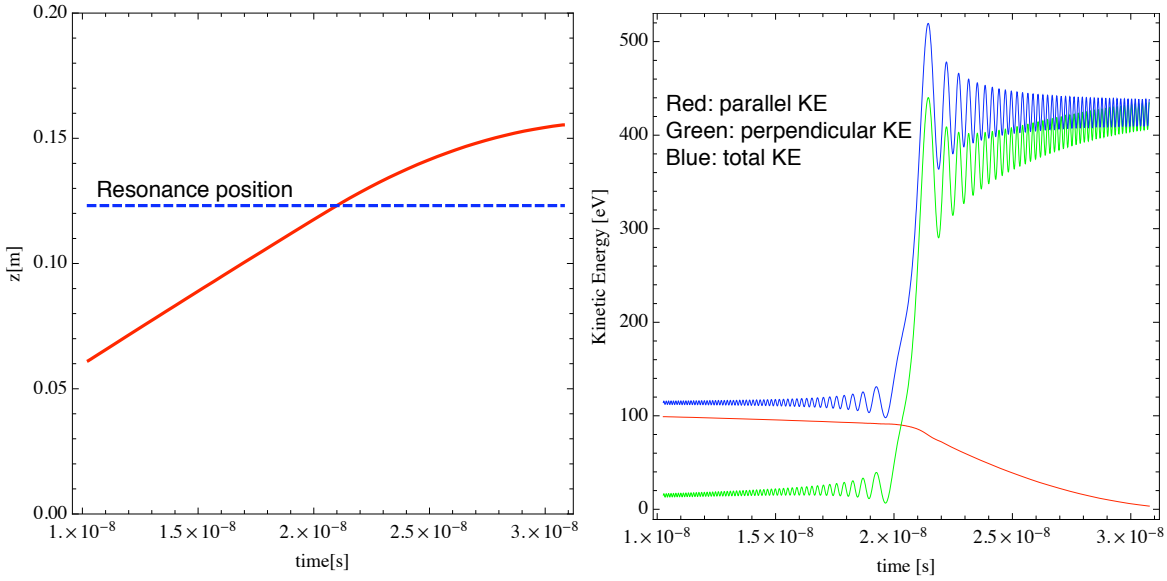


Figure 2.2.4: Electron making a single pass through resonance. Left: axial position of electron. Right: components of the electron kinetic energy.

| $B_0 =$ | 0.8 | 1.2 | 1.6 | 2.0 |
|---|---|---|---|---|
| Gradient [T/m] | 3.92 | 5.89 | 7.85 | 9.81 |
| $\triangle$(Mean total kinetic energy) [eV] | 378 | 212 | 121 | 67 |
| f [GHz] | 14 | 21 | 28 | 35 |

Table 2.1: Summary of changes to magnetic field for gradient study.

of an electron as it makes multiple passes through the two resonance zones. The electron is given identical initial conditions to the case above. The axial position and kinetic energy of the electron as a function of time are shown in Fig. 2.2.5. The initial velocity and magnetic field configuration are such that without ECR heating, the electron would not mirror. With ECR heating, though, we can see that the electron passes through the resonance zone, mirrors, and then passes again through the resonance zone. We can explain this behavior by once again referring to Eq. 2.1.26. When passing through the resonance zone for the first time, the electron has its perpendicular velocity increased, as shown in the plot on the right hand side of Fig. 2.2.5. The axial force, $F_z$, which depends on the square of the perpendicular velocity, is increased to the point that it stops the electron and accelerates it back, towards the midpoint of the mirror. The result of this is that the electron makes two resonance zone crossings in close succession.

Inspection of Fig. 2.2.5 indicates that the electron can actually lose kinetic energy when passing through a resonance zone. As discussed earlier, whether an electron gains or loses energy depends on the phase angle between its velocity vector and the local electric field vector. Figure 2.2.6 shows how the phase angle of an electron varies in a small time window. We can see three distinct features in this plot. First, there is an oscillation of the phase angle about 90 degrees when the electron is far from a resonance point. Any heating period is immediately followed by a cooling period that essentially cancels out any energy gain. Second, there is a longer period of cooling associated with the electron passing through a resonance point. Third, there is a longer period of heating, that is also associated with a resonance crossing. According to this model, whether an electron is heated or cooled depends on its state immediately before entering a resonance zone. If the electron phase angle is greater than 90 degrees prior to crossing a resonance, it will suffer an extended period of cooling. Similarly, if the phase angle is less than 90 degrees ahead of entering a resonance, the electron will undergo an extended heating period.

We also examined the effect of magnetic field gradient on single particle energy gain when passing through resonance. Simple theoretical models predict that the energy gained by a particle is inversely proportional to the magnetic field gradient[28] (also see Eq. 2.1.16). To perform this study the mirror ratio, $R_m$, and and length between mirror points, $L$, were held fixed. To change the gradient, the strength of the magnetic field, $B_0$, was varied (increasing $B_0$ increases the slope). In order to fix the axial position (z-coordinate) of the resonance point, the heating frequency was scaled with $B_0$. Table 2.1 summarizes the changes. The model was run long enough to allow the particle to pass once through a single resonance zone. The metric of interest is the change in mean total kinetic energy of the electron as it passes through resonance.

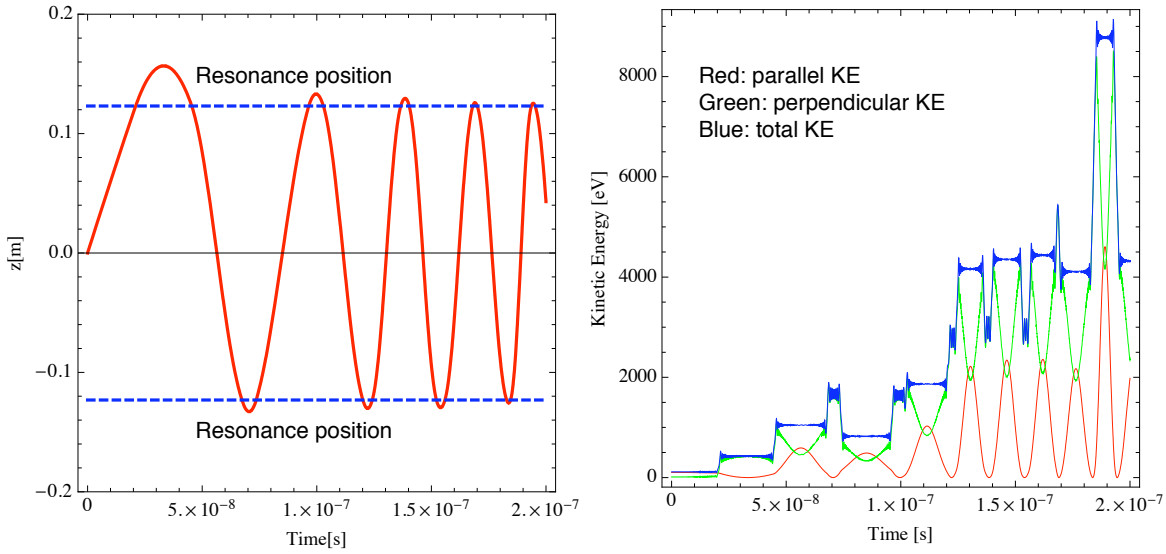


Figure 2.2.5: Electron making multiple passes through resonance. Left: axial position of electron. Right: components of the electron kinetic energy.

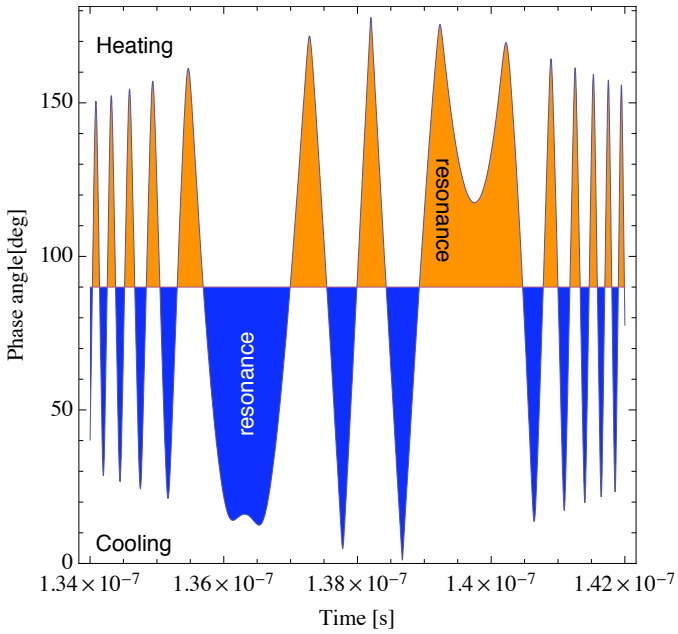


Figure 2.2.6: Phase angle of electron as a function of time.

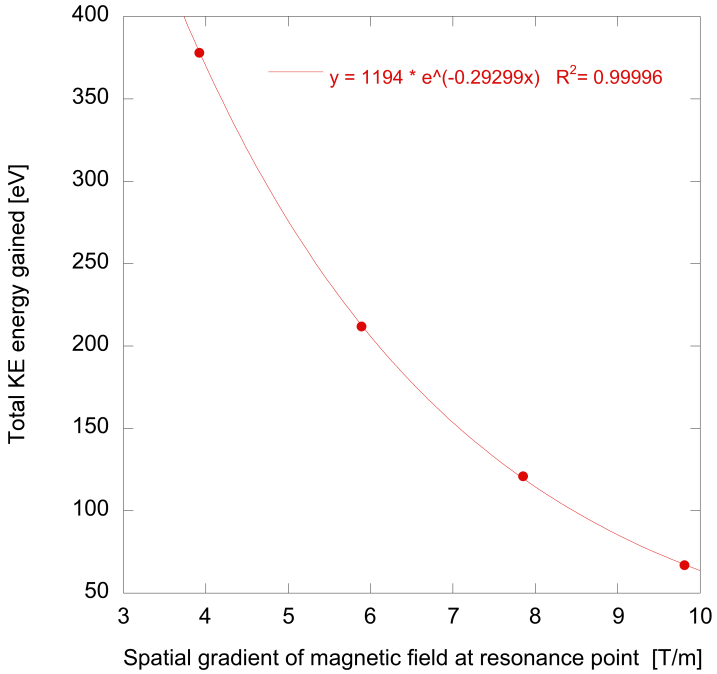


Figure 2.2.7: Change in total kinetic energy per pass of electron as a function of magnetic field gradient in resonance zone.

Figure 2.2.7 shows a plot of the change in mean total kinetic energy per pass as a function of the gradient of the magnetic field in the resonance zone. As predicted by theoretical models, our computational model shows that decreasing the gradient of the magnetic field in the resonance zone has the clear effect of increasing the energy gain.

## 2.3 X-ray cross sections

Several mechanisms are responsible for the emission of x-rays in an ECR ion source plasma. X-rays can be created in electron-ion or electron-electron collisions in the plasma, or when unconfined electrons strike the ion source vacuum structure. These x-rays result in a continuous spectra. Also, characteristic x-rays are emitted as excited ions transition back to the ground state. X-rays created in this manner cause discrete peaks to appear in recorded spectra. If the ultimate goal is determination of the electron energy distribution function, then x-rays emitted from electron-ion collisions become the most important. All x-rays, though, are important when considering the total x-ray power emitted by the plasma.

In this section we discuss the cross sections for creation of photons during a Coulomb collision between a light (electron) charged particle and a massive (atom) particle. The effects of the electron cloud surrounding the nucleus are ignored. In the low frequency limit (the energy of the created photon is much, much less than the energy of the incoming electron), the

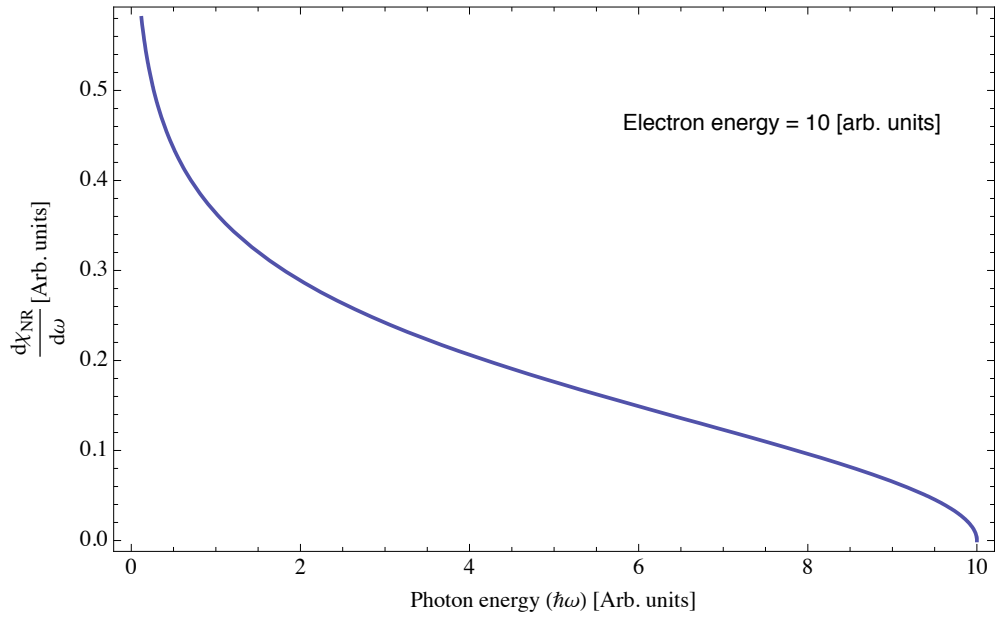


Figure 2.3.1: Nonrelativistic bremsstrahlung cross section.

radiation cross section integrated over momentum transfers can be written (cgs units)[26]:

$$\frac{d\chi}{d\omega} \simeq \frac{16}{3}\frac{Z^2e^2}{c}\left(\frac{z^2e^2}{Mc^2}\right)^2\frac{1}{\beta^2}\ln\left(\frac{Q_{max}}{Q_{min}}\right). \tag{2.3.1}$$

Here, $Ze$ is the charge of the massive, target particle, $ze$ is the charge of the projectile particle (simple $e$, in case of an electron), $M$ is the mass of the projectile particle, $\beta$ is the speed of the projectile particle (normalized by the speed of light), and $Q_{max}$ and $Q_{min}$ are maximum and minimum momentum transfers. In the nonrelativistic case Eq. 2.3.1 can be written:

$$\frac{d\chi_{NR}}{d\omega} \simeq \frac{16}{3}\frac{Z^2e^2}{c}\left(\frac{z^2e^2}{Mc^2}\right)^2\frac{1}{\beta^2}\ln\left[\frac{\lambda'\left(\sqrt{E}+\sqrt{E-\hbar\omega}\right)^2}{\hbar\omega}\right]. \tag{2.3.2}$$

In this equation E is the total energy of the incident particle, $\hbar\omega$ is the energy of the photon, and $\lambda'$ is a number close to unity. The behavior of the cross section given in Eq. 2.3.2 is shown in Fig. 2.3.1 for an electron with energy 10 (in arbitrary units). It can be seen that photons of energy up to and including the energy of the incident electron can be produced (although the probability of producing a photon with an energy equal to the electron energy is vanishingly small). What is important to realize is that a photon with energy $\hbar\omega$ can be produced by an electron with energy $E \geq \hbar\omega$.

For relativistic particles Eq. 2.3.1 can be written:

$$\frac{d\chi_R}{d\omega} \simeq \frac{16}{3}\frac{Z^2e^2}{c}\left(\frac{z^2e^2}{Mc^2}\right)^2\ln\left(\frac{\lambda''EE'}{Mc^2\hbar\omega}\right), \tag{2.3.3}$$

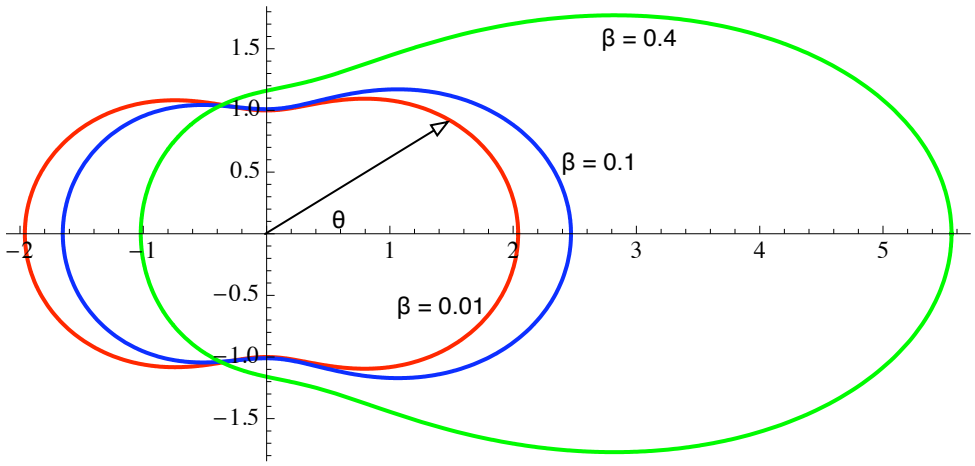


Figure 2.3.2: Polar plot of angular dependence of photon intensity in a collision between an electron and ion.

where $E'$ is the total energy of the incident particle after the collision, and $\lambda''$ is again a number of order one. Both the nonrelativistic and relativistic cross sections depend on the properties of the particles taking part in the collisions through the factors $Z$, $z$, and $M$. We see then, that the radiation cross sections will be much higher for collisions between light particles ($1/M$ dependence), and materials with high atomic numbers ($Z^2$ dependence).

If the change in the particle's velocity is small, and it occurs in a direction perpendicular to the incident direction, the angular dependence of radiation intensity is given by (again, in the low frequency limit)[26]:

$$\lim_{\omega\to 0}\frac{d^2I}{d\omega d\Omega}=\frac{z^2e^2}{8\pi^2c}|\Delta\beta|^2\left[\frac{(\beta-\cos\theta)^2}{(1-\beta\cos\theta)^4}+\frac{1}{(1-\beta\cos\theta)^2}\right], \tag{2.3.4}$$

where $\theta$ is the angle between the direction of observation and the velocity vector of the incident particle. Figure 2.3.2 shows a plot of Eq. 2.3.1 for three different values of $\beta$. It is seen that the distribution becomes more and more peaked in the forward direction, i.e., along the direction of motion, as the speed of the particle is increased. At $\beta = 0.4$, or approximately 27 keV for an electron, we see that, already, it is most likely that a photon will be emitted in the forward direction during a collision.

## 2.4 Summary

We have shown that collision frequencies decrease as the energy of the charged particle increases. This can allow for a group of electrons to become heated to temperature as high as 1 MeV[34] if they make multiple passes through resonance zones. X-rays with energies greater than 100 keV were routinely detected. Based on the x-ray data we can infer that electrons with energies greater than 100 keV must exist in some abundance in the ECRIS plasmas we

examined.

A simple power balance showed that the density of the plasma is primarily controlled by the absorbed microwave power. This simple model is largely confirmed by measurements of x-ray power and plasma energy density, which increase as microwave power is increased. Both x-ray power and plasma energy density were seen to saturate on the 6.4 GHz ECR at higher microwave powers. This saturation is likely due to another phenomenon that will be discussed in Chapter 3.

The electron temperature (at high energies) was predicted to be inversely proportional to neutral pressure and effective loss area. Measurements of x-ray power and plasma energy density agree with this prediction. In Chapter 3 we will show that increasing the neutral pressure causes the average electron energy to decrease.

A simple, single particle computational model predicted that the electrons are more efficiently heated as the gradient of the magnetic field in the resonance zone is decreased. This is also confirmed by both x-ray and diamagnetic loop measurements. We will show in the following chapters that as magnetic field strength is increased x-ray power and plasma energy density both increase.

In order to better understand the x-ray spectra that are shown in the following chapters it is important to keep in mind several points. Photons are concentrated in an increasingly forward direction as the velocity of the incident electron increases. If we measure a 100 keV photon, it is highly likely that the velocity of the electron just prior to the collision was directed toward the detector. Photons with an energy nearly equal to that of the incoming electron can be created, but it is far more likely that a photon with a lower energy will be created. Hence, photons recorded with an energy of 100 keV most likely came from electrons of energy greater than 100 keV. The bremsstrahlung cross section is much higher in materials with high atomic numbers (Eqn. 2.3.2 and 2.3.3). An electron moving through a solid object (plasma chamber wall, for example) will produce photons a larger rate than one moving through an ECRIS plasma.

# Chapter 3

# Studies of electron heating on a 6.4 GHz ECR ion source

## 3.1 Introduction

This chapter presents an examination of electron heating in the LBNL 6.4 GHz ECR. Two diagnostic methods were used in this study. The first, measurement of plasma bremsstrahlung, is a common high temperature plasma diagnostic. Plasma bremsstrahlung spectra can be used to estimate x-ray power, and to learn about the distribution of electron energies in the plasma. In this particular study we focused our attention on "low" energy x-rays in the range 2 keV-70 keV.

The second is the "diamagnetic loop." This device is simply a loop, usually consisting of multiple turns, of wire placed around the plasma in such a manner that the external magnetic field lines are perpendicular to plane created by the loop. The signal measured by the loop when the microwave power is turned on is proportional to the rate of formation of the plasma, and can be related to the plasma energy density. Similarly, the signal measured by the loop when the microwave power is turned off is proportional to the decay rate of the plasma. Barue *et al.* [4]have previously successfully taken both bremsstrahlung measurements and diamagnetic current measurements on an 18 GHz ECRIS. Their results showed that the integrated diamagnetic signal, and thus plasma energy density, increased with the microwave power and did not saturate at higher microwave powers.

This chapter is divided into three major sections. We start with a description of the experimental setup and equipment in Section 3.2. In Section 3.3, the effects of microwave power, neutral pressure, and magnetic field configuration on both the plasma bremsstrahlung and diamagnetic signal are shown. In Section 3.4, explanations for the observed trends are proposed.

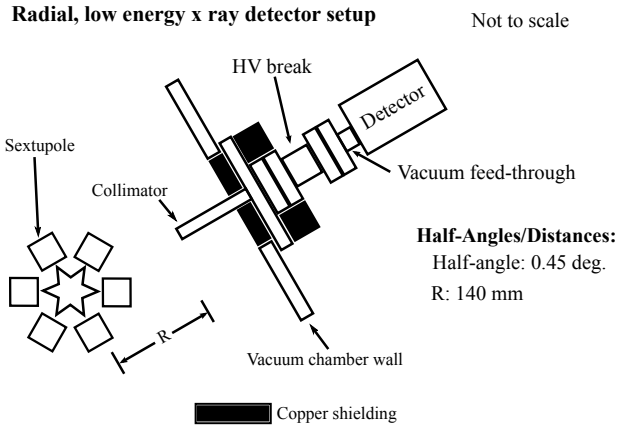


Figure 3.2.1: Low energy x-ray measurement setup.

## 3.2 Experimental Setup

### 3.2.1 Low energy x-ray measurement

X-rays are detected and processed with an Amptek XR-100T-CdTe detector and PX4 digital pulse processor[2]. The XR-100T-CdTe is a semiconductor, planar diode type x-ray detector. The basic operating principle is as follows. As photons interact with the CdTe crystal, they create an equal number of electron-hole pairs along the path they traverse. A bias voltage is applied across the CdTe semiconductor, and so the electrons and holes drift towards opposite electrodes due to the electric field. The amount of charge that is collected is proportional to the energy of the photon. The XR-100T-CdTe has a detection efficiency of 20% or greater over an energy range of approximately 2-200 keV. More details on the operating principles of CdTe detectors can be found in Appendix B.

The PX4 provides power and high voltage to the XR-100T-CdTe. It is also a digital pulse processor and multichannel analyzer (MCA). The PX4 allows the user to change parameters such as the high voltage bias and shaping times, as well as allowing the user the option of using pile-up rejection or rise time discrimination.

The experimental setup used to measure the radial, low energy x-rays is shown in Fig. 3.2.1. The detector, collimator, and shielding are placed in a radial access port of the ECR. The entire assembly is located within the high voltage cage of the ECR. The collimation and shielding are designed to ensure that only x-rays created in the plasma are detectable by the XR-100T-CdTe.

The copper collimator is 25.4 cm in length and has a 2 mm by 2 mm groove machined into it. The tip of the collimator is located approximately 14.0 cm from the centerline of the ion source. The geometric half-angle defined by this configuration is 0.45 degrees. The volume of plasma that is visible to the XR-100T-CdTe is roughly 600 cubic millimeters.

Shielding is provided by large copper blocks. The extra shielding is necessary because we want both the geometric solid angle (defined by the collimator) and the "x-ray solid angle" to be equal. We define the "x-ray solid angle" as the solid angle in which an x-ray must be created

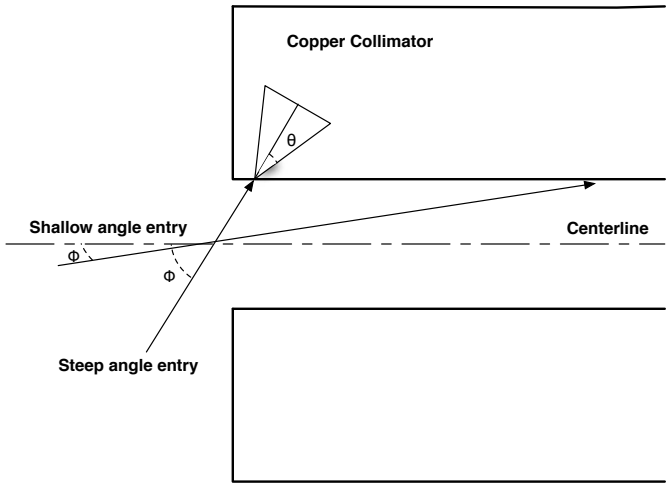


Figure 3.2.2: Diagram of collimator tip showing various angles used in discussion.

to have a chance of reaching the detector. Based on previous studies performed on the ECR we estimate the maximum x-ray energy is approximately 400 keV[40]. Thus, enough shielding is added to block approximately 93% of x-rays with energies below 400 keV, unless they are created within the geometric solid angle of the collimator. The detection efficiency of the XR-100T-CdTe falls off rapidly at energies above 50 keV, and 400 keV photons are detected with an efficiency of approximately only 7%.

There is some probability that electrons will enter the collimator opening, undergo one or more interaction events, and then be detected. Because a photon loses energy during each interaction event, it will reach the detector with less energy than it was created with, thus artificially skewing the recorded spectra towards lower energies.

Below approximately 100 keV photons are most likely to undergo photoelectric absorption ( $\approx 1.7$ times more likely at 100 keV, and $\approx 140$ times more likely at 10 keV). The emitted photoelectron has an energy equal to: $E_{e-} = h\nu - E_b$ , where $h\nu$ is the energy of the photon, and $E_b$ is the binding energy of the photoelectron. The ejected photoelectron will, most likely, lose its energy interacting with the copper atoms. The characteristic x-ray emitted in this process will most probably undergo photoelectric absorption. Given the length of the collimator, this process will repeat itself until the initial energy of the photon is lost, well before it reaches the detector. Therefore, these photons should not alter the spectrum in a significant manner.

Photons with energies above approximately 150 keV interact with the copper atoms primarily by Compton scattering. The likelihood that a Compton scattered photon can reach the detector after one, or possibly more interactions, will depend on its initial energy and the angle with which it first entered the collimator. Photons that enter the collimator with a steep angle ($\phi$ in Fig. 3.2.2), with respect to the collimator's longitudinal axis, will most likely not be detected. Using the Klein-Nishina formula[30] we can estimate at an energy of 150 keV, approximately 64% of photons are scattered in a mostly forward direction, into a cone with a half-angle ($\theta$ in Fig. 3.2.2) of 90 degrees. Thus, the majority of these photons will lose all of their initial energy in multiple Compton scattering and photoelectric absorption events before

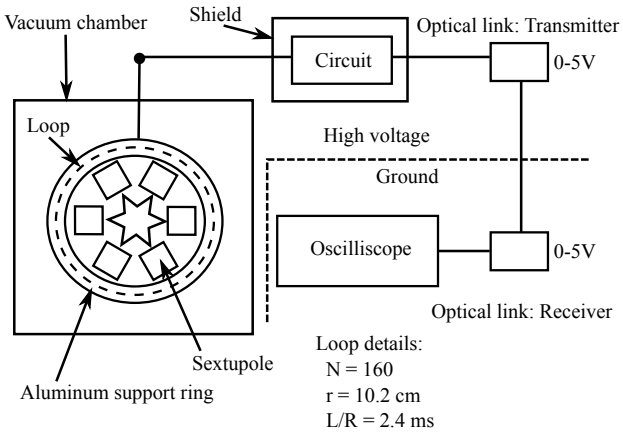


Figure 3.2.3: Experimental setup of diamagnetic loop used for plasma energy density measurements.

reaching the detector.

Because the scattering angle of photons with energies greater than 150 keV is mostly in a forward direction, the collimator is more likely to scatter the photons into the detector as the photon's entry angle becomes shallower. These photons have the largest probability of shifting the recorded x-ray spectra to lower energies. We note, though, that to have an appreciable change in energy, and thus cause a noticeable change in the x-ray spectra, a photon must be scattered by a relatively large angle. For example, a photon with an initial energy of 150 keV will lose 10% of this energy if it is scattered by 45 degrees. A large scattering angle increases the chance that a photon will reenter the copper and decreases the chances of reaching the detector. X-ray spectra are not corrected for photons that are scattered off of the interior of the copper collimator.

### 3.2.2 Diamagnetic loop

Plasma diamagnetism has been described from a theoretical standpoint in an earlier chapter. The experimental setup used to measure the diamagnetic signal is shown in Fig. 3.2.3. The diamagnetic loop is located within the vacuum chamber of the ECR. It is wound upon an aluminum support ring, which is, in turn, placed onto the sextupole structure. The leads of the diamagnetic loop are brought out of the vacuum chamber with a feed through. The loop and aluminum support ring are in electrical contact with source, and so float up to high voltage.

The raw signal from the loop is processed by a circuit, described in greater detail in the following section. Both the external portion of the feed through and the circuit are contained in an aluminum enclosure to prevent pick up of external noise.

To bring the diamagnetic loop signal outside of the high voltage cage that surrounds the ECR, a fiber optic cable is used. The processed signal from the circuit is first sent to an optical transmitter through an SMA cable, and then to the optical receiver through the fiber optic cable. Finally, the signal is sent to an oscilloscope where it is saved to a Compact Flash card. To reduce noise in the signal the averaging feature of the oscilloscope is used. For each data

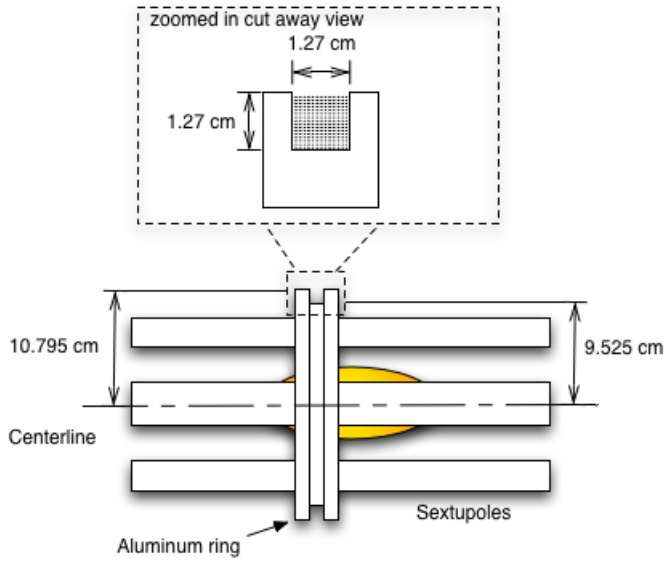


Figure 3.2.4: Approximate position of aluminum support ring. The yellow ellipse represents the approximate postion of the plasma.

set, the signal is averaged over 128 microwave power on/off cycles. The data is processed on a PC using a simple Mathematica notebook. We can estimate the plasma energy density using Eq. 2.1.42.

Figure 3.2.4 shows the approximate position of the aluminum support structure upon which the diamagnetic loop is wound. The loop itself is made of magnet wire and is circular with an approximately square cross section (1.27 cm by 1.27 cm). It has a mean radius of approximately 10.2 cm and has 160 turns. The resistance of the loop, as measured with a multimeter, is approximately 4 ohms.

To estimate the inductance of the loop the following formula is used[21]:

$$L = 0.001 a N^2 P_0^{'} \tag{3.2.1}$$

where $a$ is the mean radius of the loop in centimeters, $N$ is the number of turns, and the inductance, L, is given in microhenries. The parameter $P_0^{'}$ is given by:

$$P_0^{'} = 4\pi \left[ \frac{1}{2} \left( 1 + \frac{1}{6} \left( \frac{c}{2a} \right)^2 \right) ln \left( \frac{8}{(c/2a)^2} \right) - 0.84834 + 0.2041 \left( \frac{c}{2a} \right)^2 \right], \tag{3.2.2}$$

where $c$ is the depth of the loop winding.

If we plug in the dimensions of the loop into Eq. (3.2.1) and Eq. (3.2.2), then the inductance is approximately 9.7 mH. The time constant of the loop ($\tau = L/R$) is thus approximately 2.4 ms.

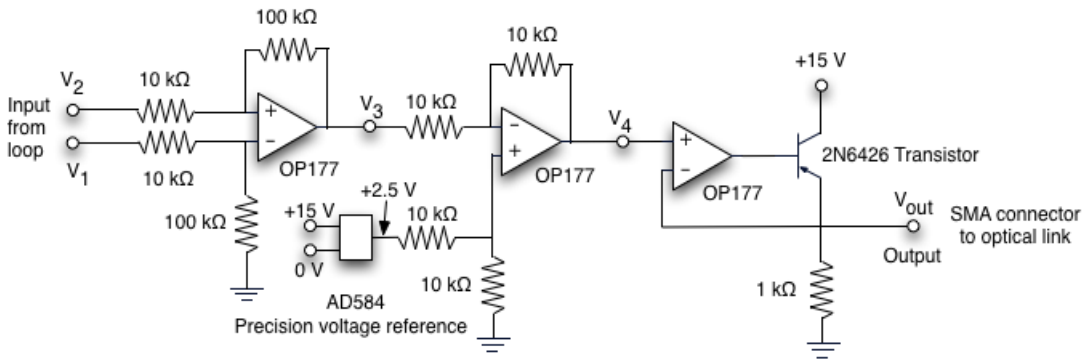


Figure 3.2.5: Diagram of circuit used to process diamagnetic loop signal.

We expect, then, the diamagnetic loop will be able to follow changes in plasma energy density that occur on timescales greater than approximately 10 ms.

### 3.2.3 Loop circuit

Figure 3.2.5 shows a diagram of the circuit used to process the diamagnetic loop signal. The circuit consists of three major sections: a differential amplifier, a level shifter, and, finally, a driver section. The circuit does not have an analog integrator as we have chosen to perform the integration on a PC.

The differential amplifier in the first section serves two purposes. The first is to amplify the signal from the diamagnetic loop. As shown in Fig. 3.2.5, the amplification is set to a factor of 10. The second purpose of the differential amplifier is common-mode rejection. If a voltage, due to some external source of noise, for example, is present in both inputs to the circuit, it will be subtracted out, leaving only the true diamagnetic loop signal. The output voltage of the differential amplifier is giving by:

$$V_3 = 10\,(V_2 - V_1)\,. \tag{3.2.3}$$

The purpose of the level shifter, the second section of the loop circuit, is to add an offset voltage of 2.5 V to the diamagnetic loop signal. The offset voltage is provided by an Analog Devices AD584 precision voltage reference. The output voltage, $V_4$, is the superposition of both a non-inverting and inverting amplifier input, and is given by:

$$V_4 = -10\,(V_2 - V_1) + 2.5V. \tag{3.2.4}$$

An offset of 2.5 V is required because the optical link transmitter and receiver used both require a voltage between 0-5 V. The loop signal, though, is both positive and negative, depending on whether the plasma is forming or decaying.

The final stage of the circuit is required to drive the analog optical link transmitter. The output voltage,$V_{out}$, of this stage is identical to $V_4$. The final voltage signal is sent to the optical

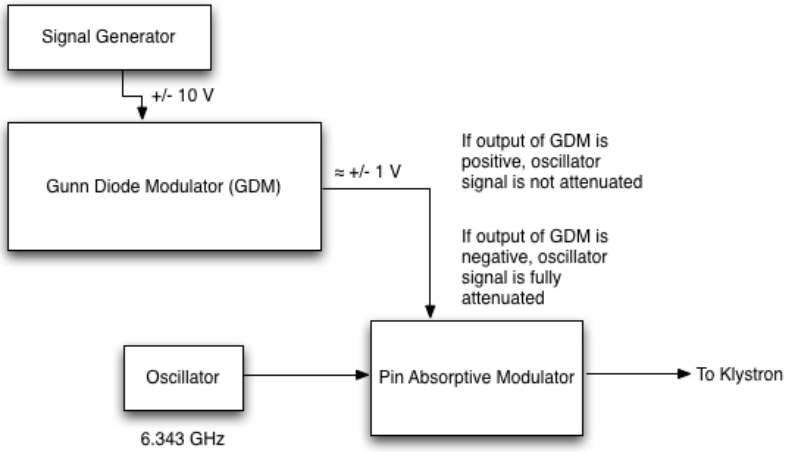


Figure 3.2.6: Diagram of Klystron pulsing circuit.

link transmitter through an SMA cable.

### 3.2.4 RF pulsing circuit

In order to measure a diamagnetic signal, which relies on changes in plasma density, the ECR must be operated in pulsed mode. There are several ways to pulse a Klystron, Fig. 3.2.6 shows a schematic of the method used in this study.

A signal generator is used to create the desired microwave pulse pattern. The signal is then sent to the Gunn Diode Modulator (GDM). The GDM is needed to provide the correct voltage and current values to drive the Pin Absorptive Modulator (PAM). When the output signal from the GDM is greater than zero, the PAM does not attenuate the oscillator signal. If the output signal from the GDM is negative the PAM fully attenuates the oscillator signal, and the power output is zero. Delays introduced with this method are on the order of microseconds. Plasma formation and decay timescales, though, are on the order milliseconds, and so the delays are ignored.

The formation and decay of the plasma will also induce currents in the aluminum support structure. However, if the conductivities of the loop and aluminum ring are approximately constant over the range of frequencies of interest, then the ratio of loop current to structure current will also be approximately constant, and a relative comparison of loop signals is valid. This eliminates the need to correct for the presence of the aluminum ring. As the conductivity of metals is approximately constant at frequencies below $10^{11}$ $s^{-1}$[26], and typical plasma formation and decay times are tens of milliseconds, the effect of the aluminum support structure on the recorded signal is neglected. A method to correct for the aluminum ring is described in Appendix A.

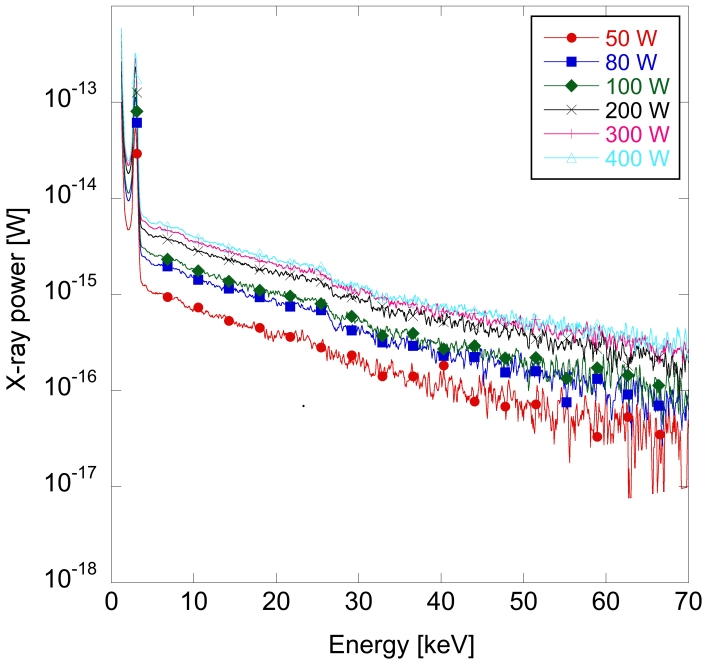


Figure 3.3.1: Example of x-ray spectra from an Argon plasma at different microwave powers.

## 3.3 Results

### 3.3.1 Low energy x-ray parametric studies

In Fig. 3.3.1 typical x-ray spectra, taken at different microwave powers with Argon as the working gas, are shown. The large peak located at approximately 3 keV is due to K-shell emission from excited Argon ions. The small step located at approximately 26 keV is caused by characteristic x-rays that escape from the CdTe crystal volume without being detected. The x-ray energy range of interest for this study was approximately 2 keV to 70 keV.

The spectral temperature, is defined as the inverse slope of a line fitted to the energy calibrated x-ray spectra data (for example, those shown in Fig. 3.3.1) over some energy range:

$$\frac{1}{kT_{spect}} = \frac{d\left(\ln J\right)}{d\left(h\nu\right)}, \tag{3.3.1}$$

where $J = h\nu \times N(h\nu)$. Calculated spectral temperatures are shown in Fig. 3.3.2. ECR ion source plasmas are known to be non-Maxwellian or bi-Maxwellian[41]. Because of this, the "spectral temperature" is not a true temperature, but can be thought of as an average electron energy over some predefined range of energies. For the data shown in Fig. 3.3.2 this predefined energy range is chosen to between 4 keV and 20 keV, and 30 and 60 keV. Fig. 3.3.2 shows that the spectral temperatures increase at low microwave powers. At larger microwave powers, in this case, greater than about 150 W, the spectral temperatures, when calculated using a fit range of 4-20 keV, saturate with respect to microwave power. With a fit range of 30-60 keV,

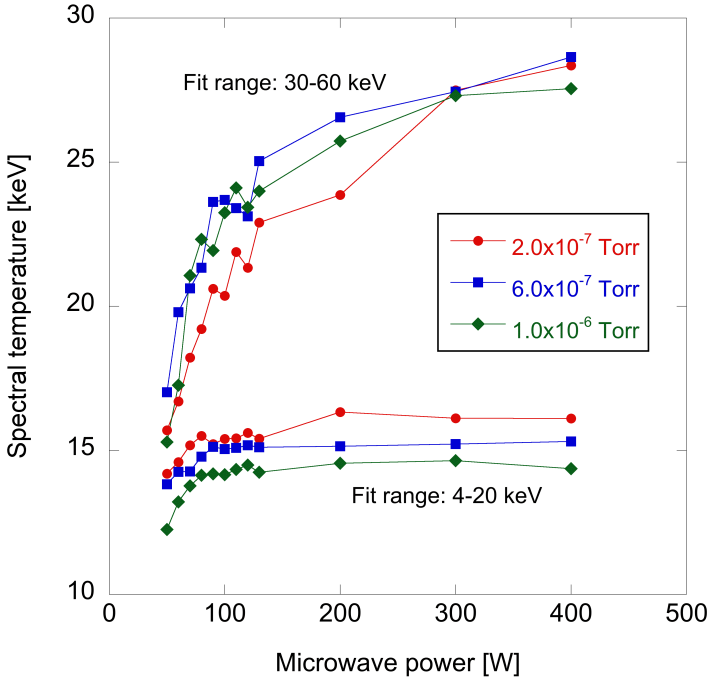


Figure 3.3.2: Spectral temperatures as a function of microwave power and neutral pressure. Argon plasma.

the saturation of spectral temperatures is not as noticeable. Increases in neutral pressure cause the spectral temperature to decrease for a fit range of 4-20 keV. There is no distinct trend with pressure with a fit range of 30-60 keV.

To calculate the x-ray power at a particular energy the following formula is used:

$$P_{h\nu} = \frac{N_{h\nu} h\nu}{t_{acq}}, \tag{3.3.2}$$

where $N_{h\nu}$ is the number of counts a certain energy, $h\nu$ is the energy, and $t_{acq}$ is the acquisition time of the spectra. To calculate the total x-ray power in a given spectra, the power at each energy is simply summed up:

$$P_{Total} = \sum_{h\nu} P_{h\nu} = \sum_{h\nu} \frac{N_{h\nu} h\nu}{t_{acq}}. \tag{3.3.3}$$

The x-ray power shown in Fig.'s 3.3.3 and 3.3.5 is the x-ray power produced by confined electrons in the small volume of plasma (approximately $890\ mm^3$) that falls within the solid angle defined by the collimator. The assumption made, then, is that the observed behavior in a small volume of plasma is representative of the plasma as a whole.

A plot of x-ray power versus microwave power, for three different neutral pressures, is shown in Fig. 3.3.3. The plot shows x-ray power increases as the logarithm of the microwave power. Because of this, the intensities of x-rays at larger microwave powers seem to saturate,

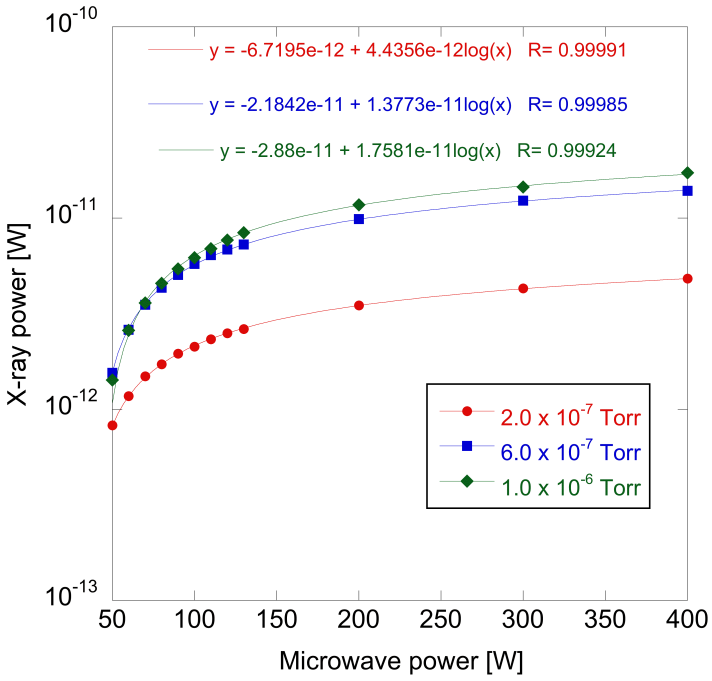


Figure 3.3.3: Calculated x-ray power at different microwave powers and neutral pressures. Argon plasma.

regardless of neutral pressure. The x-ray power is calculated with an x-ray energy range of 2-70 keV, but even if energy ranges of 4-20 keV or 30-60 keV are used to calculate x-ray power, the trend shown in Fig. 3.3.3 remains identical. The data in Fig. 3.3.3 also indicate that higher neutral pressures lead to greater x-ray intensities over a large portion of the microwave power range.

Figure 3.3.4 presents the data in Fig. 3.3.3 in a different manner. In this case the ordinate is the ratio of calculated x-ray power to microwave power, normalized by the maximum value of that ratio. A larger value of this ratio corresponds to a larger x-ray intensity per unit of input microwave power. For all three neutral pressures shown in Fig. 3.3.4 there is a peak in this power ratio, indicating an optimum combination of microwave power and neutral pressure for x-ray production. As neutral pressure is increased, the peak in x-ray efficiency moves to higher microwave powers. It can also be seen in Fig. 3.3.4 that at higher microwave powers having a larger neutral pressure produces more x-rays per unit of input microwave power. While, at the lowest microwave powers, x-rays are more efficiently produced at low operating neutral pressure.

To complete the low energy x-ray study, the effect of magnetic field configuration was also investigated. To change the magnetic field the currents going into the solenoids were simply adjusted up or down. Doing so causes several important magnetic field parameters, e.g., mirror ratio, and slope of the magnetic field in the resonance zone, all to change. Although the data in Fig. 3.3.5 is plotted as a function of $B_{min}/B_{ECR}$ only, it is important to realize that this is not a true parametric study, in that more than one magnetic field parameter is changing at a time.

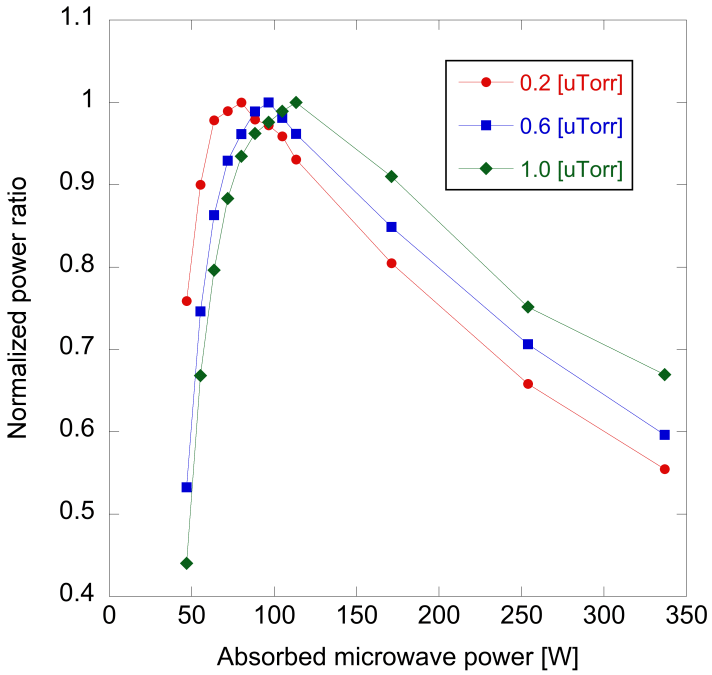


Figure 3.3.4: Normalized ratio of calculated x-ray power to microwave power as function of microwave power. Argon plasma.

Figure 3.3.5a shows a plot of calculated x-ray power as a function of the ratio of $B_{min}/B_{ECR}$. It is seen that the calculated x-ray power increases more or less linearly as the currents into the solenoids are increased, regardless of the range of energies used to calculate the x-ray power. In Fig. 3.3.5b the spectral temperatures are shown for two different fit ranges. For a fit range of 4-20 keV, the spectral temperature is relatively insensitive to changes in $B_{min}/B_{ECR}$. However, for a fit range of 30-60 keV, the spectral temperature almost monotonically increases with $B_{min}/B_{ECR}$.

### 3.3.2 Diamagnetic loop parametric studies

Figure 3.3.6 shows an example of an unintegrated signal from the diamagnetic loop. The initial, positive spike shown in Fig. 3.3.6 is due to the formation of the plasma. The second, negative spike occurs when the microwave power is turned off and the plasma begins to decay. The voltage shown in Fig. 3.3.6 is proportional to rate of change plasma formation, and so the plasma forms more rapidly than it decays. This trend remains consistent for all data points.

The effect of that microwave power has on the diamagnetic signal is shown in Fig. 3.3.7. In Fig. 3.3.7a the unintegrated signal at plasma ignition is shown as a function of time and microwave power. As the input microwave power is increased the maximum induced voltage in the loop also increases. The time scales, i.e., rise and fall times of the loop signal, do not change in a significant manner. An estimate of the plasma energy density, calculated using Eq. 2.1.42 and normalized by the energy density at 370 W of microwave power, is shown in Fig. 3.3.7b. As with the calculated x-ray power, the plasma energy density increases with

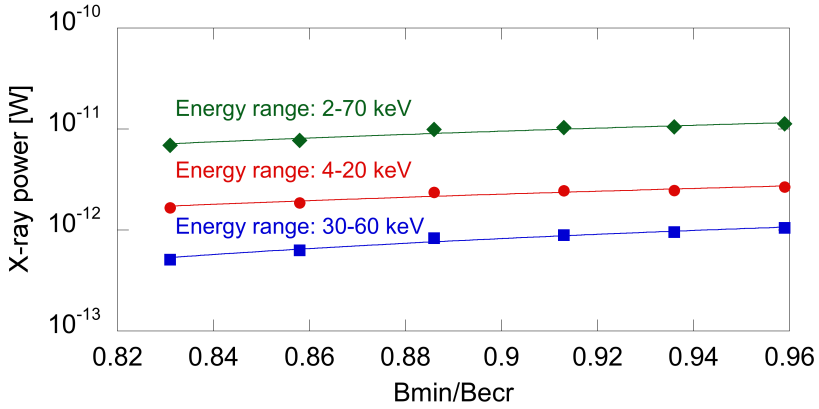


(a) Calculated x-ray power as function of Bmin/Becr. X-ray power calculated over three energy ranges.

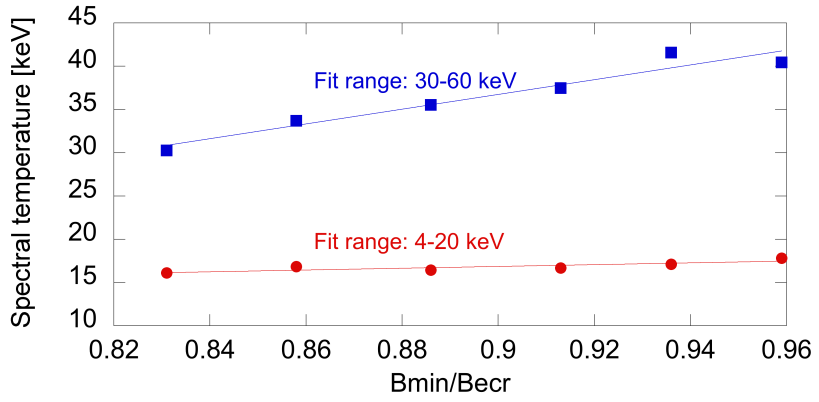


(b) Spectral temperature as function of Bmin/Becr.

Figure 3.3.5: Effect of magnetic field configuration on x-ray power and spectral temperature. Argon plasma.

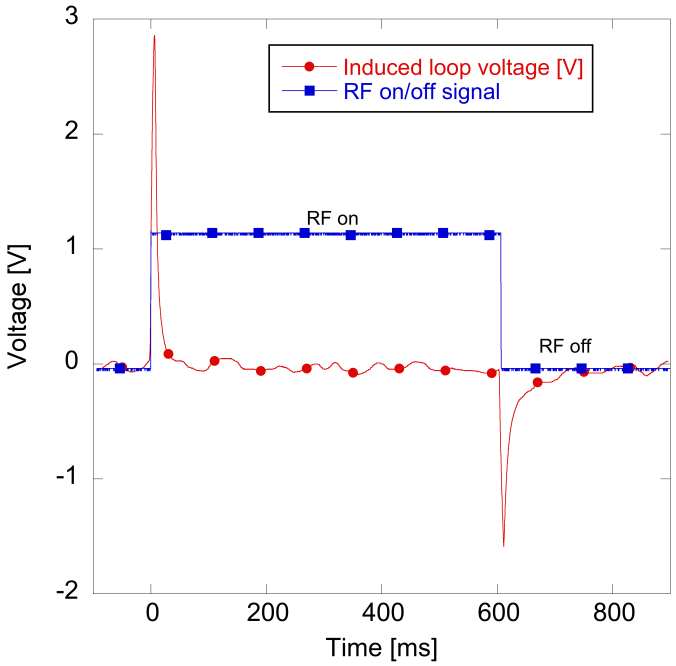


Figure 3.3.6: Example of raw, unintegrated signal from diamagnetic loop. Argon plasma. 150 W microwave power.

microwave power, and also increases in a nonlinear, logarithmic manner.

Shown in Fig. 3.3.8 are the unintegrated diamagnetic loop signal as a function of time and neutral pressure, and the plasma energy density as a function of neutral pressure. The maximum induced voltage is seen to decrease from a value of approximately 8 V at the highest pressure to a little over 5 V at the lowest pressure. The time required to reach the maximum rate of change of plasma formation is delayed by approximately 4 ms as pressure is decreased from 1.2 $\mu$Torr to 0.3 $\mu$Torr. The plasma energy density, as shown in Fig. 3.3.8b, rapidly reaches saturation as the neutral pressure is increased.

Lastly, the effect that the magnetic field has on the diamagnetic signal and plasma energy density is shown in Fig. 3.3.9. As noted earlier, this is not a true parametric study, as several parameters (for example, mirror ratios at injection and extraction and the gradients of the magnetic field in the resonance zones) describing the magnetic field configuration are changing as the current into the solenoids varies. Similar to the trend observed with x-ray power as a function of $B_{min}/B_{ECR}$, plasma energy density is also seen to increases with that same ratio. The maximum induced voltage increases with $B_{min}/B_{ECR}$, but the time at which the diamagnetic signal first appears does not seem affected.

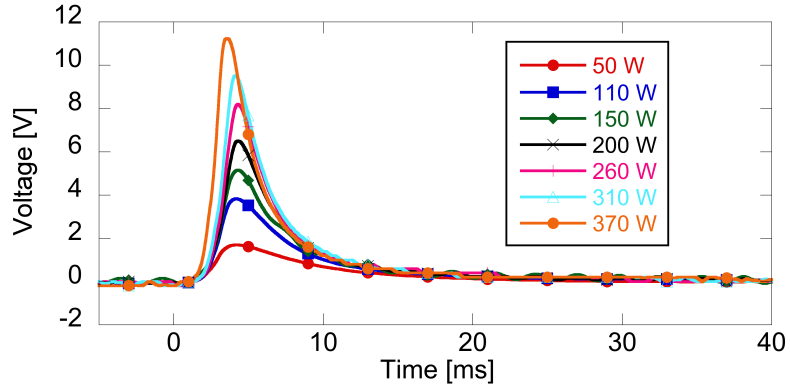


(a) Unintegrated diamagnetic loop signal as function of time and microwave power.

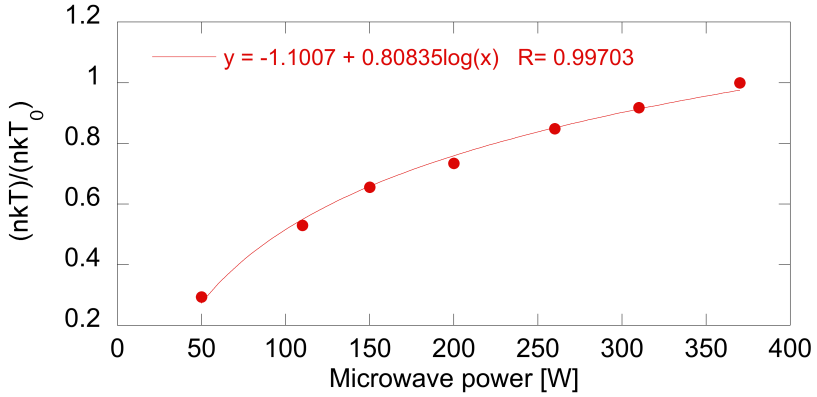


(b) Normalized plasma energy density as a function of microwave power.

Figure 3.3.7: Effect of microwave power on diamagnetic signal at plasma ignition. Argon plasma. 600 ms on/off.

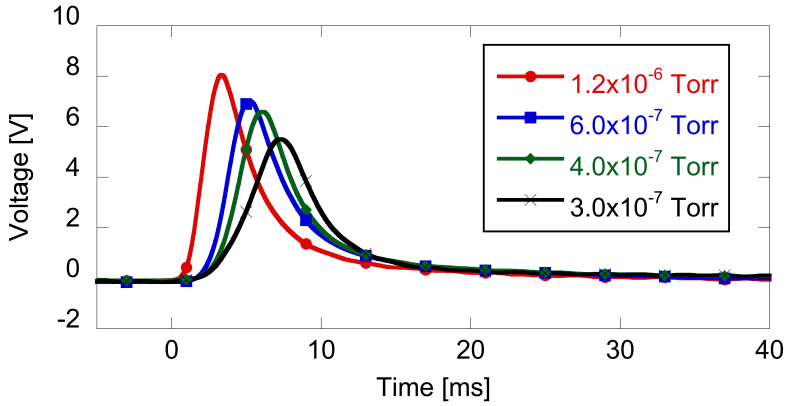


(a) Unintegrated diamagnetic loop signal as a function of time and neutral pressure.

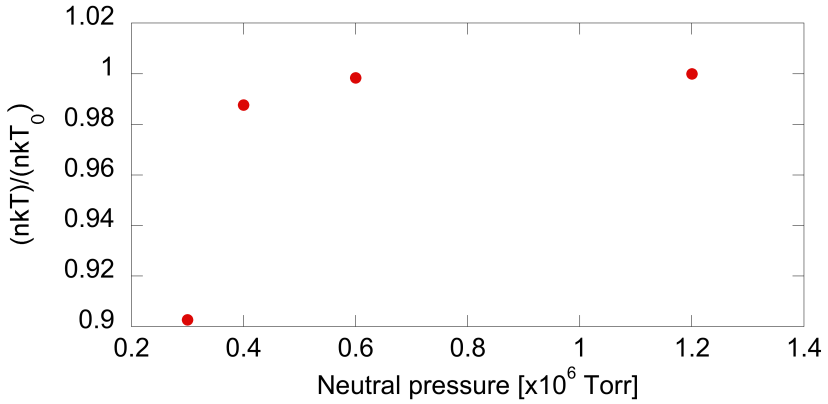


(b) Normalized plasma energy density as a function of neutral pressure.

Figure 3.3.8: Effect of neutral pressure on diamagnetic signal at plasma ignition. Argon plasma. 600 ms on/off.

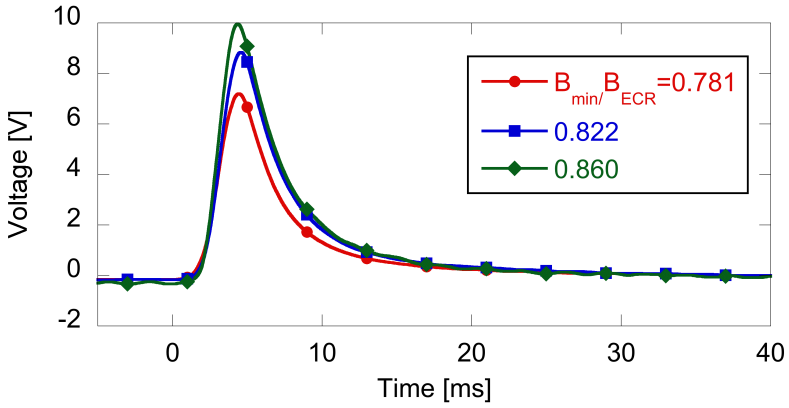


(a) Unintegrated diamagnetic loop signal as a function of time and Bmin/Becr.

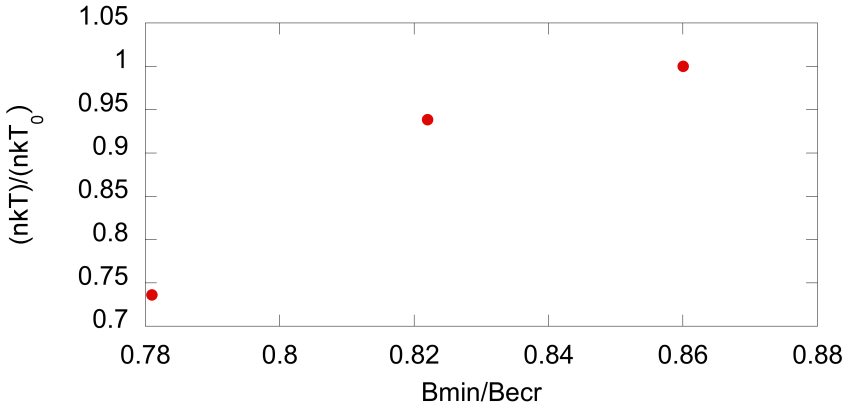


(b) Normalized plasma energy density as a function of Bmin/Becr.

Figure 3.3.9: Effect of magnetic field on diamagnetic signal at plasma ignition. Argon plasma. 600 ms on/off.

## 3.4 Discussion of results

### 3.4.1 Saturation of x-ray power and plasma energy density with microwave power

Previous studies, using a 10/14 GHz ECR ion source[54] and an 18/28 GHz ECR ion source[34], have shown a linear scaling of x-ray power with microwave power (it should be noted, that these studies focused on x-rays with energies greater than approximately 50 keV). Figure 3.3.3 shows that the x-ray power emitted by the confined plasma electrons behaves not in a linear fashion, but instead, in a logarithmic fashion with respect to the microwave power. Initially, there is a fast rise of x-ray power, but as microwave power continues to increase, the rate of increase of x-ray power becomes smaller. The x-ray power seems to saturate. Spectral temperatures, as shown in Fig. 3.3.2, and the diamagnetic signal, Fig. 3.3.7b, also show the trend of saturating at higher microwave powers.

For a non-relativistic, Maxwellian plasma the x-ray power per unit volume, in CGS units, can be written[45]:

$$\frac{dW}{dVdt} = 1.4 \times 10^{-27} T^{\frac{1}{2}} n_e n_i Z^2 \bar{g_B}, \tag{3.4.1}$$

where $T$ is temperature of the plasma electrons, $n_e$ is the electron density, $n_i$ is the ion density, $Z^2$ is the square of the average charge state of the ions in the plasma, and $\bar{g_B}$ is the frequency average of the velocity averaged Gaunt factor. The Gaunt factor is a quantum mechanical correction factor of order one. Assuming quasi-neutrality, $n_e \approx Zn_i$, this equation is rewritten as:

$$\frac{dW}{dVdt} \approx 1.4 \times 10^{-27} T^{\frac{1}{2}} n_e^2 Z, \tag{3.4.2}$$

showing that the radiated power per unit volume is proportional to the electron density squared, the square root of temperature, and the average charge state of the ions.

The diamagnetic signal is proportional to the energy density of the plasma, which can be approximated as: $nkT = n_i kT_i + n_e kT_e$. In typical ECR ion source plasmas, the energy density will be dominated by warm and hot electron populations[38]. Similar to the x-ray power, the plasma energy density is also a function of electron energy and density.

For the x-ray power and energy density to saturate, then, some mechanism must exist that limits the growth of either the electron energy or the electron density, or both. Perret *et al.[41]* have suggested rf-induced pitch-angle scattering as the possible means for this saturation. Pitch-angle scattering refers to the change in an electron's pitch angle that can occur during an interaction between the electron and the magnetic field of the wave. As microwave power is increased, the diffusion coefficient due to this interaction increases. This can be seen in the following equation[18]:

$$D_{\mu\mu} = \pi \left( \frac{eE}{2m_e} \right)^2 \frac{d}{L\omega} \left( \frac{v}{v_\phi} \right)^2, \tag{3.4.3}$$

where $E$ is the electric field strength, $d$ and $L$ are characteristic length scales, $\omega$ is the wave

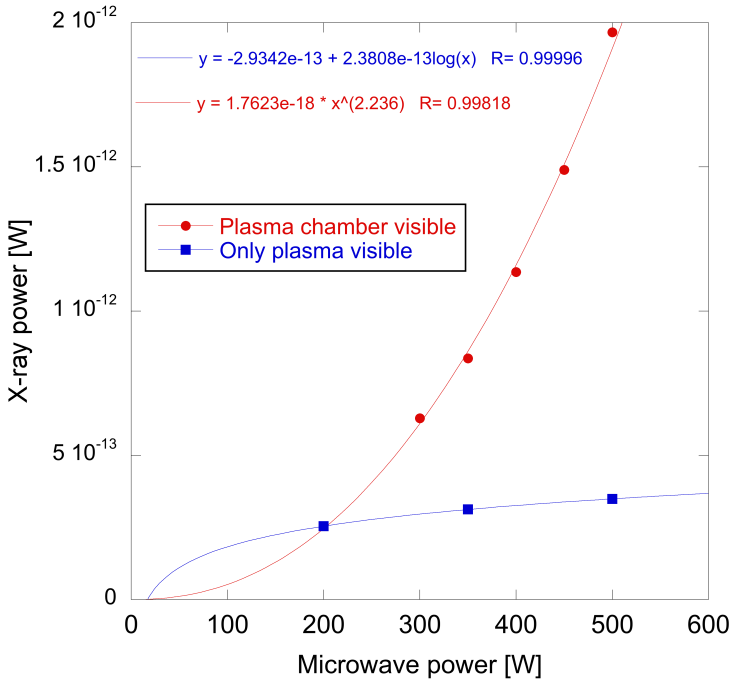


Figure 3.4.1: Plot of total x-ray power versus microwave power, both with and without the vacuum chamber structure visible to a NaI(Tl) x-ray detector . Measured radially. Argon and oxygen plasma.

frequency, $v$ is the velocity of an electron, and $v_\phi$ is the wave phase velocity. If one assumes that the average electric field strength in the plasma chamber increases with microwave power, it is immediately obvious from Eq. (3.4.3) that the diffusion coefficient increases. Eventually, as microwave power continues to increase, the loss rate of the hot electrons will balance with their creation rate, thus, limiting the electron energy and density.

Equation (3.4.3) also may offer insight into why the studies performed on the 10/14 GHz and 18/28 GHz ECR ion sources did not show signs of electron density and energy saturation. Girard *et al.*[18] have previously shown that the greater the ratio of cutoff density (the cutoff density is proportional the wave frequency squared) to electron density, the larger the phase velocity. Hence, larger microwave frequencies lead to larger phase velocities, and smaller diffusion coefficients. To reach the saturation point of the 10/14 GHz and 18/28 GHz sources, even higher powers than those used in the previous studies may need to be applied.

If rf-induced pitch-angle scattering is responsible for the observed saturation of x-ray power and plasma energy density, then it is reasonable to assume that the flux of electrons lost from the plasma will increase with the microwave power. The implication of this is that the x-ray flux created by electrons striking solid surfaces should not saturate. Instead, it should steadily increase as the microwave power is raised. Data taken during a different experiment, also carried out on the 6.4 GHz ECR, shows this trend, and is discussed below.

Figure 3.4.1 shows a plot of the x-ray power versus the microwave power when only the plasma is visible to the detector, and also when the plasma chamber walls are visible to the

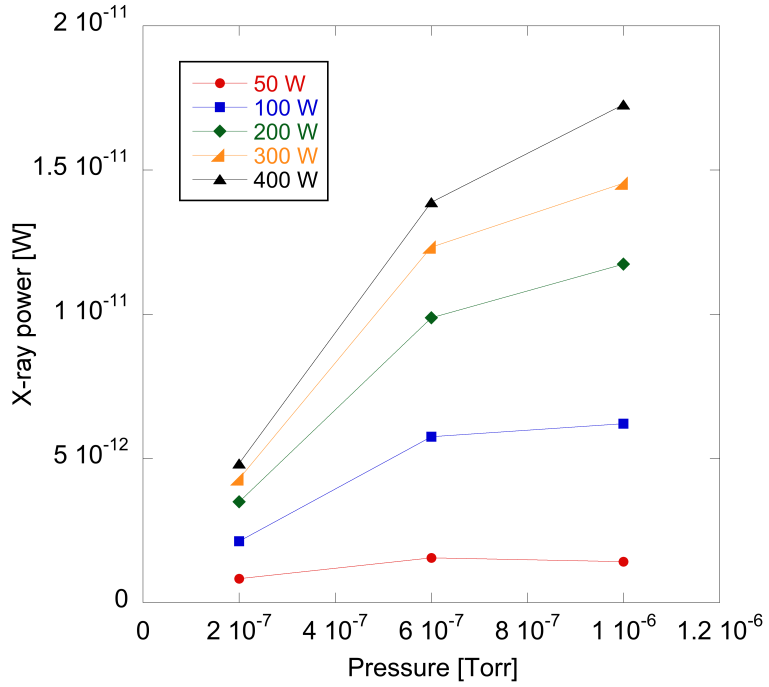


Figure 3.4.2: Calculated x-ray power at different neutral pressures. Argon plasma.

detector. The experimental setup used to produce the data in Fig. 3.4.1 is discussed in greater detail in reference [40]. When only the plasma is visible to the detector, the previously discussed logarithmic increase of x-ray power with microwave power is again seen. However, when the collimation is adjusted such that the plasma chamber walls are visible to the detector, the x-ray power increases almost quadratically with microwave power.

### 3.4.2 Pressure trends

The spectral temperature, fit to an energy range of 4-20 keV, decreases as neutral pressure is increased. This is in agreement with computer models [18, 10] that also predict that the mean energy of electrons decreases as the neutral pressure increases. The "mean energy" discussed in these models refers to a mean over all electrons in the simulation, so it is related to the spectral temperature, but not identical. From a physical standpoint, the fact that spectral temperature decreases as the neutral density increases makes sense, as electrons will suffer more frequent collisions with neutrals. More frequent collisions, in turn, will scatter electrons into the loss cone more rapidly.

Girard *et al.* [18] also predict that the electron density first experiences a period of rapid increase with neutral density. This is followed by a period of more gradual change. X-ray power and plasma energy density are both functions of electron density, and thus the trends shown in Fig. 3.3.3 and Fig. 3.3.8 agree with the model. The trend of x-ray power with neutral pressure is shown in a more explicit manner in Fig. 3.4.2. Here the saturation of x-ray power with neutral pressure is much more apparent, especially at microwave powers below 200 W.

| $B_{Min}/B_{ECR}$ | 0.831 | 0.858 | 0.886 | 0.913 | 0.936 | 0.959 |
|---|---|---|---|---|---|---|
| Gradient in resonance zone (extraction) [G/cm] | -95.8 | -91.1 | -84.4 | -75.8 | -66.0 | -53.4 |
| Gradient in resonance zone (injection) [G/cm] | 97.7 | 92.7 | 85.4 | 76.6 | 64.7 | 49.4 |
| Mirror ratio (extraction) | 1.654 | 1.648 | 1.646 | 1.642 | 1.629 | 1.616 |
| Mirror ratio (injection) | 2.102 | 2.106 | 2.107 | 2.105 | 2.118 | 2.123 |
| Axial distance between resonance zones [cm] | 15.0 | 13.5 | 11.8 | 10.1 | 8.6 | 6.7 |

Table 3.1: Summary of magnetic field parameters used in low energy x-ray study.

Finally, the delay of plasma breakdown with neutral pressure, as shown Fig. 3.3.8a, is consistent with data taken by other research groups[50]. The precise breakdown time will also depend on the microwave pulse pattern and the number density of electrons diffusing into the main stage from the ECR first stage. For example, it has been observed over the course of this study that electrons can remain in the plasma chamber for nearly a full second after the microwave power has been turned off. The presence of these "seed" electrons greatly reduces the time required for plasma ignition[50].

### 3.4.3 Magnetic field trends

To change the magnetic field configuration of the ECR, the magnitude of the solenoid currents was varied. Because the ECR sextupoles are permanent magnets, the radial field is fixed. Table (3.1) summarizes the changes to various magnetic field parameters as a function of $B_{Min}/B_{ECR}$, and Fig. 3.4.3 shows the axial magnetic field profile for two data points. The data shown in Table (3.1) are calculated values based on a magnetic field model of the ECR. The mirror ratio, as shown in Table (3.1), is defined as the ratio $B_{Max}/BMin$.

By far, the most dramatic changes that occur as $B_{Min}/B_{ECR}$ increases is the drop in the gradient of the magnetic field near the resonance point, and the decrease in axial distance between the extraction and injection resonance zones. Simple ECR heating models show that the energy gain of electrons is inversely proportional this slope[36]. Previous experimental studies have confirmed this theoretically predicted behavior with the observation of increased spectral temperatures as the slope is decreased[34, 56].

In this study spectral temperature is seen to either increase slowly with $B_{Min}/B_{ECR}$, or to remain nearly constant with $B_{Min}/B_{ECR}$, depending on the fit range. Electrons with a spectral temperature, or mean energy, of approximately 16 keV appear to be less sensitive to changes in magnetic field configuration than electrons with a mean energy of approximately 30-40 keV.

In general, to reach higher energies electrons will need to make multiple passes through the resonance zone. In a magnetic field configuration with a lower slope in the resonance zone an electron will require, on average, fewer traverses to reach a given energy. Competing with the heating process is the scattering of electrons into the loss cone of the mirror field, with less energetic electrons scattered more rapidly ($\tau_{ei} \sim T_e^{3/2}$). The collision time of the low energy, cold electrons might close to the average time required for a cold electron to reach 30-40 keV. Thus, the population of 30-40 keV electrons will be quite sensitive to the slope of the magnetic

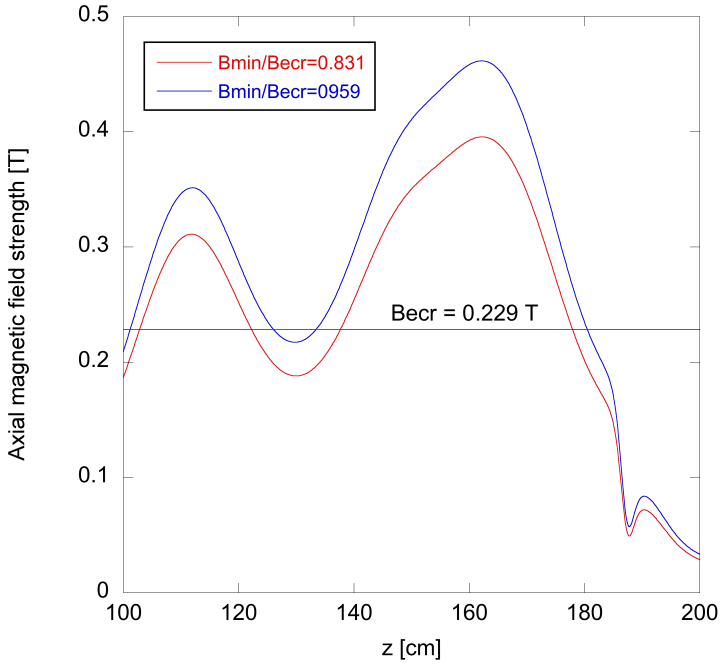


Figure 3.4.3: Axial magnetic field profile.

field. Conversely, the average time required to reach 16 keV may be much lower than the collision time, and, thus, this population of electrons is not sensitive to a change of slope of the magnetic field in the resonance zone.

The fact that x-ray power and the plasma energy density are seen to increase as the slope in the resonance zone decreases is also in agreement with theory. Decreasing the slope leads to an increase in the warm and hot electron population, due to the more efficient heating process. Larger populations of warm and hot electrons, in turn, result in greater x-ray intensities and plasma energy densities.

It is interesting to note that stochastic heating models predict that the maximum energy gained, in both the stochastic and adiabatic limit, is proportional to the axial distance between resonance zones[53]. Based on this model, one would expect to see decreases in x-ray power and spectral temperature as $B_{Min}/B_{ECR}$ is increased. The fact that opposite trend occurs may indicate that the gradient of the magnetic field in the resonance zone plays a primary role in determining the energy distribution of the warm and hot electrons.

## 3.5 Conclusions

In this chapter it has been shown that for a 6.4 GHz ECR ion source, both the x-ray power due to confined electrons and the plasma energy density behave logarithmically with microwave power. The x-ray flux created by electrons lost from the plasma, however, does not saturate. Thus, the small increase in plasma density that occurs at high microwave powers will be accompanied by a large increase in total x-ray power.

X-ray power and plasma energy density are also shown to saturate with neutral pressure, and to increase nearly linearly as the gradient of the magnetic field in the resonance zone is decreased. All of these findings are in agreement with the theoretical models describing ECR ion source plasmas that were discussed earlier in the paper.

To extend this study, it would be interesting to take both diamagnetic loop and low energy x-ray measurements on a higher frequency ECRIS. Particular attention should be paid to saturation of electron energies and densities with microwave power. From a theoretical standpoint, the saturation is expected to occur at larger microwave powers than those used in this study.

# Chapter 4

# Time scales in an ECR plasma

In the previous chapter we focused on understanding how the plasma energy density, as calculated based on the integrated diamagnetic signal, changed under various ECRIS operating conditions, and ignored time scales. In this chapter we will use the diamagnetic signal to discuss the timescales of various processes in an ECR plasma. In particular we focus on how the microwave power, neutral pressure, and magnetic field configuration affect the formation and decay times of the diamagnetic signal. In order to understand how plasma energy density is related to the appearance of different ionic charge states, we compare extracted ion currents (measured with a Faraday cup) to the diamagnetic signal for both an helium plasma and an argon plasma. Finally, we explore how the initial number density of electrons in the plasma chamber at the beginning of a microwave pulse affects the plasma breakdown properties, and compare the diamagnetic loop signal to the ratio of reflected to forward microwave power.

## 4.1 Experimental setup

Data shown in this chapter were taken on the LBNL 6.4 GHz ECR, described in a previous chapter. The experimental setup for the diamagnetic loop has also been discussed earlier, in Chapter 3. Faraday cup currents were recorded on an oscilloscope simultaneously with the diamagnetic loop signal. For comparison purposes, an attempt was made to record the diamagnetic signal on the LBNL 14 GHz AECR-U, but due to time constraints and poor positioning of the loop, we were unsuccessful.

Because of currents that may be induced in the aluminum support ring, on which the diamagnetic loop is mounted, we reiterate that we are comparing data on a relative basis only (see Chapter 3). The plots in the next section will show decay and formation times, but these should only be used to compare to other times. We are looking for trends, rather than absolute values.

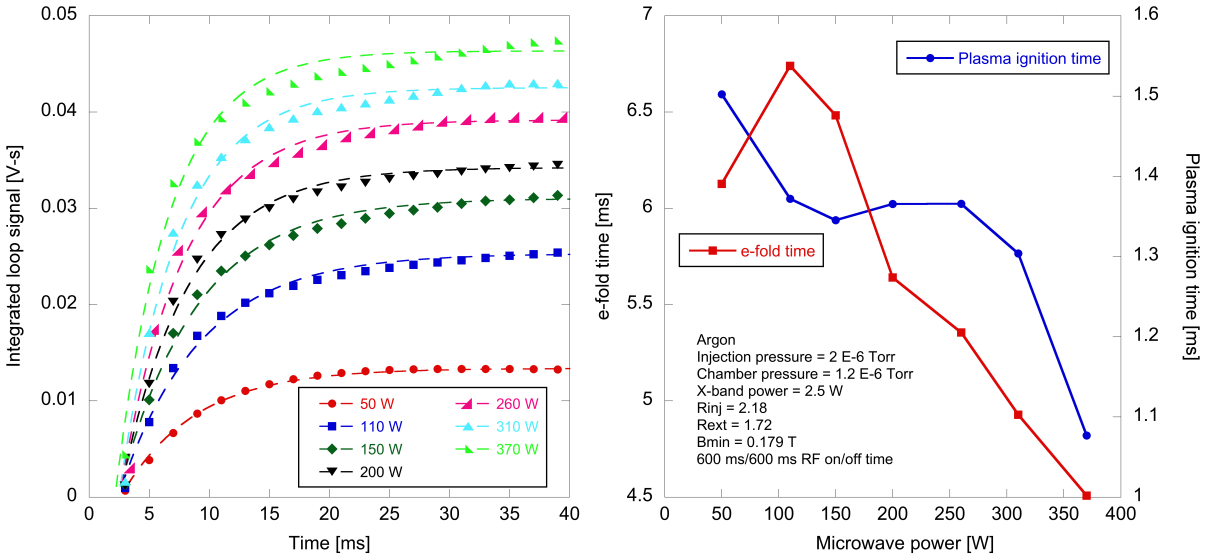


Figure 4.2.1: Left: Integrated diamagnetic loop signal as a function of time and microwave power at the beginning of the microwave pulse. Right: e-fold and plasma ignition time as function of microwave power.

## 4.2 Experimental results: Effect of microwave power on diamagnetic signal formation and decay

Figure 4.2.1 shows the integrated diamagnetic loop signal as a function of time, and the "e-fold" time and the plasma ignition time as a function of microwave power at the beginning of the microwave pulse. Time is measured from the leading edge of the microwave pulse. The duty factor of the klystron is set to 50%, with an on and off time of 600 ms, and the source settings are provided in the figure. The dashed lines are exponential fits to the integrated loop signal data of the form: $y = m_1 + m_2\,(1 - \exp\,(-m_3 x))$. The constant $m_3$ is used to calculate the "e-fold" time, shown in the plot on the right of Fig. 4.2.1, by simply inverting it. The plasma "ignition time" is calculated as the x-intercept of the exponential fit. It is the approximate time at which the diamagnetic signal becomes large enough to be measured, and is therefore not a true "plasma breakdown time." For brevity, however, we will continue to simply say "breakdown time" or "ignition time."

The e-fold time, the time that is required for the integrated loop signal to reach approximately 63% of its steady state value, is seen to decrease with microwave power (there is an initial increase in e-fold time when moving from 50 W to 110 W). The e-fold time at a microwave power of 370 W is approximately 33 % less than it is at 110 W. The plasma ignition time also shows a slight decrease, from approximately 1.5 ms to 1.1 ms, as the microwave power is increased from 50 W to 370 W.

In Fig. 4.2.2 the integrated loop signal and the e-fold time are shown at the end of the microwave pulse. The curve fits to the integrated loop data, in this case, are of the form: $y = m_1 + m_2\,(\exp\,(-m_3 x))$. We see a clear trend that the decay rate of the integrated diamag-

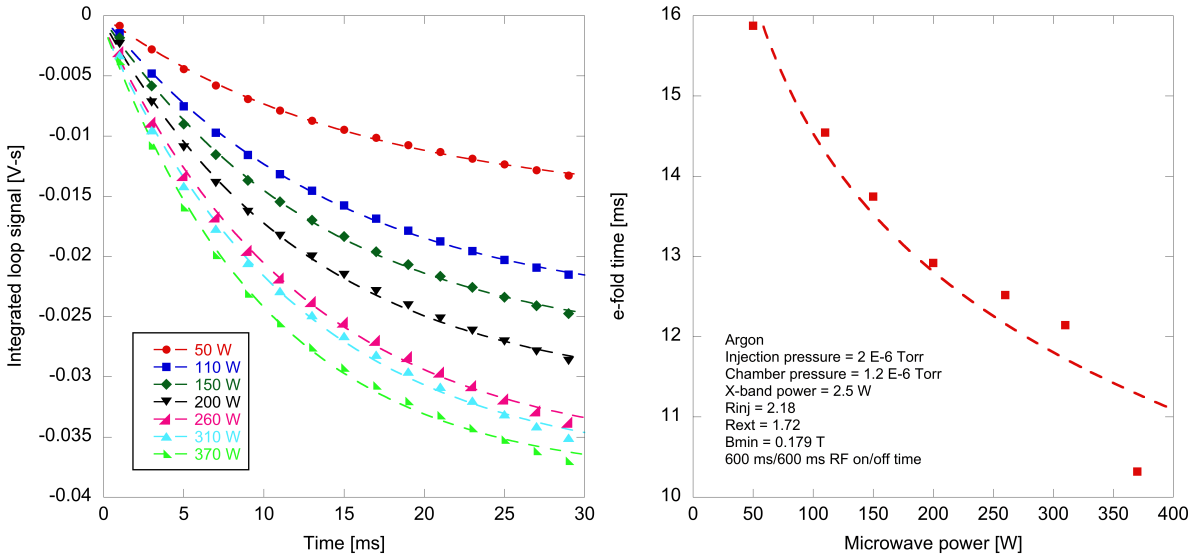


Figure 4.2.2: Left: Integrated diamagnetic loop signal as a function of time and microwave power at the end of the microwave pulse for identical source settings as those in Fig. 4.2.1. Right: associated decay e-fold time at end as function of microwave power.

netic loop signal increases (smaller e-fold time) with the microwave power. The red, dashed line in the plot of e-fold time versus microwave power is a logarithmic fit to the data, indicating, that the e-fold time decreases in a nearly logarithmic fashion with increasing microwave power (the fit is quite good, $R^2 = 0.991$, if the somewhat anomalous data point at 370 W were dropped. It is unknown why this data point falls so far from the trendline). If we compare e-fold times at beginning and end of the microwave pulse we can calculate that, on average, it takes approximately 2.3 times longer for the integrated loop signal to decay than it does to form.

Figures 4.2.3 and 4.2.4 show the same parameters as just discussed (integrated loop signal, e-fold time, and plasma ignition time), but at different source settings and with a shorter microwave pulse duration (225 ms versus 600 ms). The same trend in e-fold time with respect to microwave power at plasma ignition is still seen: as microwave power is increased, the e-fold time is decreased, indicating a faster plasma formation rate. The plasma ignition time, again, is relatively insensitive to microwave power level. Finally, Fig. 4.2.4 shows the same trend as that in Fig. 4.2.2: increasing microwave power causes the decay e-fold time to decrease. The red, dashed line is again a logarithmic fit to the data (excluding the data point at 62 W, which may fall far from the trend line because the neutral pressure, 5e-7 Torr, is too low for the plasma to be sustained at this power). As with the data shown in Fig.'s 4.2.1 and 4.2.2, this data suggests that the decay of the diamagnetic signal takes longer than the rise.

Previous studies [3, 4], in which the plasma diamagnetism of an 18 GHz ECRIS was measured, also observed a similar trend in rise and decay time versus microwave power. Namely, the authors saw that the characteristic times decrease with microwave power. In those studies the rise and decay time were calculated as: $\tau = {}^{dia}/_{s}$, where *dia* is the magnitude of the in-

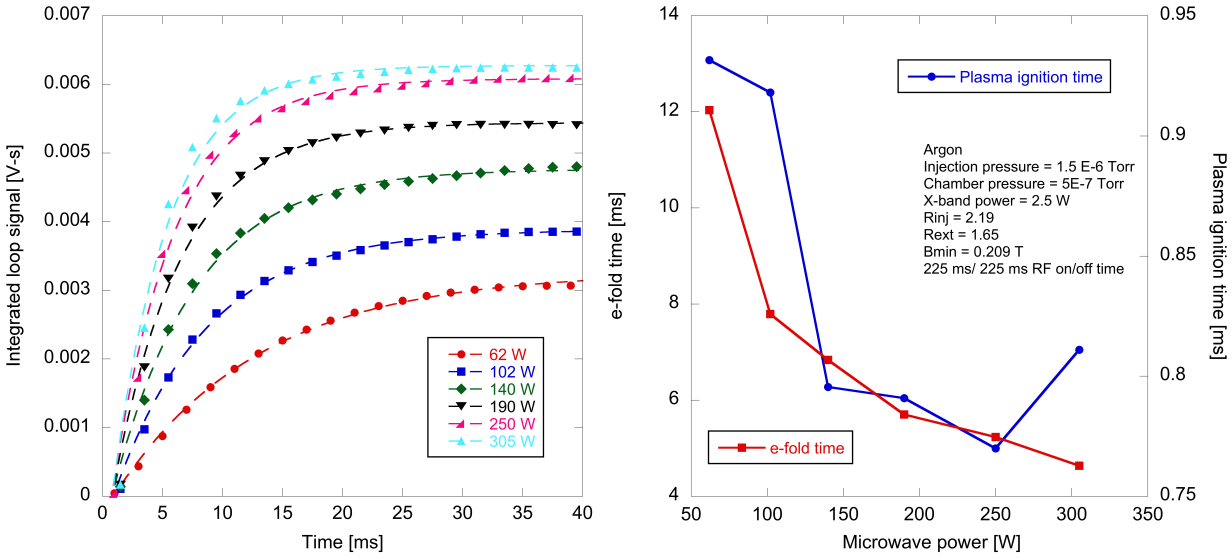


Figure 4.2.3: Left: Integrated diamagnetic loop signal as a function of time and microwave power at the beginning of the microwave pulse. Right: e-fold time and plasma ignition time as function of microwave power. Chamber pressure and RF on/off times decreased from those in Fig. 4.2.1.

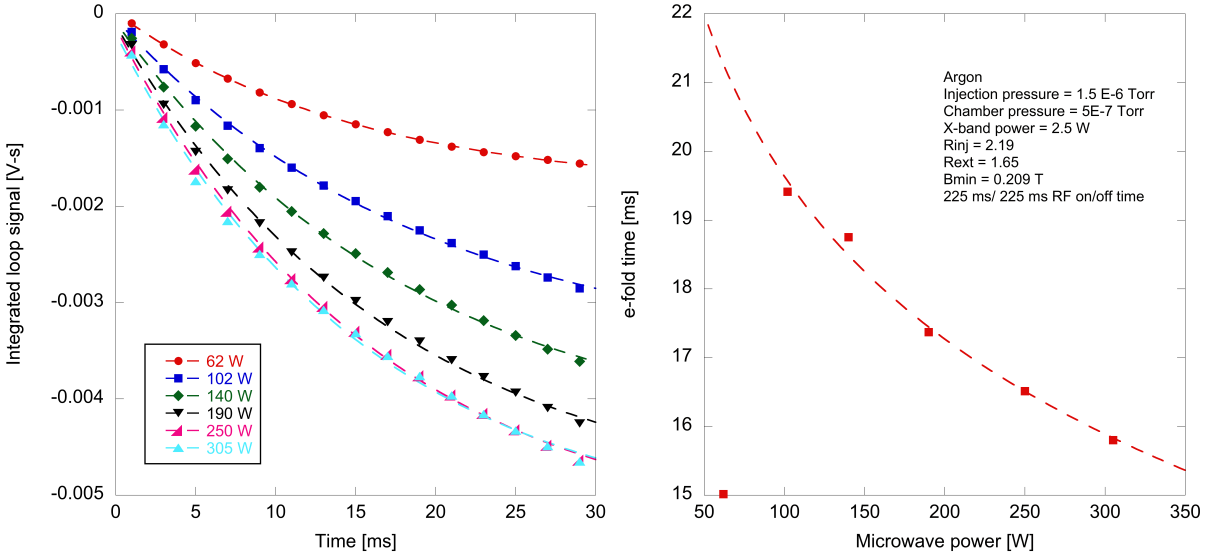


Figure 4.2.4: Left: Integrated diamagnetic loop signal as a function of time and microwave power at the end of the microwave pulse for identical source settings as those in Fig. 4.2.3. Right: associated decay e-fold time as function of microwave power.

tegrated diamagnetic signal at steady state, and $s$ is the slope of the diamagnetic signal right as the microwave power is either turned on or turned off. Furthermore, in those studies the formation time was always less than the decay time of the diamagnetic signal, as we observe here. The fact that the decay times decrease with microwave power make sense if we examine Eq. 2.1.9 (shown again for convenience):

$$\langle \nu_{ei} \rangle = \frac{\sqrt{2} n_i Z^2 e^4 ln\Lambda}{12\pi^{3/2}\varepsilon_0^2 \sqrt{m} T_e^{3/2}}.$$

As we have shown, except at very low powers, the electron "temperature" does not change significantly with microwave power (Fig. 3.3.2). The main result of increasing microwave power, then, is to increase the plasma density. From Eq. 2.1.9 we see that increasing plasma density, $n_i$, increases the collision frequency, and hence lowers the decay times.

In another study, by Tarvainen *et al*. [50], in which the current signal of the bias disk was used to study plasma breakdown processes, it was shown that the plasma breakdown time is almost independent of the microwave power. The time required to reach the peak bias disk current at the leading edge of the microwave pulse was measured for microwave powers ranging from 50 W up to 700 W, on a 14 GHz ECRIS, with microwave power off times of 6 s. Results showed that this time varied by less than approximately 3 ms over the entire range of powers. The lack of sensitivity of the plasma ignition time to microwave power, as we measure with the diamagnetic loop in this study, is verified by the results published by Tarvainen *et al.*.

## 4.3 Experimental results: Effect of neutral pressure on diamagnetic signal formation and decay

We next examine the impact that the neutral pressure has the diamagnetic signal formation and decay rates. In contrast to changes in microwave power, an increase or decrease in neutral pressure has a negligible effect on the formation e-fold time (Fig. 4.3.1). That is, neutral pressure does not seem to change the rate at which the plasma forms in a significant way. However, for the source settings and pulse pattern given in Fig. 4.3.1, the plasma ignition time is more than halved, when increasing the neutral pressure from $3 \times 10^{-7}$ Torr to $1.2 \times 10^{-6}$ Torr. The decay rate, as shown in Fig. 4.3.2, first undergoes a decrease with neutral pressure, and then steadily increases as neutral pressure is raised from $4 \times 10^{-7}$ Torr to $1.2 \times 10^{-6}$ Torr. The increase is slight (11.8 ms to 13.2 ms), but noticeable.

For different source settings and shorter microwave pulse pattern, the rise times and plasma ignition times follow the same trend with neutral pressure, as shown in Fig. 4.3.3. The rise time again decreases by a small amount, approximately 1 ms, as the neutral pressure is increased from $4 \times 10^{-7}$ Torr to $1 \times 10^{-6}$ Torr. Over this same range of neutral pressures, the plasma ignition time decreases from a value of 1 ms to 0.7 ms. The plasma ignition time, for these settings, occurs approximately 4 ms sooner, while the e-fold time at ignition is roughly the same when comparing to Fig. 4.3.1.

Neutral pressure has previously been shown to have a large impact on the plasma ignition

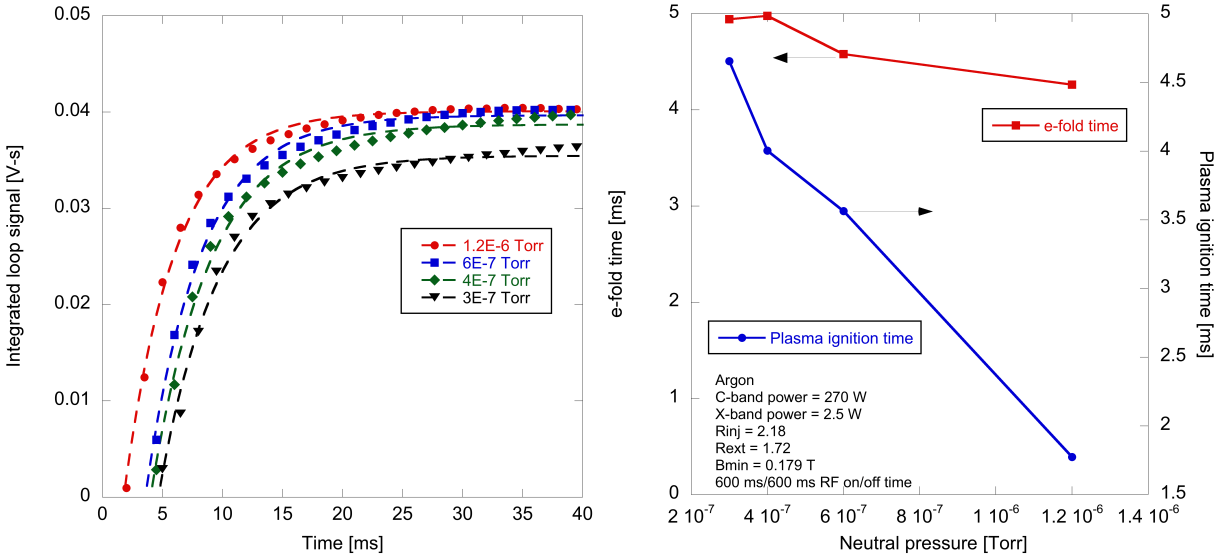


Figure 4.3.1: Left: Integrated diamagnetic loop signal as a function of time and neutral pressure at the beginning of the microwave pulse. Right: e-fold and plasma ignition time as function of neutral pressure.

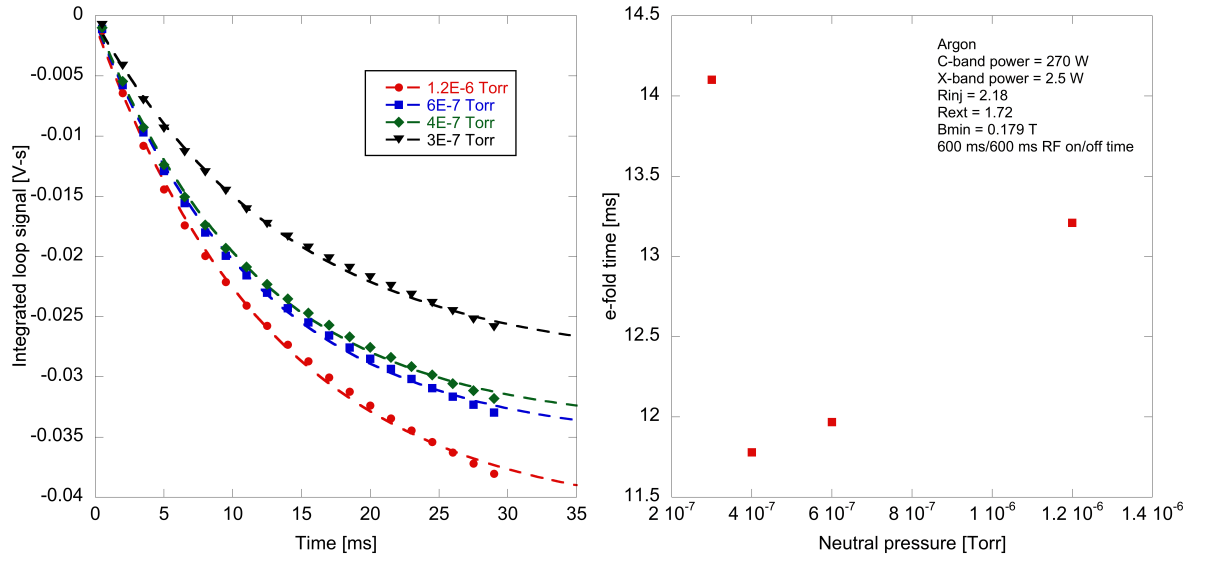


Figure 4.3.2: Left: Integrated diamagnetic loop signal as a function of time and neutral pressure at the end of the microwave pulse for identical source settings as those in Fig. 4.3.1. Right: associated decay e-fold time as function of neutral pressure.

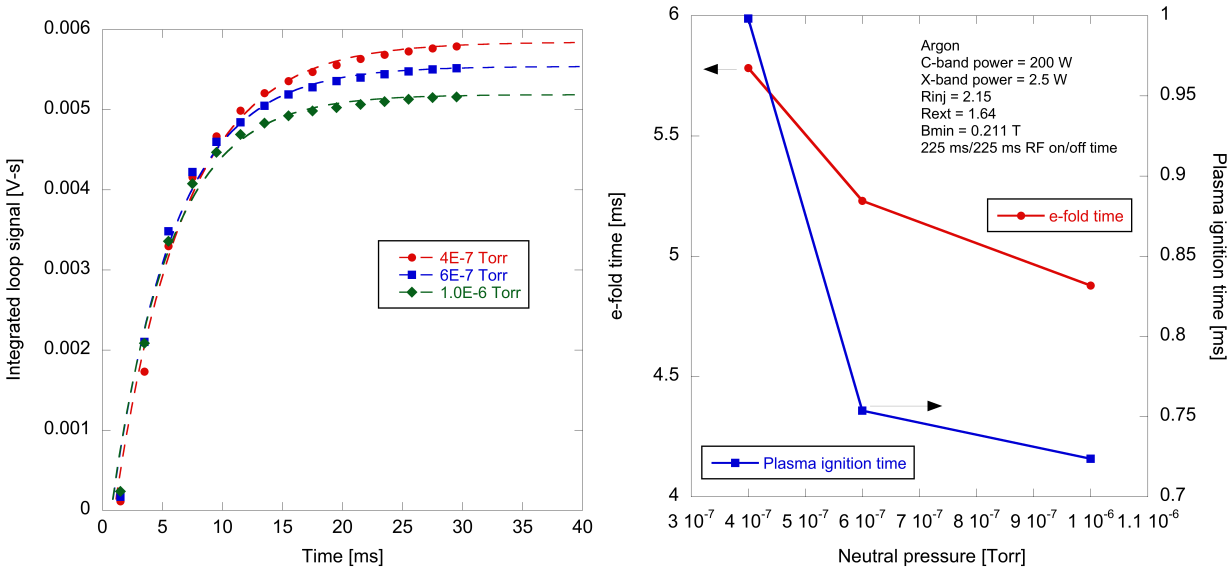


Figure 4.3.3: Left: Integrated diamagnetic loop signal as a function of time and neutral pressure at the beginning of the microwave pulse. Right: e-fold and plasma ignition time as function of neutral pressure. Microwave power and RF on/off times lower than those for the data shown in Fig. 4.3.1.

times. In the same study mentioned earlier [50], the authors showed that the time required to reach peak bias disk current steadily decreased as the neutral gas pressure was increased. For example, in a neon plasma, increasing the neutral pressure by a factor of approximately nine caused the plasma ignition time to have decreased by approximately a factor of 10. The range of pressures we examine in the current study is smaller, but we still observe an identical trend. As the neutral pressure is increased, the plasma ignition time (calculated as the x-intercept of an exponential fit to the integrated diamagnetic loop data in this case) decreases.

In the data shown in Fig. 4.3.3, for a microwave on and off time 225 ms (50% duty factor), the average plasma ignition time is approximately 0.8 ms. For the data in Fig. 4.3.1, with a microwave on and off time of 600 ms (again, a 50% duty factor), the average plasma ignition time is 3.5 ms. The data suggest, then, that having a shorter time between microwave pulses will cause the ignition time to decrease. Tarvainen *et al.* [50] again saw a similar trend. Measurements on a 6.4 GHz ECRIS showed that the time to reach 10% of the peak bias disk current was delayed as the separation between microwave pulses was increased. If the separation time was increased beyond a certain point, however, the ignition times became more randomized. The trend of faster plasma ignition with smaller microwave pulse separation is thought to be due to the relative abundance (or lack) of electrons in the plasma chamber. This effect will examined in more detail later in this chapter.

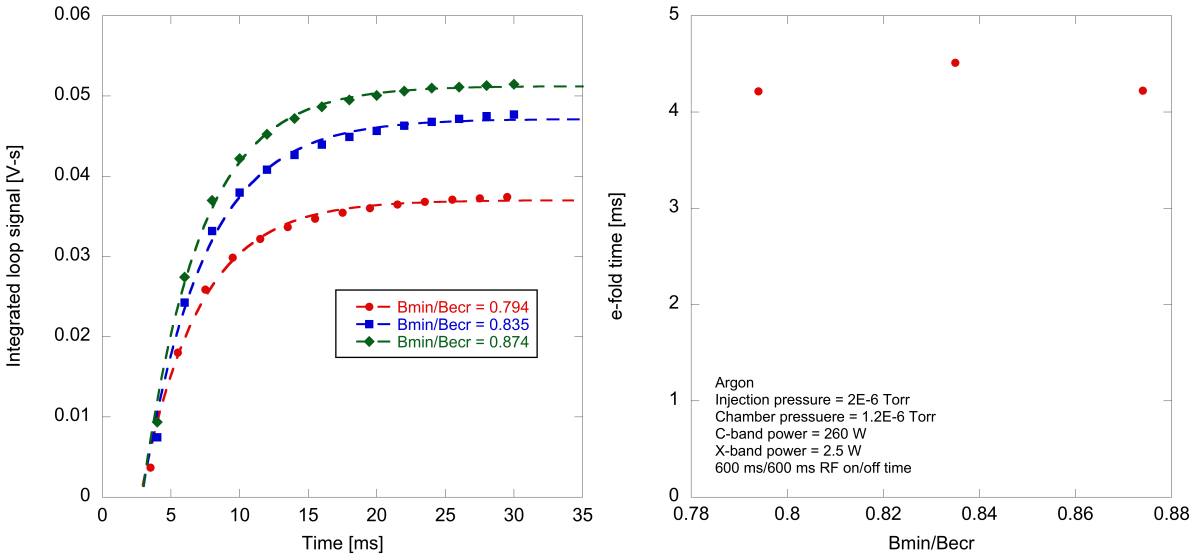


Figure 4.4.1: Left: Integrated diamagnetic loop signal as a function of time and Bmin/Becr at the beginning of the microwave pulse. Right: e-fold time as function of Bmin/Becr.

## 4.4 Experimental results: Effect of magnetic field on diamagnetic signal formation and decay

In Chapter 3 we showed the importance of magnetic field configuration, especially the gradient of the field in the resonance zone, on determining the steady state x-ray count rate and plasma energy density of the 6.4 GHz ECR. Results shown in this section, however, indicate that the rise and decay rates of the diamagnetic signal, and therefore the plasma energy density, are minimally affected by the specific magnetic field configuration. Figures 4.4.1 and 4.4.2 show the rise and decay e-fold times as functions of the the ratio of $B_{min}/B_{ecr}$. As just stated, they vary little over the range of $B_{min}/B_{ecr}$ ratios examined. The decay times are again greater, approximately three times as large, than the rise times. In Fig. 4.4.3 e-fold times at plasma ignition are shown for a different source operating point and a much shorter pulse pattern. There is a slight increase in e-fold time from 4.5 ms to 5.9 ms when $B_{min}/B_{ecr}$ is raised from 0.93 to 0.97, otherwise it again remains almost constant.

Assuming that the plasma in an ECRIS is partially ionized, and that $\omega_c \tau \gg 1$ ($\tau$ is the characteristic time required for a particles momentum to be changed significantly, i.e., the large angle scattering time), the perpendicular diffusion coefficient ( across magnetic field lines) for a particular species can be written:

$$D_{\perp PI} = \frac{KT\nu}{m\omega_c^2}, \tag{4.4.1}$$

where $\nu$ is the collision frequency between the species of charged particle and neutral gas atoms. The cyclotron frequency, $\omega_c$, is proportional to the magnitude of the local magnetic field (Eq. 2.1.6), and hence, the perpendicular diffusion coefficient is proportional to $1/B^2$. Thus, we might expect that increasing the magnetic field strength would increase the decay e-

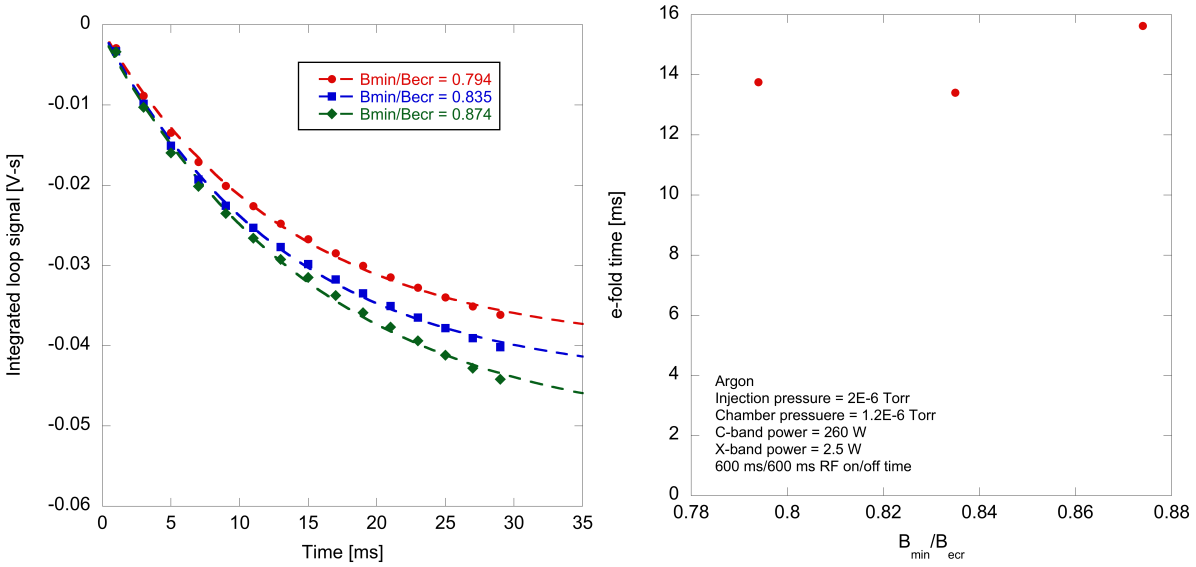


Figure 4.4.2: Left: Integrated diamagnetic loop signal as a function of time and Bmin/Becr at the end of the microwave pulse at identical source settings as those shown in Fig. 4.4.1. Right: associated decay e-fold time as function of Bmin/Becr.

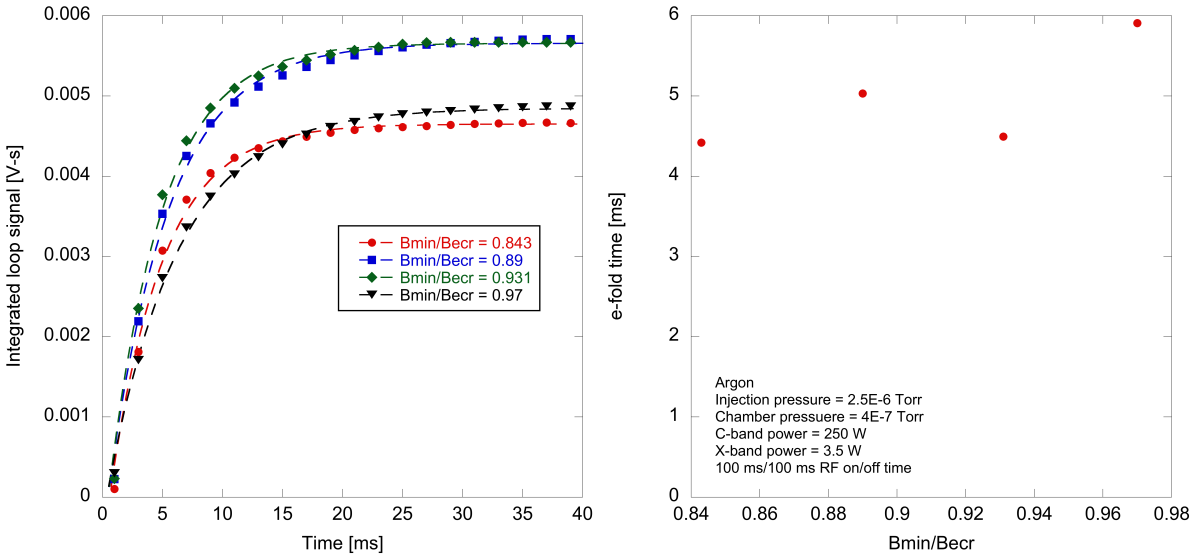


Figure 4.4.3: Left: Integrated diamagnetic loop signal as a function of time and Bmin/Becr at the beginning of the microwave pulse. Right: e-fold time as function of Bmin/Becr. Chamber pressure decreased, and RF on/off time lower compared to data in Fig. 4.4.1.

fold times. However, as clearly demonstrated in Fig. 4.4.2, this trend is not observed. Rather, the decay e-fold times are insensitive to changes in magnetic field strength over the range of field settings we examined.

The collision frequency, $\nu$, in Eq. 4.4.1 is proportional to the velocity of the electrons ($T^{1/2}$), and so the diffusion coefficient increases with energy electron

$$D_{\perp PI} \sim \frac{T^{3/2}}{B^2}. \tag{4.4.2}$$

As shown in Chapter 3 increasing the ratio $B_{min}/B_{ecr}$ can increase the spectral temperature (average energy) of electrons. It is conceivable, then, that any benefit (decreased diffusion coefficient) from the increase in magnetic field strength is offset by the increase in both $KT$ and $\nu$, with the end result that the decay e-fold times do not vary much with magnetic field strength ($B_{min}/B_{ecr}$), as the data seems to indicate.

In the case of a fully ionized plasma the perpendicular diffusion coefficient can be written:

$$D_{\perp FI} = \frac{\eta_{\perp} n (KT_i + KT_e)}{B^2}, \tag{4.4.3}$$

where $\eta_{\perp}$ is the perpendicular plasma resistivity, and $n$ is the plasma density. The resistivity is proportional to $T^{-3/2}$, and so the fully ionized diffusion coefficient will decrease with increasing temperature:

$$D_{\perp FI} \sim \frac{1}{B^2 T^{1/2}}. \tag{4.4.4}$$

For a fully ionized plasma we would expect that if we increase $B_{min}/B_{ecr}$, which increases both $B$ and $T$, that the decay times would show a definite increase. However, as stated earlier, the data does not show this trend.

## 4.5 Experimental results: Comparison of diamagnetic signal to Faraday cup currents

Before an ion reaches the Faraday cup it must first be formed, it must then diffuse out of the plasma in a manner that is amenable to extraction. Once extracted, the ion transit times from the plasma to the Faraday cup are on the order of microseconds, and therefore negligible when compared to plasma time scales of interest. Hence, any delays in recorded ion current, as measured from leading edge of the trigger signal, will be due to both the time required to form a certain charge state, and the time required for that particular charge state to diffuse from the formation region to the extraction region. In this section we compare ion currents to the diamagnetic signal.

In Fig. 4.5.1 we compare the diamagnetic signal (unintegrated) to the ion currents for a helium plasma in the 6.4 GHz ECR. Also shown in Fig. 4.5.1 is the trigger signal and the source settings for reference. Approximately 1 ms after microwave power is turned on, both the diamagnetic signal and the current of $He^{1+}$ start to rise. The current of $He^{1+}$ then

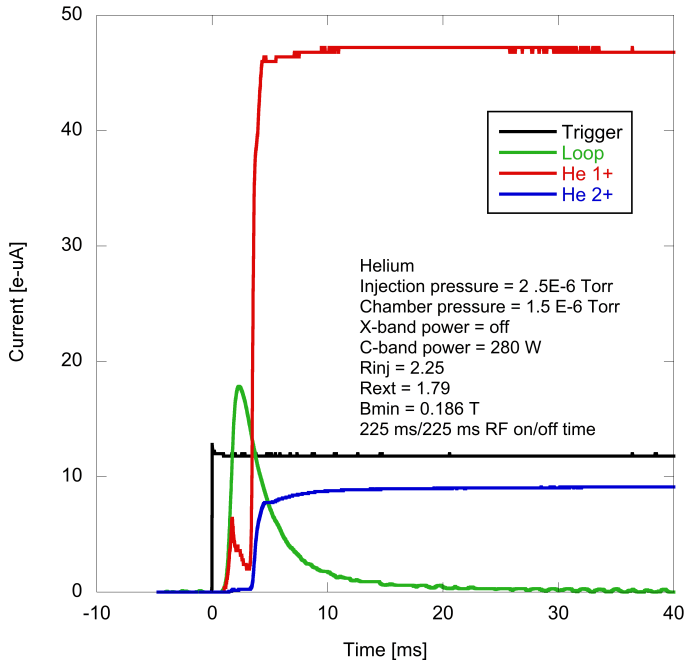


Figure 4.5.1: Faraday cup currents at beginning of microwave pulse. Helium plasma.

undergoes a slight decrease before rapidly rising to a steady state value of around 47 e-$\mu$A. At approximately 3.5 ms the current of $He^{2+}$ begins to appear, reaching steady state value of 9 e-$\mu$A some 10-15 ms after microwave power is applied. Not surprisingly, no currents appear before the diamagnetic signal does.

Decay of the ion currents and the diamagnetic signal when microwave power is turned off is shown in Fig. 4.5.2. The zoomed in view, on the right of Fig. 4.5.2, shows that both He $1^+$ and He $2^+$ have small peaks in the current form just as the microwave power is turned off. These are the so-called "afterglow" peaks[38] that are often seen with ECRIS operating in pulsed mode. However, there are no corresponding "wiggles" in the diamagnetic signal, which is seen to rapidly and smoothly rise, and then decay away slowly. If we fit exponential decay of the form: $y = m_1 + m_2\,(\exp(-m_3 x))$ to the falling portions of the ion currents, we can calculate that the He $2^+$ rate constant ($1/m_3$) is approximately 5 times larger than He $1^+$ rate constant (Fig. 4.5.3).

The unintegrated diamagnetic loop signal at both the leading and trailing edge of the microwave pulse, as shown in Fig's 4.5.1 and 4.5.2, has a characteristic form. There is first a rapid, exponential rise to some maximum value. This is immediately followed by more gradual exponential decay (for certain source settings, there are peaks overlayed on the exponential decay portion of the signal, as will be shown later). The e-fold time of the rising portion of the loop signal in Fig. 4.5.1 is approximately five times faster than for the falling portion of the signal. While at the trailing edge of the microwave pulse (Fig. 4.5.2), the e-fold time for the rising portion of the loop signal is several tens of times faster than the for the decaying part.

In Fig. 4.5.4 Faraday cup currents for charge states from Ar $5^+$ to Ar $10^+$ and the diamagnetic signal are shown. Again, the trigger signal and source settings are shown for reference.

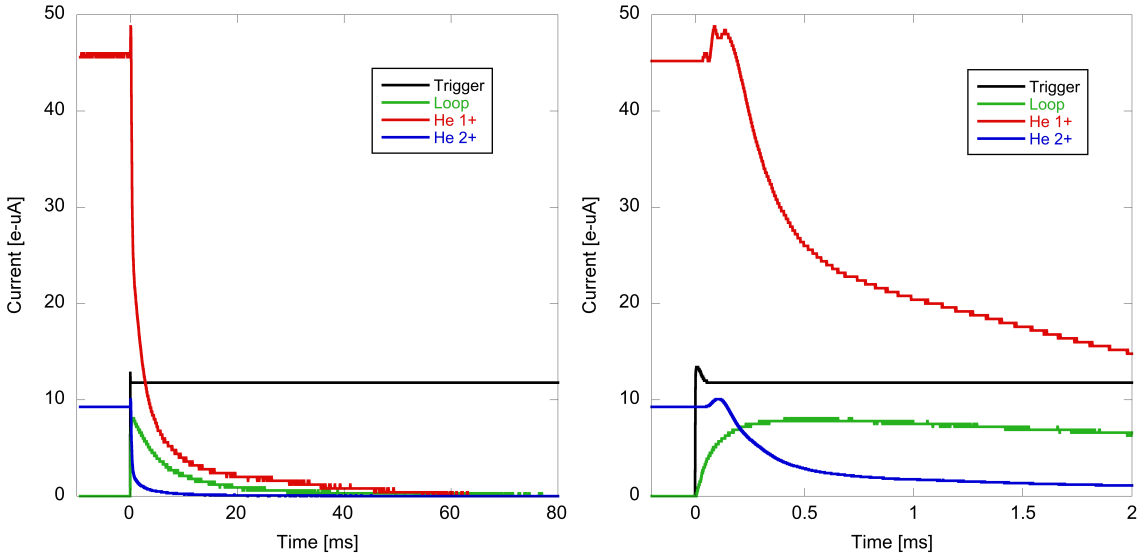


Figure 4.5.2: Faraday cup currents at end of microwave pulse. Helium plasma. Left: full view. Right: zoomed in view showing afterglow peak in greater detail.

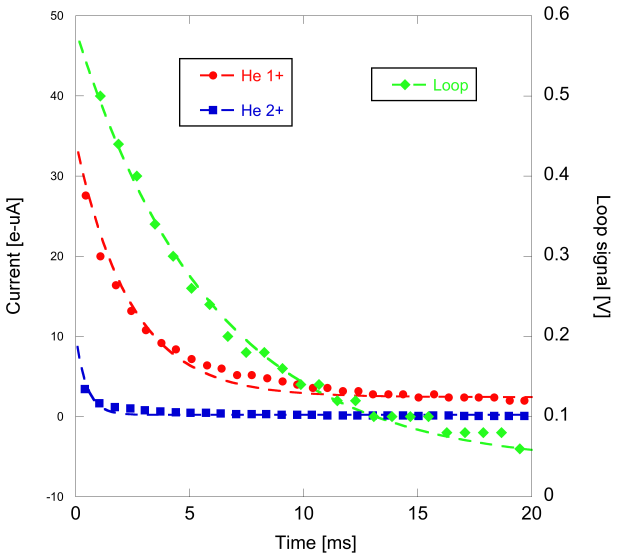


| y = m1 + m2*exp(-m3*x) | | |
|---|---|---|
| | Value | Error |
| m1 | 0.039039 | 0.0005959 |
| m2 | 0.543 | 0.0016465 |
| m3 | 0.16627 | 0.00098607 |
| Chisq | 0.047386 | NA |
| $R^2$ | 0.99556 | NA |

| y = m1 + m2*exp(-m3*x) | | |
|---|---|---|
| | Value | Error |
| m1 | 2.4403 | 0.058065 |
| m2 | 31.893 | 0.36701 |
| m3 | 0.41597 | 0.0072214 |
| Chisq | 1275.2 | NA |
| $R^2$ | 0.94875 | NA |

| y = m1 + m2*exp(-m3*x) | | |
|---|---|---|
| | Value | Error |
| m1 | 0.22761 | 0.010271 |
| m2 | 9.8345 | 0.20192 |
| m3 | 2.0825 | 0.054291 |
| Chisq | 55.161 | NA |
| $R^2$ | 0.88796 | NA |

Figure 4.5.3: Exponential fits to the falling portion of the Faraday cup currents and diamagnetic signal during plasma decay. Helium plasma.

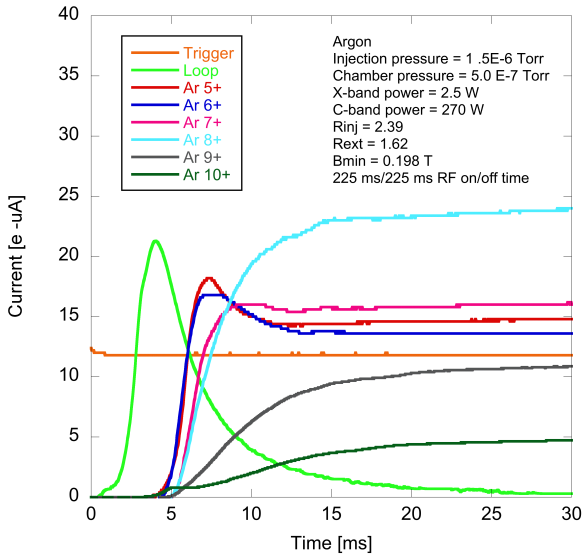


Figure 4.5.4: Faraday cup currents at beginning of the microwave pulse. Argon plasma.

Source parameters are set to maximize the current of Ar $9^+$ at the Faraday cup. Despite this, the charge state distribution is still peaked on Ar $8^+$, as indicated in Fig. 4.5.4, because Ar $8^+$ is a closed shell, and so the ionization potential jumps as one goes to Ar $9^+$. The first ion currents to reach the Faraday cup are Ar $5^+$ and Ar $6^+$, which both appear at approximately the same time, some 4 ms after the microwave power is turned on. The remaining charge states appear at approximately 5 ms. Higher charge states also take a longer time to reach steady state. For example, the e-fold time of Ar $8^+$ is approximately 3.5 ms, while Ar $9^+$ is 6.2 ms. These observations reinforce the notion that the dominant ionization process is a stepwise one[16], that is, high charge states are obtained through multiple collisions with electrons. Each ionization collision between an electron an ion raises the ion's charge state by one.

ECRIS operating in pulsed mode sometimes exhibit a phenomenon called preglow[25]. Preglow, similar to afterglow, is a transient peak in extracted ion current that occurs near the beginning of the microwave pulse for certain charge states. Both Ar $5^+$ and Ar $6^+$ have preglow peaks, while the higher charge states have little or no preglow peaks.

The decay of the measured Argon currents and diamagnetic signal is shown in Fig. 4.5.5. Afterglow peaks can be seen for almost all of the charge states. We can also see that the decay of currents is distinctly unsmooth. Immediately following the afterglow peak there is a steep and rapid drop in recorded current for approximately 0.5 ms. The diamagnetic signal during this portion is undergoing the rapid exponential rise discussed earlier. For the next 0.5 ms, the decay rate of the ion currents decreases, and at the same time the diamagnetic signal begins its slow decay. Then, at approximately 1.5 ms there is a sudden, large drop in the ion current signals (this is especially noticeable for Ar $8^+$). Concurrent to this, is a transient peak in the diamagnetic signal. At approximately 3 ms there is another sudden change in the ion current, and another spike in the diamagnetic loop signal.

Table 4.1 shows the calculated, based on the data shown in Fig. 4.5.5, decay e-fold times

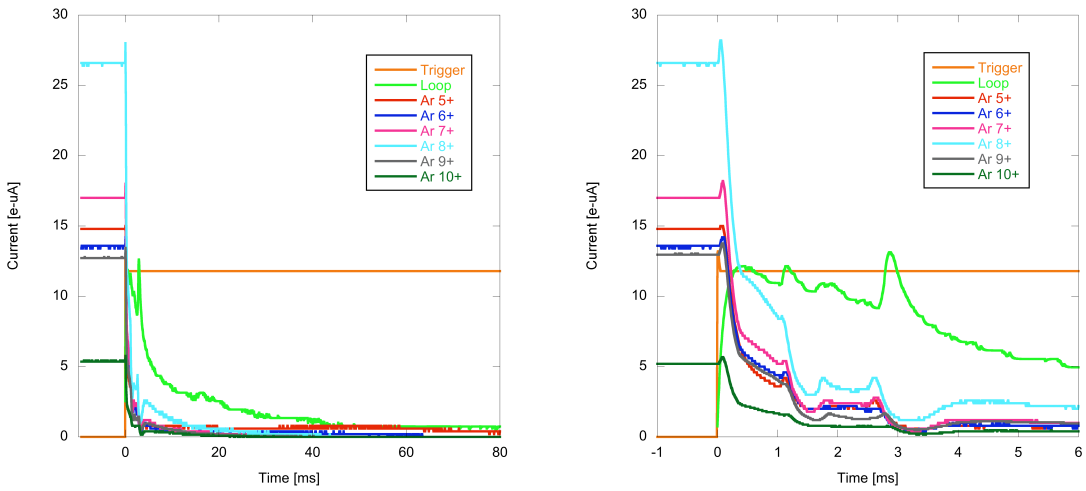


Figure 4.5.5: Faraday cup currents at end of the microwave pulse. Argon plasma. Left: full view. Right: zoomed in view.

| Argon charge state | $\tau$[ms] ($R^2$) |
|---|---|
| $5^+$ | 0.186 (0.99) |
| $6^+$ | 0.151 (0.99) |
| $7^+$ | 0.139 (0.98) |
| $8^+$ | 0.149 (0.97) |
| $9^+$ | 0.142 (0.98) |
| $10^+$ | 0.139 (0.98) |

Table 4.1: Calculated decay e-fold times ($\tau$) for different argon charge states. Times calculated based on data shown in Fig. 4.5.5.

for the measured argon ion currents. The decay e-fold times are calculated by fitting a curve of the form: $y = m_1 + m_2(\exp(-m_3 x))$, to a portion of the current signal immediately following the small afterglow peak. The table shows that, as with a Helium plasma, the time required for the ion currents to decay generally decreases as the charge state increases. A similar trend was seen in an earlier study by Tarvainen *et al.*[49].

The unintegrated diamagnetic signal is proportional to the rate of change of the diamagnetic current. The strength of the diamagnetic current is related to the energy density, *nkT*, of the charged particles in the plasma. Hence, rapid changes in the diamagnetic signal correspond either to rapid changes in plasma density or average energy of the confined particles. The peaks in the diamagnetic signal in Fig. 4.5.5 at 1.5 ms and 3 ms are associated with decreases in ion current. If we assume the peaks are caused by a sudden loss in particle density, then the data imply that the charged particles are lost radially, across magnetic field lines rather than axially, along magnetic field lines. If the particles are lost axially then we should see an increase in the Faraday cup currents, which, clearly we do not.

Supporting evidence for a radial loss mechanism is given by Tarvainen *et al.*[49]. In that experiment time resolved measurements of high energy x-rays (> 30 keV) showed periodic bursts in the count rate of photons superimposed on an exponentially decaying portion, analogous to the decay of the diamagnetic signal in Fig. 4.5.5. The x-rays were measured with a germanium detector, in a radial position, with aligned such that it focused on a magnetic pole. The shielding and collimation were such that both thin and thick target bremsstrahlung could be detected. Because of its positioning and alignment, the periodic bursts of x-rays seen by the detector were most likely caused by electrons, expelled from the plasma across magnetic field lines, striking a magnetic pole.

## 4.6 Experimental results: Effect of initial density of electrons on diamagnetic signal

In order to understand the effect of the initial density of electrons on plasma breakdown time we undertook a small study utilizing the first stage of the 6.4 GHz ECR. As mentioned in Chapter 1, the 6.4 GHz ECR includes a small injection stage. The plasma created in this stage diffuses into the main stage, and thus helps to initiate and maintain the primary plasma. Turning off the first stage deprives the primary stage of a constant source of new, low energy electrons, and thus, any electrons present at the initiation of a new microwave pulse are left over from the previous pulse.

Figure 4.6.1 shows the results of this study. Ion source settings are kept constant, and are shown in the plots. We vary the pulse duration and whether or not the first stage is on. In Fig. 4.6.1 are plots of diamagnetic loop signal versus time. The blue curves represent a data point with the first stage on, while the red curves represent a data point with the first stage off. The plot on the left is for microwave pulse times of 600 ms (50% duty factor). We can see that there is a negligible difference in appearance of the diamagnetic signal. The plasma ignition time, both with and without the first stage on, is less than 5 ms. There is a slight difference in

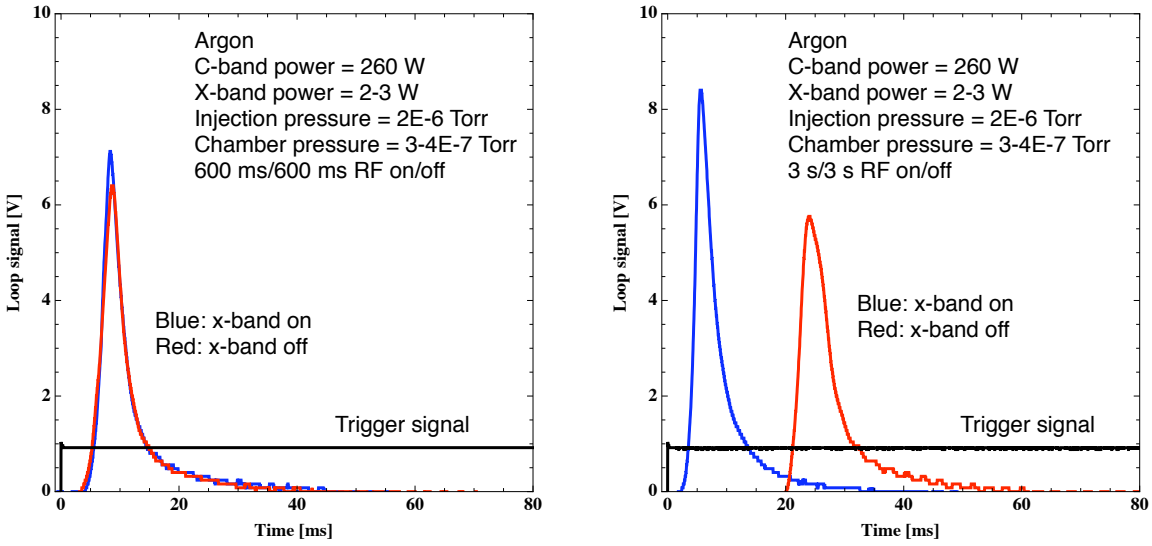


Figure 4.6.1: Effect of the first stage of the 6.4 GHz ECR on the diamagnetic signal at leading edge of microwave pulse.

the integrated diamagnetic signal (a difference of approximately 4% at 50 ms).

The plot on the right of Fig. 4.6.1 shows the loop signals for microwave pulse times of 3 s (again, 50% duty factor). In this case there is a clear difference in the diamagnetic signals. With the first stage on the plasma ignition time is again less than approximately 5 ms. When the first stage is turned off, the diamagnetic signal does not appear until approximately 20 ms. The integrated signal, with the first stage on, is 8% larger at 50 ms. We conclude from this that even 600 ms beyond the end of the microwave pulse, a significant number density of electrons remains in the chamber, thus enabling the rapid ignition of the plasma on the next pulse.

A simple model proposed by Tarvainen *et al.*[50] is helpful in explaining these observed trends. Under the assumption that the neutral density does not change significantly at the start of the breakdown process, the model predicts a breakdown time of:

$$t_{breakdown} = \frac{\ln\left(n_{e,critical}/n_{e,0}\right)}{n_n \left\langle \sigma_{ion} v \right\rangle}, \tag{4.6.1}$$

where $n_{e,critical}$ is the electron density at which measurable bias disk currents appear, $n_{e,0}$ is the initial electron density, $n_n$ is the neutral density, and $\langle \sigma_{ion} v \rangle$ is the ionization rate coefficient averaged over the electron velocity distribution. Equation 4.6.1 predicts that the breakdown time will decrease if the neutral density is increased, and also predicts that a larger initial electron density will cause breakdown to occur earlier (although the impact of initial electron density on breakdown times is not as large as the impact of neutral density, due to the fact that it appears inside of a logarithm).

With the first stage of the 6.4 GHz ECR turned on, there is a minor difference in the time of appearance of the diamagnetic signal, regardless of the microwave on and off times. Figure 4.6.2 emphasizes this point. Six different microwave on and off times are shown. In all cases,

the diamagnetic signal becomes measurable (which we equate to ignition of plasma) almost immediately after the leading edge of the microwave pulse. The apparent lack of change in ignition time when the first stage is on suggests that the initial density of electrons, $n_{e,0}$ (Eq. 4.6.1), is kept at a sufficient level to be close to $n_{e,critical}$, and hence, the breakdown down time becomes approximately independent of microwave pulse pattern. A similar observation was made in another study in which a continuous, low power travelling wave tube amplifier (TWTA) signal was used to keep the density of electrons elevated during periods when the klystron was off[48]. With the TWTA on, plasma ignition times, as deduced from Faraday cup signals, were seen to vary little with klystron repetition rate.

We note, that although the breakdown time seems to be independent of pulse pattern when the first stage of the 6.4 GHz ECR is on, the integrated diamagnetic signal does depend on pulse pattern (Fig. 4.6.3). As the on and off times are shortened we can see that the steady state value of the integrated diamagnetic signal decreases. For on/off times as low as 50 ms, there is almost no change in integrated signal, as compared to on/off times of 600 ms. For on/off times below 20 ms, however, the integrated signal is reduced by as much as 60%. This implies that for the source settings provided in Fig. 4.6.3 the plasma energy density (which is proportional to the integrated loop signal) requires greater than 20 ms to reach its full value.

Further evidence of the importance that the number density of electrons in the plasma chamber at the leading edge of a microwave pulse plays in determining the plasma breakdown times is shown in Fig. 4.6.4. Shown are plots of the ratio of reflected to forward microwave power as a function of time for two different microwave on/off times. Forward and reflected powers are measured at a directional coupler located next to the ion source. The data was taken on the 6.4 GHz ECR, with the first stage turned off. One of the parameters that affects the amount of power that is absorbed or reflected is electron density[52]. Hence, by observing when there is a significant change in the ratio of reflected to forward power we can estimate the plasma formation time. Again, we see that a longer microwave off period (more time for the electrons to diffuse out of the plasma), results in a delay to ignition time of the plasma.

## 4.7 Experimental results: Comparison of diamagnetic loop signal and ratio of reflected to forward microwave power

The diamagnetic signal is proportional to the rate of change of the diamagnetic current, and is thus related to the rate of change of plasma pressure (energy density). The greater the magnitude of the signal, the greater the rate of change of the plasma energy density. Integration of the diamagnetic signal from time zero to time $\tau$ will allow one to estimate the plasma energy density at time $\tau$ by using Eq. 2.1.42.

In an anisotropic plasma with two temperatures, $T_{\perp}$ and $T_{\parallel}$, the energy density is simply:

$$nkT_{Total} = nkT_{\perp} + nkT_{\parallel}. \tag{4.7.1}$$

In ECR heated plasmas $T_{\perp}$ is typically much greater than $T_{\parallel}$, and the parallel component of energy density can be omitted from Eq. 4.7.1. Hence, if either the density, $n$, or the temperature,

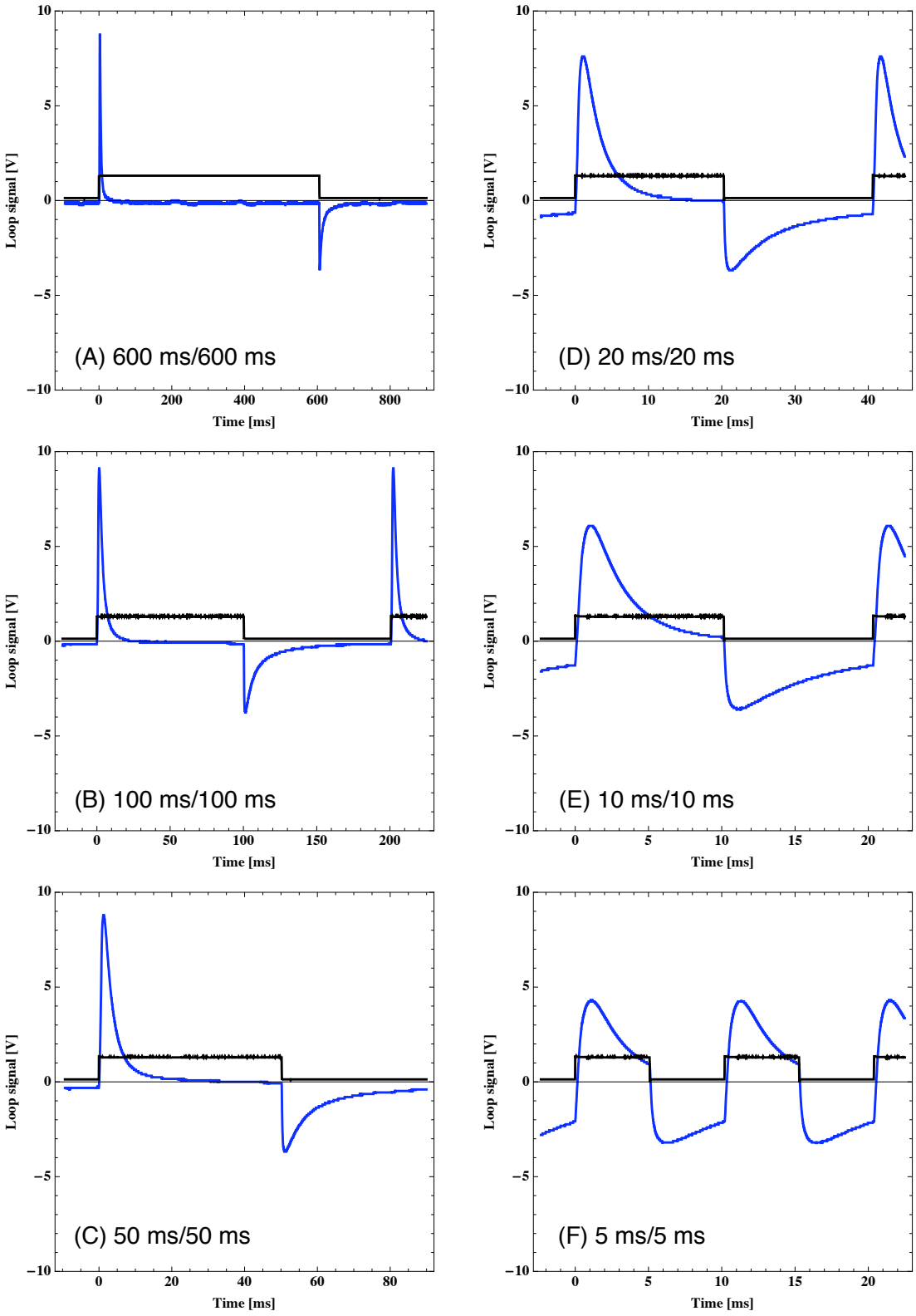


Figure 4.6.2: Effect of microwave on and off times on diamagnetic signal. 6.4 GHz ECR. First stage is on.

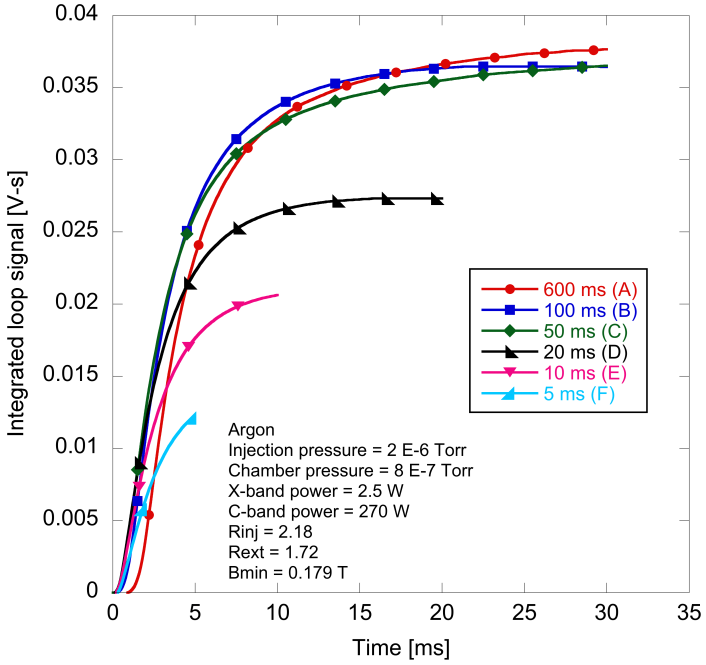


Figure 4.6.3: Integrated diamagnetic loop signal for different microwave on and off times shown in Fig.4.6.2.

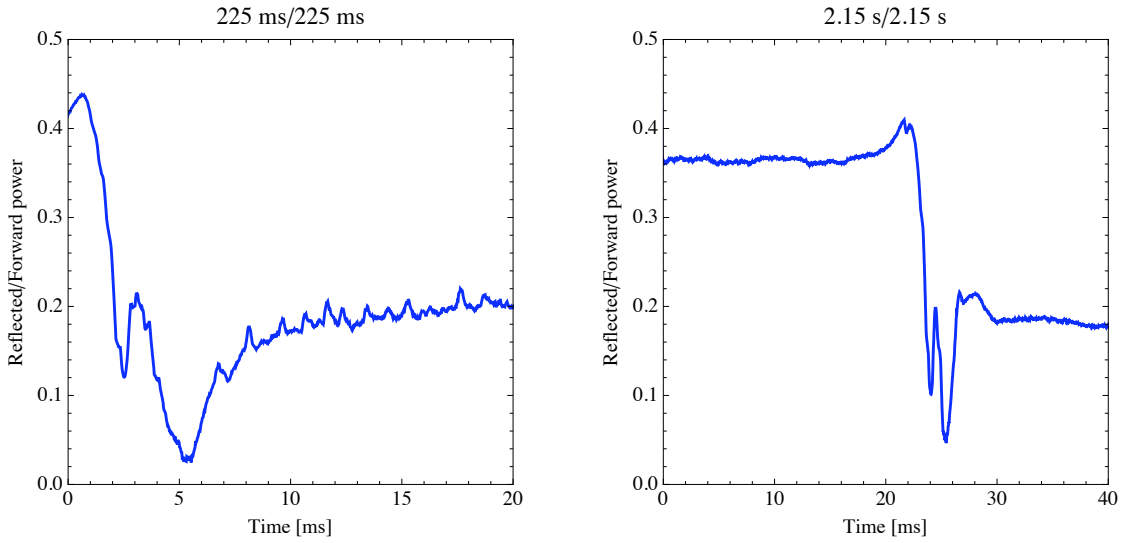


Figure 4.6.4: Ratio of reflected to forward power versus time on 6.4 GHz ECR. First stage is turned off. Left: 225 ms/225 ms on/off pulse pattern. Right: 2.15 s/2.15 s on/off pulse pattern.

$T_\perp$, is changing we should theoretically be able to see a diamagnetic signal. We will discuss anisotropy in the x-ray production in Chapter 5, were we will show that radial x-ray intensity is typically much larger than axial x-ray intensity.

All charged particles, both ions and electrons, that are confined within the plasma contribute to the energy density. Typically ion temperatures are much, much less than electron temperatures in ECRIS, with values of a few electronvolts[16], and their contribution to the energy density can be ignored. The electron population consists of a large population of warm electrons, and a smaller population of hot electrons[17]. The majority of the energy content in the plasma comes from these electrons. Hence, the diamagnetic signal can be thought of as an indicator of the presence and growth of the warm and hot electron populations.

With no plasma in the chamber, the amount of reflected microwave power is a function of the coupling between the waveguide and the plasma chamber. For a given power and frequency, the ratio of reflected to forward power, with no plasma present, is essentially constant, as shown in the plot on the right of Fig. 4.6.4 (we of course assume that the geometry of the plasma chamber is not being changed). As the plasma forms it will absorb some of the incoming microwave power, and we should therefore observe a drop in reflected power. Models have shown that the amount of microwave power that is absorbed, and where the power is absorbed is primarily a function of plasma density and plasma collisionality[52, 32]. Hence, changes in the ratio of reflected to forward power can be associated with changes in plasma density.

Shown in Fig. 4.7.1 is a plot of the loop signal, the integrated loop signal, and the ratio of reflected to forward microwave power. The ion source settings are shown in the figure. We see that the 6.4 GHz microwave power and the magnetic field configuration are different for the loop related quantities and the reflected to forward power ratio. However, as shown previously, neither the microwave power or magnetic field configuration change the plasma ignition time in a significant manner. The neutral pressure, which has been shown to change the ignition time, is identical.

We can see that almost immediately after the leading edge of the microwave pulse, which occurs at time *t=0*, $P_{ref}/P_{for}$ begins to change. At approximately 0.5 ms we can begin to see the diamagnetic signal, indicating the growth of the warm and hot electron populations. At approximately 3 ms $P_{ref}/P_{for}$ stops changing in a significant manner. Based on the above arguments, this implies that the plasma density has reached an approximate steady state value. The diamagnetic loop signal also undergoes a dramatic change at 3 ms. Namely, it has reached its maximum rate of change, and begins to slow down. Recall that the diamagnetic signal is primarily proportional to changes in the product of warm and hot electron density and electron energy. If either change, a diamagnetic signal should appear. If we assume, based on $P_{ref}/P_{for}$, that plasma density does not change after 3 ms, the plot suggests the following. During the first 3ms, there is a rapid increase in *both* plasma density and electron energy. This causes the exponential increase in diamagnetic loop signal. After 3 ms, the plasma density stops changing, and the microwave power is serving to slowly increase only the average energy of the electrons. Hence, the diamagnetic signal is slowly decreasing.

Complementary data to that shown in Fig. 4.7.1 is given in Fig. 4.7.2. The data in Fig. 4.7.2 is part of an extensive set of measurements taken at the Accelerator Laboratory in the

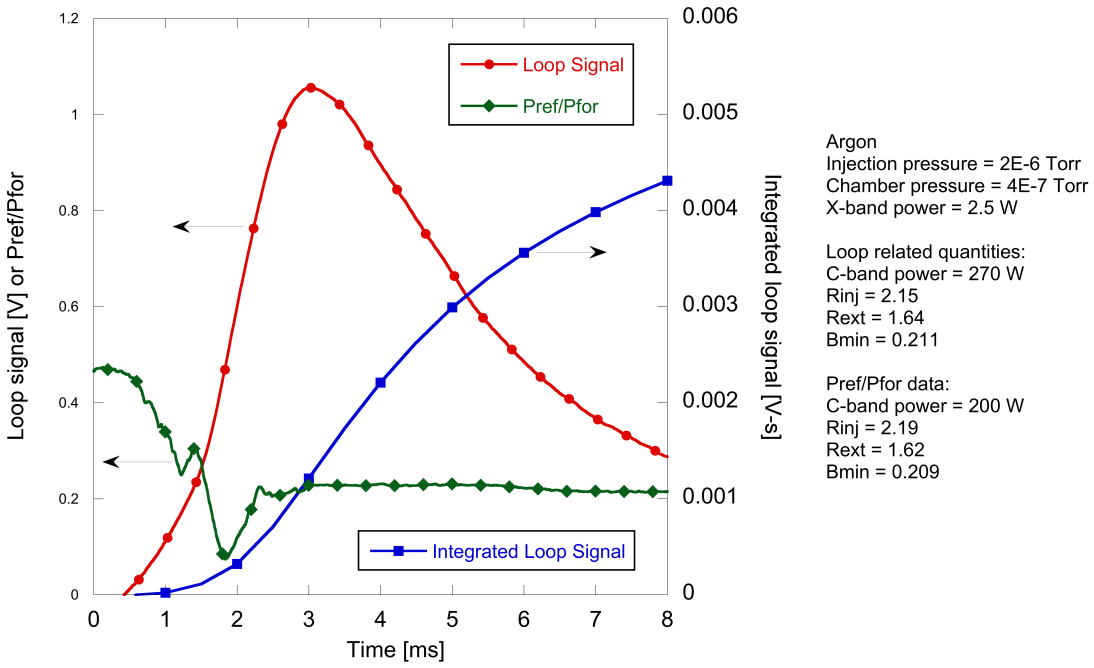


Figure 4.7.1: Comparison of diamagnetic loop signal to ratio of reflected to forward power on 6.4 GHz ECR. Leading edge of microwave pulse.

Department of Physics (JYFL), University of Jyvaskyla. The study focused on making time resolved measurements of low energy x-rays produced by the JYFL 14 GHz ECRIS[31]. Prior time resolved x-ray measurements used a germanium detector, and concentrated on high energy x-rays (> 30 keV)[42, 44, 43]. The use of the Amptek XR-100T-CdTe in this study allowed detection of x-rays with energies as low as 1 keV. The time resolved x-ray data acquisition was developed by T. Ropponen[42]. The other data acquisition systems were developed and implemented by physicists at JYFL. I was responsible for the design of the x-ray collimation system and was present at JYFL during the study.

To record the data shown in Fig. 4.7.2, the 14 GHz microwave pulse pattern was set to 500 ms on, and 500 ms off. In addition, there is a continuous 10 W of 11.53 GHz power from a TWTA. As mentioned earlier this helps to keep the population of electrons relatively high during 14 GHz off periods. Data was taken over a 24 hour period with an Argon plasma.

Figure 4.7.2 shows the average detected photon energy and the ratio of reflected to forward microwave power as a function of time. $P_{ref}/P_{for}$ exhibits the same behavior as in Fig. 4.7.1, dropping quickly as the plasma ignites and reaching a steady state some tens of milliseconds later. The values of $P_{ref}/P_{for}$ shown in the Fig. 4.7.2 are about one order of magnitude less than those shown in Fig. 4.7.1, indicating a much better coupling scheme.

The most interesting feature of this plot is the behavior of the average energy of detected photons. It can be seen that it first rapidly rises, decreases to a minimum, and then slowly increases to some steady state value. This general behavior was observed in all data points (three different microwave powers, three different neutral pressures, and three different magnetic field settings). The average energy of the electrons in the plasma is not being measured

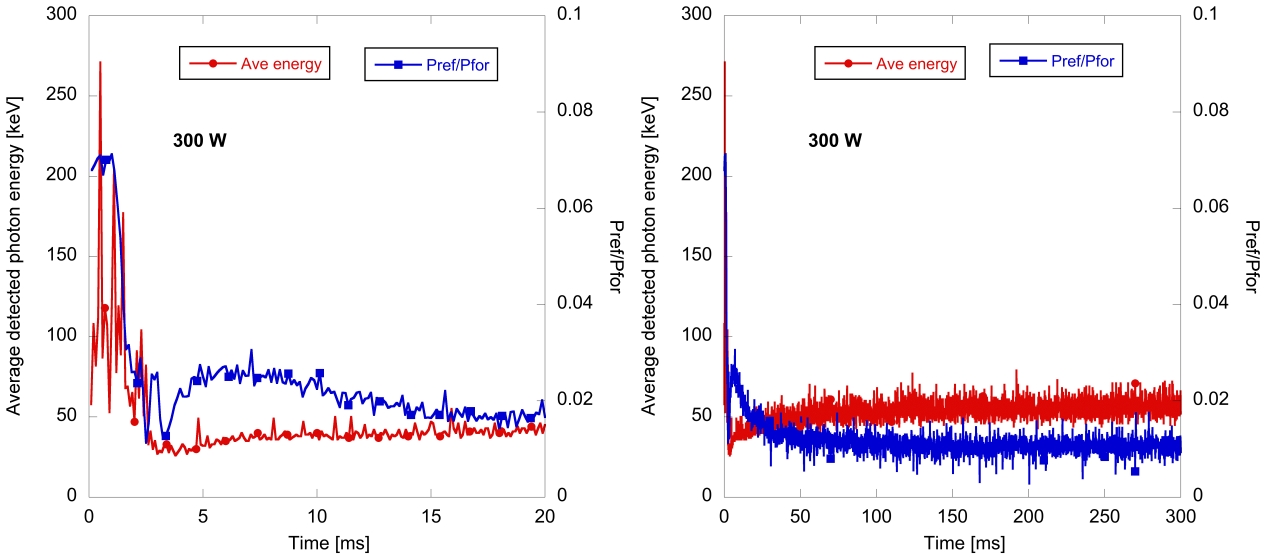


Figure 4.7.2: Average detected photon energy, and ratio of reflected to forward microwave power as a function of time. 300 W of microwave power. Argon plasma. Data taken on JYFL 14 GHz ECRIS. Left: zoomed in time axis. Right: extended time axis.

directly. However we know that a 30 keV photon can only be produced by an electron with an energy of at least 30 keV (see Eq. 2.3.2 in Chapter 2), and thus we can use the x-ray data to qualitatively assess the behavior of the electrons. We conclude, then, that at the very beginning of the discharge, the average electron energy is relatively high. This is followed by a collapse of the average electron energy to some lower, steady state value. During the period of rapid average electron energy change, the plasma density also experiences a rapid change, substantiating what we proposed earlier: the rising portion of the diamagnetic signal is due to a combination of both the plasma density and electron energy changing, while the falling portion is due to a slow change in electron energy.

## 4.8 Conclusions

In this chapter we have discussed the use of a diamagnetic loop as a means of exploring various plasma time scales on a relative basis. Specifically, we focused much of our attention on studying how changing ion source parameters, such as microwave power and neutral pressure, would effect the rise and decay of the integrated diamagnetic signal (which can be related to plasma energy density, see Eq. 2.1.42). We have shown that increasing microwave power lowers the e-fold times at both the leading edge and the trailing edge of the microwave pulse. The fact that decay times increase with microwave power, makes sense based on the electron-ion collisional frequency, $\nu_{ei}$. Microwave power, however, has almost no impact on the ignition times of the plasma.

The e-fold times were shown to be insensitive to both neutral pressure and magnetic field setting. Neutral pressure, however, can have a dramatic effect on the ignition time of the

plasma. In addition to neutral pressure, ignition times are also a function of pulse spacing and whether or not the first stage of the 6.4 GHz ECR is on. We suggest that the insensitivity of decay times to magnetic field setting is due to the fact that the perpendicular diffusion coefficient (Eq. 4.4.1), which is proportional to the ratio of electron energy to magnetic field strength, remains essentially constant as the magnetic field strength is increased. In all cases, the rise time of the integrated diamagnetic signal was seen to be faster than the decay time.

Typically, except for He $1^+$, the ion currents did not appear in measurable amounts until a few milliseconds after the diamagnetic signal. Had we measured the very low charge states of Argon ($1^+$, $2^+$, etc.) it is probable that they would have appeared much sooner in relation to the diamagnetic signal. It was also shown that higher charge states generally appeared later, however, they also decayed away at faster rates. We suggested that peaks superimposed on the decaying portion of the diamagnetic signal at the trailing edge of the microwave pulse were caused by a radial expulsion of charged particles.

By comparing the diamagnetic signal to the ratio of reflected to forward power we theorized that the initial, exponential rise in the diamagnetic signal at the leading edge of the microwave pulse is due to rapid changes in both the average electron energy and density. During the slowly decaying portion of the loop signal, the hot tail of the electron population is increasing. This theory is supported by time resolved, low energy x-ray measurements that showed that the period of rapid change of $P_{ref}/P_{for}$ coincides with a rapid change in average photon energy. Finally, we want to emphasize that the data shown in this chapter should be used for qualitative analysis only.

# Chapter 5

# Axial and radial x-ray studies in ECRIS

In this chapter, results of x-ray measurements taken on the LBNL 6.4 GHz ECR and the 14.3 GHz AECR-U are described. The x-ray flux was measured simultaneously in both the direction parallel ("axial") to the source axis and the direction perpendicular ("radial") to the source axis using standard NaI(Tl) detectors. The position and associated collimation of each detector are such that the resonance zone was visible. The setup is shown in Fig. 5.1.1.

Most reported x-ray measurements have been taken in only one direction with respect to the ECR ion source axis, either radially, or axially. However, the combination of the ECR heating mechanism, strong magnetic fields, and anisotropic nature of the emission of radiation in a collision, are expected to cause the radiation emitted by an ECR ion source plasma to be anisotropic. Thus, measuring the angular dependence of x-rays is desirable. Two studies in which such a measurement was performed were those done by Bernhardi[7] and Kato[29].

Bernhardi took measurements in both the radial and axial directions, but the device used in the study was a magnetic mirror with no multipole structure. The resonance zone was visible in both directions. By using a combination of detector types the range of photon energies examined was between 10 keV and 1.1 MeV. From the measurements they were able to estimate a degree of anisotropy (related to the size of the mirror loss cone) of the electron distribution function above 200 keV. They found that the anisotropy angle, $\theta_0$, was between 50 and 60 degrees ($\theta_0 = 0$ represents an isotropic distribution function, and $\theta_0 = 90$ represents complete anisotropy).

In comparison, Kato measured low energy x-rays (< 20 keV), using a Si-pin diode detector, produced in a minimum B device operating at 2.45 GHz. X-rays were recorded in both the radial and axial direction, however the radial detector was positioned such that it could not directly see the resonance zone. As a result, axial x-ray count rates were larger than radial x-ray count rates.

Additionally, Friedlein *et al.*[13] have also estimated the anisotropy of the electron energy distribution function in a 7.5 GHz ECRIS through the use of an "anisotropy ratio." This ratio corresponds to the change in the x-ray spectrum due the distribution of electrons in the angle $\theta$, where $\theta$ is the angle between the momentum vector of an electron an the axis of symmetry. Friedlein showed that as the strength of the magnetic field was increased, the anisotropy ratio decreased, corresponding to a more anisotropic distribution function.

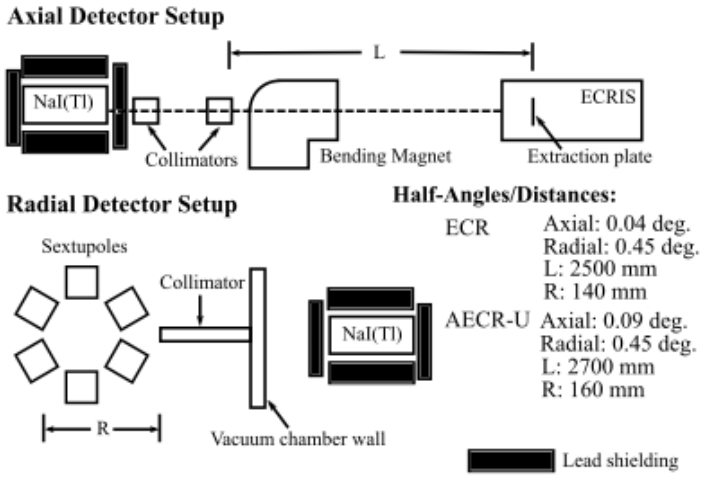


Figure 5.1.1: Axial and radial x-ray detector setup used in this study.

Our purpose is to examine the changes in x-ray power and spectral temperatures in the axial and radial direction as a function of microwave power and magnetic field setting. The goal is not to calculate a degree of anisotropy in the electron energy distribution function, but rather to qualitatively compare the intensity of x-rays in the axial and radial directions. We also make a qualitative comparison between axial and radial x-ray count rates at two operating frequencies: the 6.4 GHz ECR and the 14.3 GHz AECR-U.

## 5.1 Experimental setup and methods

Data presented in this chapter was taken on the LBNL 6.4 GHz ECR and on the LBNL 14.3 GHz AECR-U, both described in an earlier chapter. For measurements on both the ECR and AECR-U, two NaI(Tl) are used to detect photons created in electron-ion collisions within the plasma. The theory and operation of NaI(Tl) detectors are explained in detail in many textbooks on radiation detection[30], and a brief description of these detectors is given in Appendix B. The particular detectors used in this study enable reliable detection of photons with energies ranging from approximately 30 keV to over 1 MeV, with the minimum energy determined primarily by the amount of material between the NaI(Tl) crystal and the plasma, and the maximum energy determined by the size of the NaI(Tl) crystal. One detector, positioned perpendicular to the machine axis, measures photons emitted in the radial direction. The other, positioned parallel to the machine axis, measures photons emitted axially. A schematic showing the position of both detectors relative to the ECR ion source is depicted in Fig. 5.1.1 (the exact detector position and shielding are slightly different for measurements made on the ECR and AECR-U). Also shown in Fig. 5.1.1 are the geometric acceptance half-angles for the various collimation setups.

The collimation and shielding are designed such that the majority of x-ray photons that are visible to the detectors were created in the plasma itself, and not in collisions between

unconfined electrons and plasma chamber structure. The one exception to this is the collimation for the axially placed detector for the AECR-U. In this case, due to time constraints, the detector can see a circle of roughly 10 mm at the extraction electrode (the extraction aperture is 8 mm in diameter). X-rays created by electrons lost from the plasma which subsequently strike the electrode can thus be detected from the AECR-U.

In the case of the ECR, we use a collimation system that consists of two copper blocks and one heavy metal (95 % W and 5 % Cu) block. Copper is not as dense at lead, but it does have the advantage of having no absorption edges in the range of energies we are interested in. This should decrease the possibility of characteristics x-rays produced by photoelectric absorption of photons from entering the detector. The setup of the collimation system is shown in Fig. 5.1.1. The first copper block is located inside of the bending magnet vacuum chamber 2.75 m from the extraction plate aperture. It is 100 mm long and has a square, 10 mm groove machined along its length. A 100 mm block of copper will practically stop all x-rays with energies less than 1.0 MeV. The purpose of this block is to lower the number of x-rays that can enter the remaining two blocks at large angles with respect to the collimation axis, and thus reduce the number of scattered x-rays that reach the detector. The heavy metal block, located 3.5 cm behind the first collimator, is 127 mm long and has a 1 mm square groove machined into it. The second copper block, located 2.75 m behind the tungsten-copper block, is 100 mm long and has a 3 mm square groove machined into it. The individual grooves are aligned with the center line of the ECR using a scope. The geometric acceptance angle of this collimator system is approximately 0.04 deg. This corresponds to a square with sides 5.12 mm at the extraction plate, small enough to fit completely inside of the 8 mm diameter extraction aperture of the ECR. By ensuring that the detector does not see any solid walls, we minimize the chances of detecting x-rays produced by thick-target interactions. The same collimators are used in measurements made on the AECR-U, although the placements were slightly different.

The radial collimator for both the ECR and AECR-U is a copper piece that is 254 mm long and has a 2 mm square groove machined into it. It sits within the vacuum chamber of the source. The length and groove size of the collimator were chosen such that none of the sextupole structure falls within its geometric line of sight. The collimator is positioned such that a line that is co-linear with its central axis will pass approximately through the center of the plasma.

The individual signal from each detector is sent to an identical pulse shaper/amplifier. This signal is in turn processed with a dual multichannel analyzer (MCA), and then finally displayed and stored on a personal computer. The MCA accepts signals from two different detectors simultaneously.

We note that the physical sizes of the axial and radial detector NaI(Tl) crystals are different. Moreover, the photomultiplier tubes (PMT) and PMT base are not identical. Hence, the recorded spectra from an identical source of radiation would be different. Because of this, the response of each detector was studied by taking two spectra, in the radial direction, at an identical AECR-U operating condition. The resulting spectra are shown in Fig. 5.1.2.

For this calibration measurement, the shielding and collimation of the detector as well as its distance from the AECR-U was the same. As is shown in Fig. 5.1.2, the resulting spectral

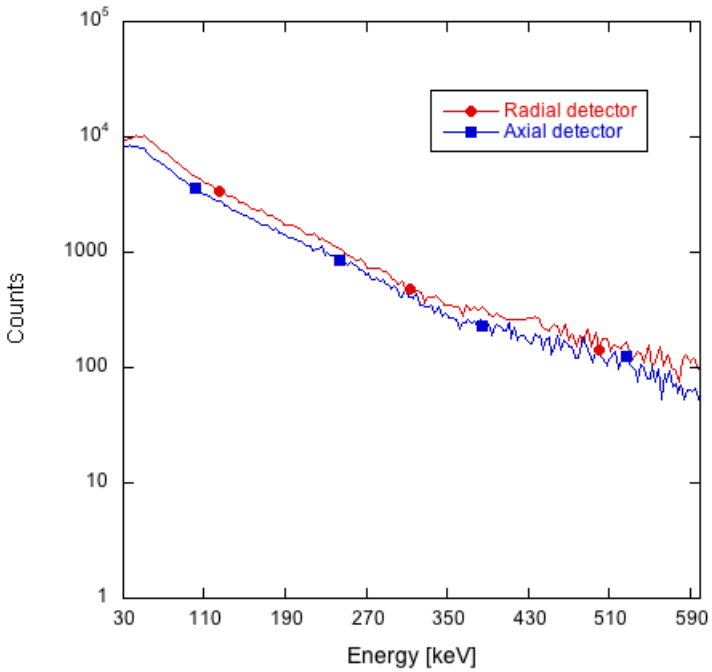


Figure 5.1.2: Spectra for the two NaI(Tl) detectors used in this study. Taken under identical source conditions, and identical collimation and shielding. Both the axial and radial detectors were placed behind the radial comllimator to produce these spectra

shape was very similar for both detectors, with one spectra offset by approximately 30% in an energy range of 30 keV to 600 keV. The lowest order correction to make, then, would be to take the ratio of the measured intensities at a given energy, and use this ratio to adjust the spectra on plots comparing radial and axial x-rays. This correction is made for data discussed in Section 5.2. Ideally, of course, one would use two identical detectors in the measurement.

Because the solid angles defined by the collimation in the radial and axial directions are different, we need to make an additional correction in order to compare the intensity of radial and axial x-rays on a somewhat equal basis. Instead of making a simple $1/r^2$ (which is based on the assumption that the x-rays are emitted isotropically) correction, we have chosen to correct the x-ray spectra by using an estimate of the plasma volume seen by each of the detectors. The total plasma volume can be approximated as the volume of an ellipsoid with major axis, $a$, and minor axis, $b$, defined by the axial and radial resonance zone positions (Fig. 5.1.3). The detector does not see the entire resonance zone volume due to the collimation and shielding, however. Because the grooves used in the collimators have square profiles, the visible plasma volume is calculated as the volume of a square pyramidal frustum:

$$V = \frac{h}{3}\left(m^2 + n^2 + mn\right), \tag{5.1.1}$$

where $h$ is the height of the frustum, and $m$ and $n$ are the lengths of the sides of the base and top of the frustum, as shown in Fig. 5.1.4. The surface of the resonance ellipsoid is curved;

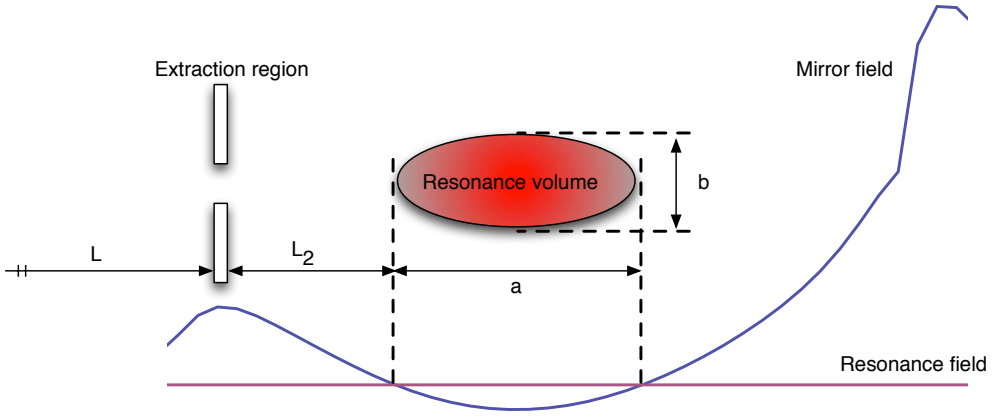


Figure 5.1.3: Diagram showing relative positions of extraction plane, mirror field, and resonance volume.

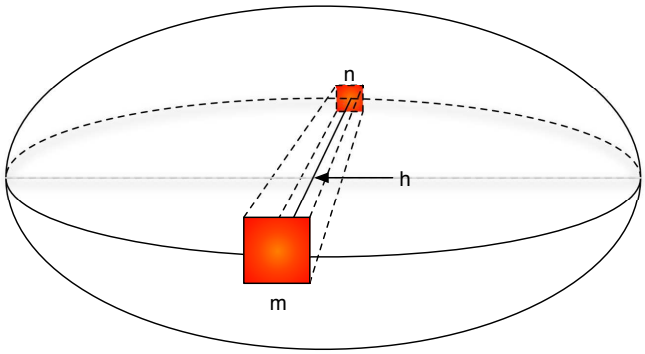


Figure 5.1.4: Diagram showing resonance ellipse and the volume of plasma visible to the detector, which is estimated using a pyramidal frustum.

however, we assume that it is flat over the small areas where the frustum intersects with it. The lengths of the sides of the base and top ($m$ and $n$ in Eq. 5.1.1 and Fig. 5.1.4) of the frustum are calculated based on the half angle defined by the collimation, and the distance from the collimator to the resonance zone. For example, the distance from an axial collimator to the resonance surface is $L + L_2$ (Fig. 5.1.3), where $L$ is given in Fig. 5.1.1, and $L_2$ is calculated using magnetic field models of the ion sources. The height of the frustum is either the major axis, $a$, or the minor axis, $b$, of the ellipsoid, depending on whether we are estimating the visible plasma volume for the axial or radial detector. Effects such as resonance zone broadening[46] due to Doppler shift have been ignored when calculating the positions of the resonance zone. We note that this correction will not affect the spectral temperature, as it will simply shift an entire spectrum either up or down. In addition, by using this simple correction, we assume that volume-averaged density profile and temperature profile are similar in the radial and axial direction.

## 5.2 Experimental results: effect of microwave power

### 5.2.1 6.4 GHz ECR

X-ray spectra, recorded radially and axially, taken with the 6.4 GHz ECR, running at three different microwave powers and with an Argon/Oxygen plasma, is shown in Fig. 5.2.1. For the specific source settings shown in Fig. 5.2.1, we can calculate (using the method outlined in the above section) that the ratio of axial to radial visible plasma volume is approximately five (indicating that the axial detector can see five times as much plasma). Hence, the radial x-ray spectra are scaled up by a factor of five (we could also, of course, scale the axial spectra down by five). Spectra have been corrected for absorption by quartz and air, but not for the aluminum casing protecting the NaI(Tl) crystal. Fig. 5.2.1 indicates that the maximum recorded x-ray energy in the radial direction, slightly more than 150 keV for all of the microwave powers, is greater than in the axial direction, around 100 keV. We also see that, despite the fact that the axial detector sees a larger volume of plasma, the count rate in the radial direction is approximately two orders of magnitude greater than in the axial direction.

In Fig. 5.2.2 the radial and axial x-ray power, based on the date in Fig. 5.2.1, as a function of microwave power is shown. The x-ray power is calculated in the range 30-150 keV for the radial direction, and in the range 30-100 keV for the axial direction. We see that the x-ray power behaves logarithmically with microwave power in the radial direction, and linearly with microwave power in the axial direction. The logarithmic behavior was also seen in radial measurements of low energy x-rays (see Chap. 3). The ratio of radial to axial x-ray power decreases with microwave power. In a previous study, Leitner et al.[34] found that the high energy x-ray flux increased essentially linearly with power. The ion source used in that study, however, is fully superconducting and operated at microwave frequencies of 18 GHz and 28 GHz. Based on Eq. 3.4.3, which shows that the pitch-angle scattering diffusion coefficient depends inversely on operating frequency, the fact that we see saturation in the x-ray power on the 6.4 GHz ECRIS, but Leitner *et al.* did not observe any saturation on the 28 GHz

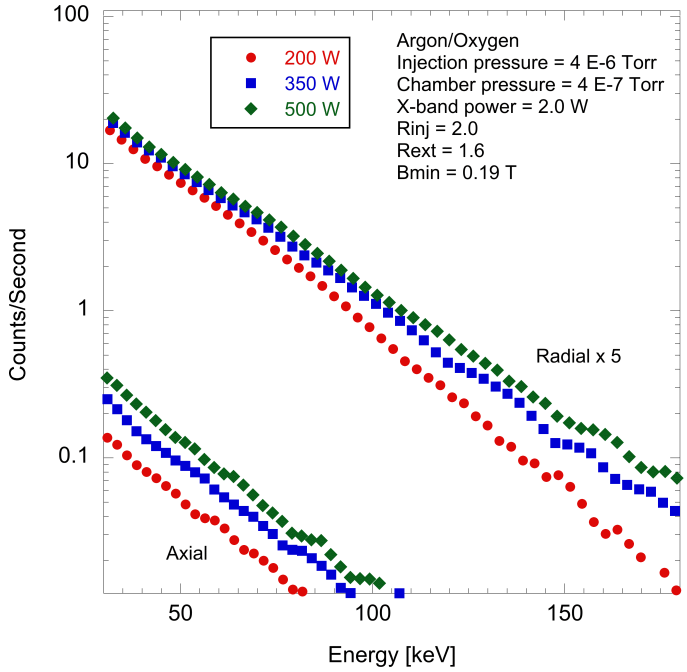


Figure 5.2.1: ECR (6.4 GHz): Radial and axial x-ray spectra at three different microwave powers.

ECRIS, makes sense (we note that the extraction electrode was visible in that experiment). It is interesting that, in the axial direction, we do not observe a saturation of x-ray power. Instead the x-ray power behaves linearly with microwave power. One possible explanation for this observation could be the alignment of the axial collimators. If the alignment is off, a small portion of the extraction plate would be visible. Hence, we would observe bremsstrahlung created by electrons striking these surfaces.

Shown in Fig. 5.2.3 is another plot of radial and axial x-ray power versus microwave power. However, in this instance, we rearranged the collimation in such a way that the plasma chamber walls became visible to the detectors. Additionally, the source settings are different from those for the data shown in Fig. 5.2.1. The data in Fig. 5.2.3 is not corrected for differences in the visible plasma volume in the radial and axial direction as the exact solid angles are not known. Because the walls of the ion source are visible, it is possible to observe thick target bremsstrahlung created when electrons collide with them. The result is that, radially the x-ray power does not saturate at larger microwave powers. This behavior was discussed earlier in Chap. 3, where it was explained that an increase in the pitch-angle scattering diffusion coefficient with microwave power causes more, and more electrons to be lost from the plasma. These lost electrons then collide with the sextupoles, creating very intense x-rays. In the axial direction, the x-ray power increases at a faster rate, $x^{2.236}$, versus linearly when fully collimated, which is most likely due to the much larger solid angle.

The radial and axial spectral temperatures calculated from the data shown in Fig. 5.2.1 are shown in Fig. 5.2.4 as a function of microwave power. The energy range used to calculate the

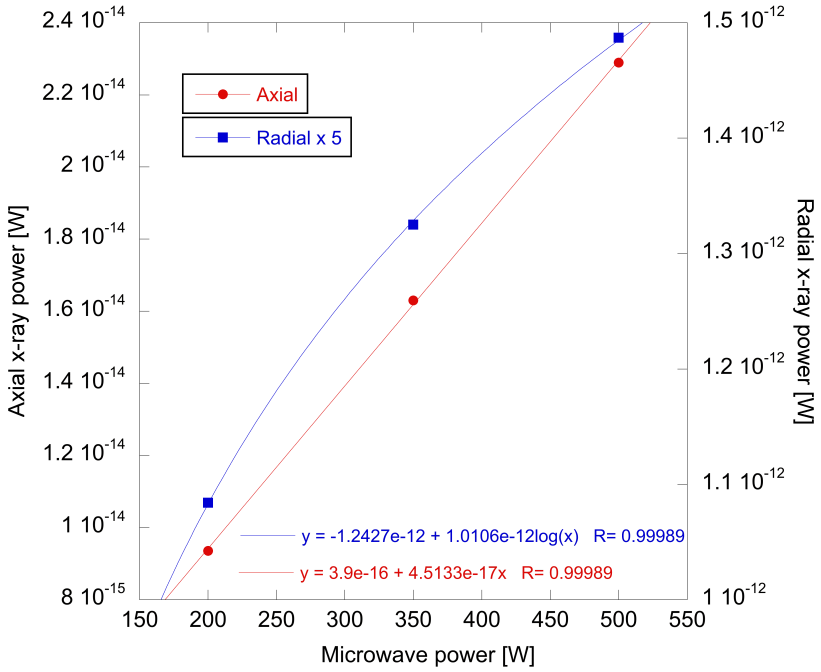


Figure 5.2.2: ECR(6.4 GHz): X-ray power versus microwave power.

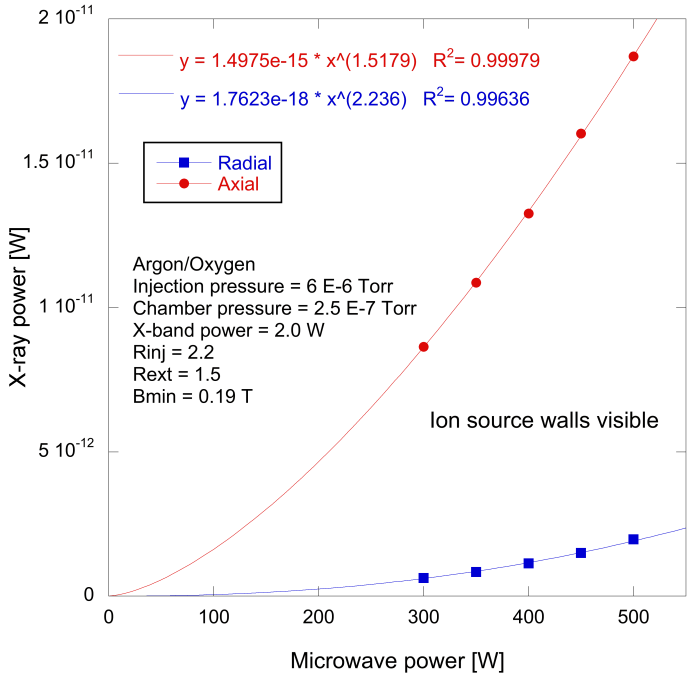


Figure 5.2.3: ECR(6.4 GHz): Axial and radial x-ray power versus microwave power. Plasma chamber visible to detectors.

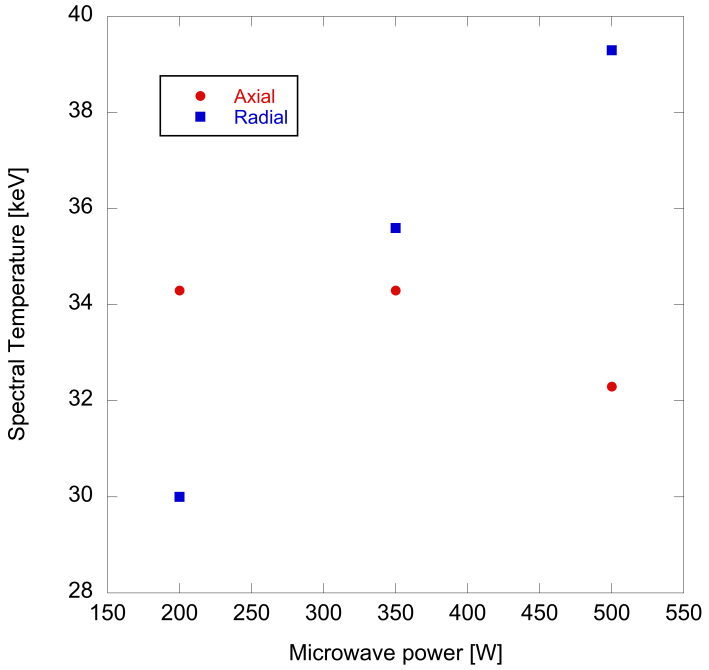


Figure 5.2.4: ECR(6.4 GHz): Spectral temperature versus microwave power.

spectral temperature is 30-100 keV for the axial data, and 30-120 keV for the radial data. The difference between radial and axial spectral temperatures for the ECR are small. In the radial direction, there is a slight increase in spectral temperature with microwave power. In the axial direction, however, the spectral temperature remains essentially constant, between 32 keV and 34 keV.

### 5.2.2 AECR-U results

Figure 5.2.5 shows radial and axial x-ray spectra taken on the AECR-U, operating in dual frequency mode at several 14 GHz powers, and 145 W of 12.56 GHz power, which was kept constant. The ratio of axial to radial visible plasma volume for the settings shown in Fig. 5.2.5 is approximately 13. As can be seen in Fig. 5.2.5 the maximum recorded x-ray energy in the radial direction is over 400 keV. For the axial case, it is approximately 200 keV. This difference, a 100 % increase, is larger than is seen on the ECR, which showed an approximate 50 % increase in maximum detected x-ray energy between the axial and radial directions. We again see that in spite of the fact that the volume visible to the axial detector is 13 times larger than the volume visible to the radial detector, the count rate in the radial direction remains much larger than in the axial direction.

Figure 5.2.6 shows the x-ray power, based on the data shown in Fig. 5.2.5,measured in both the radial and axial directions, as a function of the input microwave power for the AECR-U. The radial x-ray power increases linearly with microwave power, and does not saturate in the range of microwave powers we examined. The axial x-ray power also is most closely fit with a line. The radial behavior differs from that observed in the ECR, shown in Fig. 5.2.2, where

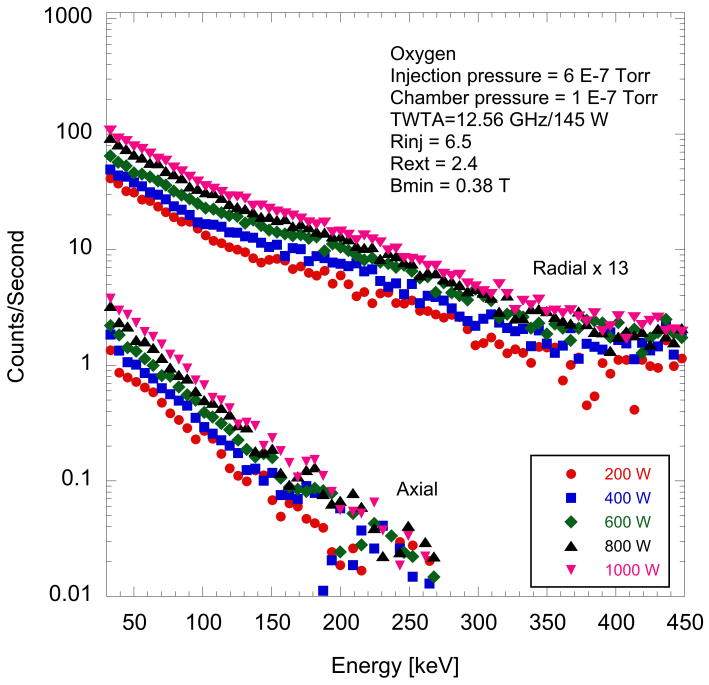


Figure 5.2.5: AECR-U (14 GHz + 12.56 GHz): Radial versus axial x-ray spectra. Oxygen plasma.

the radial x-ray power was shown to increase logarithmically. However, the axial x-ray power increases linearly on both the AECR-U and ECR. Recall, that for the data shown in Fig. 5.2.5, a small portion of the extraction plate is visible to the axial detector. On average, the recorded x-ray power in the radial direction is 10 times larger than it is in the axial direction. The linear increase in axial x-ray power with respect to microwave power is in agreement with previous studies by Leitner *et al.* (the extraction electrode was visible)[34] and Xie[54], in which x-rays were measured axially.

Figure 5.2.7 shows the spectral temperature, calculated from the data shown in Fig. 5.2.5, of the radial and axial x-rays as a function of the microwave power. The spectral temperature is calculated using an energy range between 30-140 keV in the axial direction, and 30-300 keV in the radial direction. The axial spectral temperature remains close to 80 keV throughout the microwave power range. In the radial direction, the spectral temperature first increases from a value of approximately 230 keV at 200 W to a value of nearly 270 keV at 600 W, then returns to a value of 230 keV at 800 and 1000 W, with an average value of 240 keV. The essentially constant spectral temperature has also previously been shown change very little with microwave power[34]. Unlike in the ECR, where the axial and radial spectral temperatures are nearly identical, the radial spectral temperature in the AECR-U is close to twice as large as the axial spectral temperature, indicating that the anisotropy in radial an axial spectral temperatures seems to grow with operating frequency.

Another detail that can be learned from Fig.'s 5.2.1 and 5.2.5 is that the detected x-ray energy emmited by the AECR-U plasma extends to much higher energies than the x-ray spectra

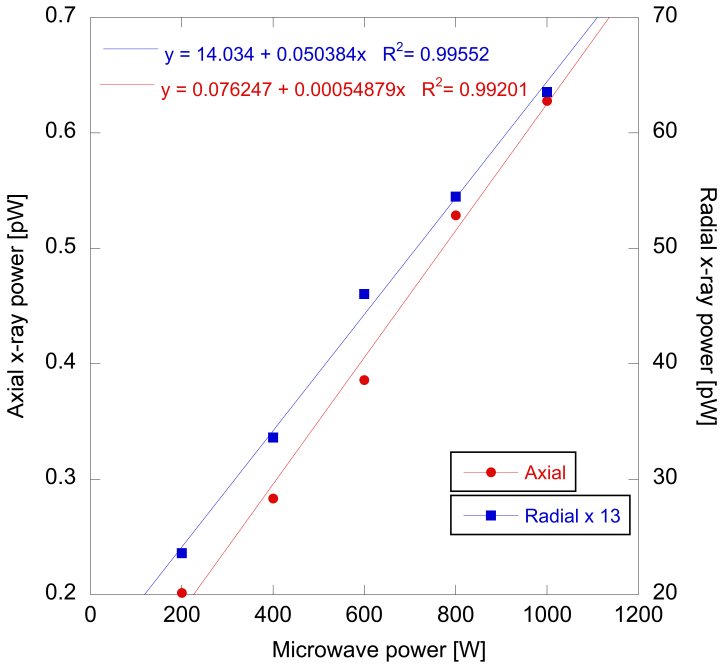


Figure 5.2.6: AECR-U (14 GHz + 12.56 GHz): X-ray power versus microwave power. AECR-U.

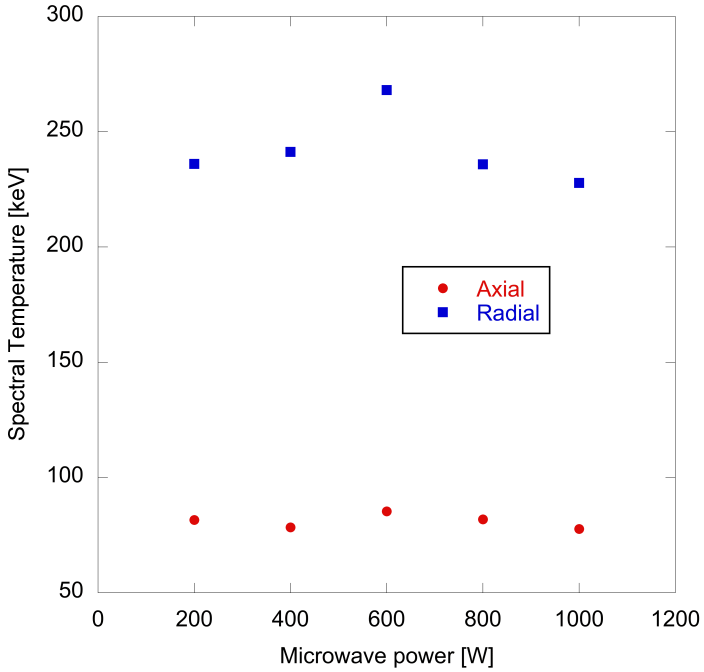


Figure 5.2.7: AECR-U (14 GHz + 12.56 GHz): Spectral temperature versus microwave power. AECR-U.

emitted by the ECR plasma. In the radial direction, for example, over 400 keV compared to approximately 150 keV for the ECR, and over 200 keV compared to 100 keV in the axial direction. This observed energy anisotropy between radially and axially measured x-ray energies is in agreement with both the transverse (to the local magnetic field) nature of the electron cyclotron heating mechanism, discussed earlier in Chap. 2, and the fact that most of the power radiated by a particle during a collision will be in the forward direction for particles with energies of 50 keV or greater (see, for example [20] or Fig. 2.3.2). In addition, if a photon of energy 100 keV, for example, is detected, it is reasonable to assume that there must have been an electron with energy of at least 100 keV in the plasma at one time (Fig. 2.3.1). Thus, the anisotropy in x-ray energy (radial versus axial) translates to an anisotropy of the electron energy distribution in the plasma. The much larger anisotropy in axial and radial x-ray (electron) energies on the AECR-U is likely due to its increased magnetic confinement and lower operating pressures. Longer lifetimes will lead to more passes through the ECR resonance region, and hence more heating.

In addition to the x-ray energy, the x-ray count rates coming from the AECR-U are higher than those coming from the ECR, in both the radial and axial direction. These will be compared directly in the following section.

### 5.2.3 Comparison between ECR and AECR-U

We have shown that the radial x-ray count rate is higher than the axial x-ray count rate, for both the ECR and AECR-U, even though the axial detectors see a larger volume of plasma. This result differs from that observed by Kato *et al.*[29], as mentioned earlier. This most likely caused by the fact the both the radial and axial detectors used in our study have clear line-of-sight to the resonance zone, as opposed to the detectors used by Kato. We have also seen that the x-ray count rates coming from the AECR-U are much larger than those coming from the ECR. In this section we will directly compare the x-ray power coming from the ECR and AECR-U.

Shown in Fig. 5.2.8 are plots of x-ray power per unit volume (volume visible to the detector) as a function of microwave power per unit volume (volume of the resonance zone) for both the ECR and AECR-U. The ion source settings for this are identical to those in Fig. 5.2.1 and Fig. 5.2.5. On the left is the axial x-ray power per unit volume, and on the right is the radial x-ray power per unit volume. We can clearly see that for a given power density (microwave power per unit volume) the AECR-U produces higher x-ray powers in both the axial and radial directions.

The next question we wanted to answer was what effect does the microwave frequency have on the ratio of radial to axial x-ray power. In other words, does the driving frequency of the ECRIS have a significant impact in determining the anisotropy in the x-ray power. In Fig. 5.2.9 we show the ratio of radial to axial x-ray power per unit volume as a function of the microwave power density. For a given microwave power density, we can see that the anisotropy in x-ray power is significantly larger in the AECR-U than in the ECR. Increasing the microwave frequency from 6.343 GHz to 14.3 GHz (slightly more than doubled) results in the the average value of the ratio of x-ray power density is approximately three times bigger

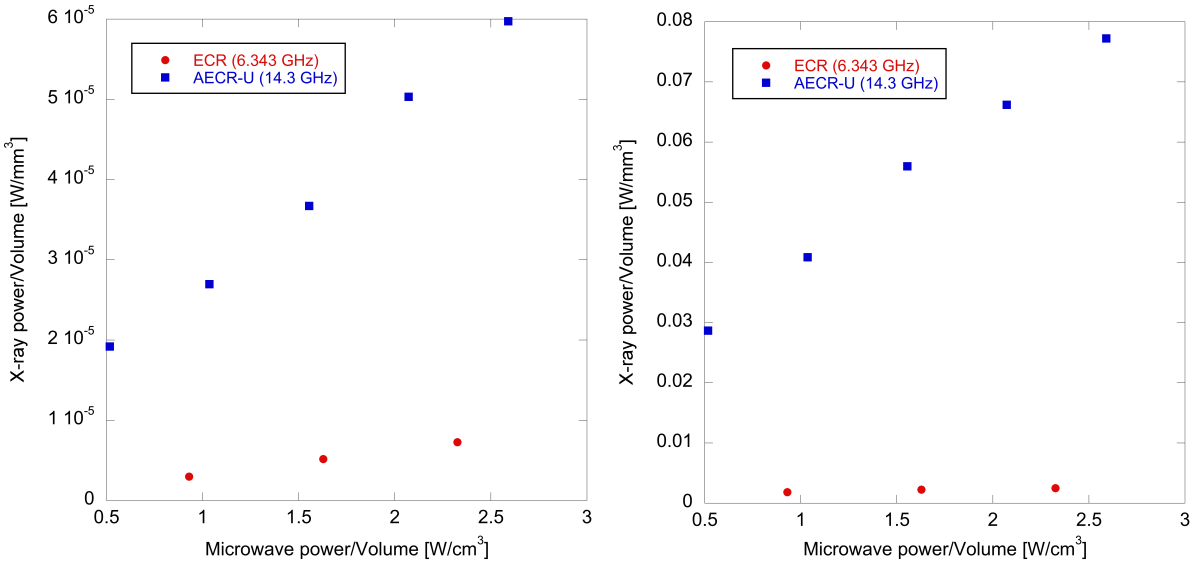


Figure 5.2.8: X-ray power per unit volume (volume visible to detector) as function of microwave power per unit volume (resonance zone volume) for ECR and AECR. Left: Axial. Right: Radial.

for the AECR-U. It is important to realize that the anisotropy difference is, most likely, not due to frequency alone. Increasing the frequency of a source necessarily implies an increase in confinement strength in order to keep the resonance zone within the plasma chamber. The stronger magnetic fields also play an important role in the anisotropy of the x-ray power, as we will show in a following section.

Based on this limited data set, we would expect that the anisotropy in x-ray power density would continue to grow as the driving frequency is increased, and that the latest generation of ECRIS, such as VENUS[35], would have much larger flux of x-rays in the radial direction than in the axial direction (though the flux in axial direction is still quite high[34]). For superconducting sources, like VENUS, this poses a significant heat load problem for the cyrostat, which is wrapped around the plasma chamber.

## 5.3 Experimental results: presence of very high energy x-rays

Shown in Fig. 5.3.1 and 5.3.2 are x-ray spectra taken when the collimation is changed to increase the solid angle to the point that solid material becomes visible to the detectors. In the axial direction, this means that the extraction plate (and likely the puller) is visible to the detector. While in the radial direction, the sextupoles become visible. Two effects can be seen. The first is the appearance of large bumps in the spectra. These are most likely caused by a combination of attenuation of the photons through the various materials in the source, as well as Compton scattering. The more interesting effect is a large increase in maximum recorded

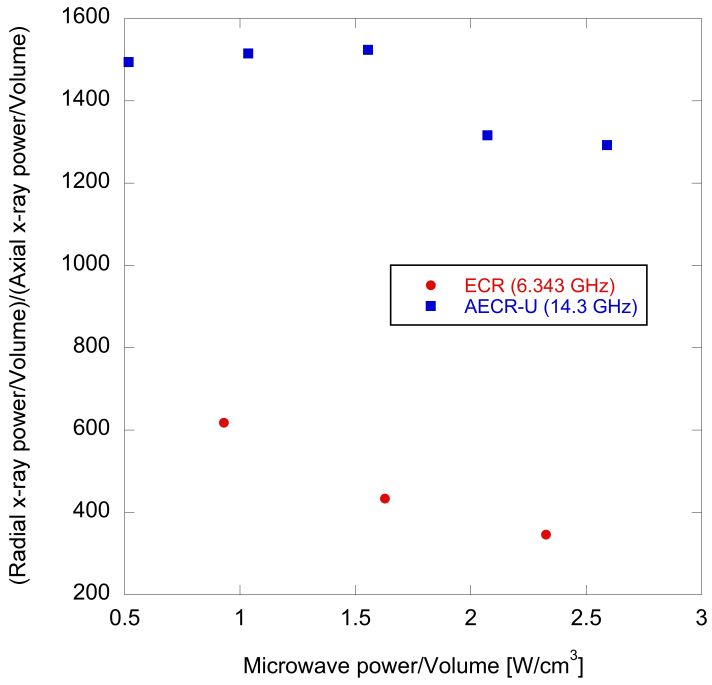


Figure 5.2.9: Ratio of radial to axial x-ray power density as function of microwave power density for both ECR and AECR-U.

x-ray energy for both the ECR and the AECR-U, in both the radial and axial directions. X-rays with energies of 800 keV are seen coming from the AECR-U, and x-rays with energies of over 400 keV are detected coming from the ECR.

The presence of these very high energy x-rays shown in Fig.'s 5.3.1 and 5.3.2 is somewhat surprising. The cyclotron frequency, $\omega_c = qB/\gamma m$, of a particle is inversely proportional to its mass, and the Lorentz factor, $\gamma$. At low energies, the Lorentz factor is nearly one, and the cyclotron frequency is independent of the velocity of the electron. However, as the velocity of the electron is increased, the Lorentz factor will become large enough that the cyclotron frequency will change. In order for the electron to stay in resonance with the driving microwave frequency, and continue to be heated, the resonance zone must move to a region of higher magnetic field strength. Thus, one can estimate the maximum kinetic energy an electron can attain, based on the maximum magnetic field strength point in the ion source with the following equation:

$$W_{Max} = \frac{|e| B_{Max} c^2}{2\pi f} - mc^2, \tag{5.3.1}$$

where $m$ is the mass of an electron, $B_{Max}$ is the maximum magnetic field strength that an electron is expected to experience, and $f$ is the driving microwave frequency. This equation is plotted for three different frequencies in Fig. 5.3.3.

We estimate the maximum magnetic field using the following equation[22]:

$$B_{Last}^2 = B_{min}^2 + B_{rad}^2, \tag{5.3.2}$$

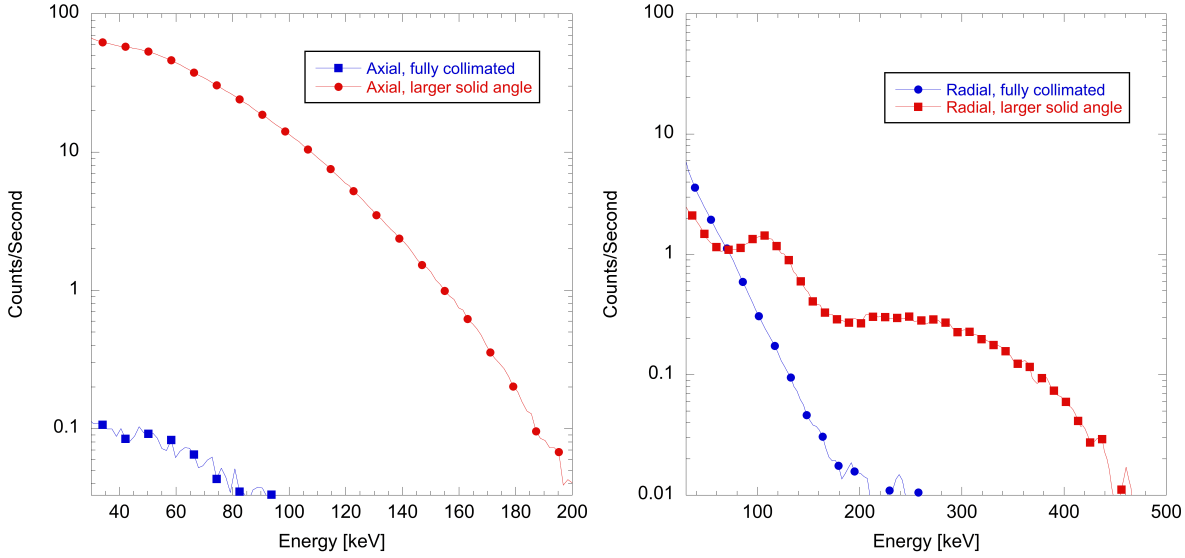


Figure 5.3.1: ECR (6.4 GHz): X-ray spectra with only plasma viewable and with structure viewable. 500 W. Left: axial. Right: radial.

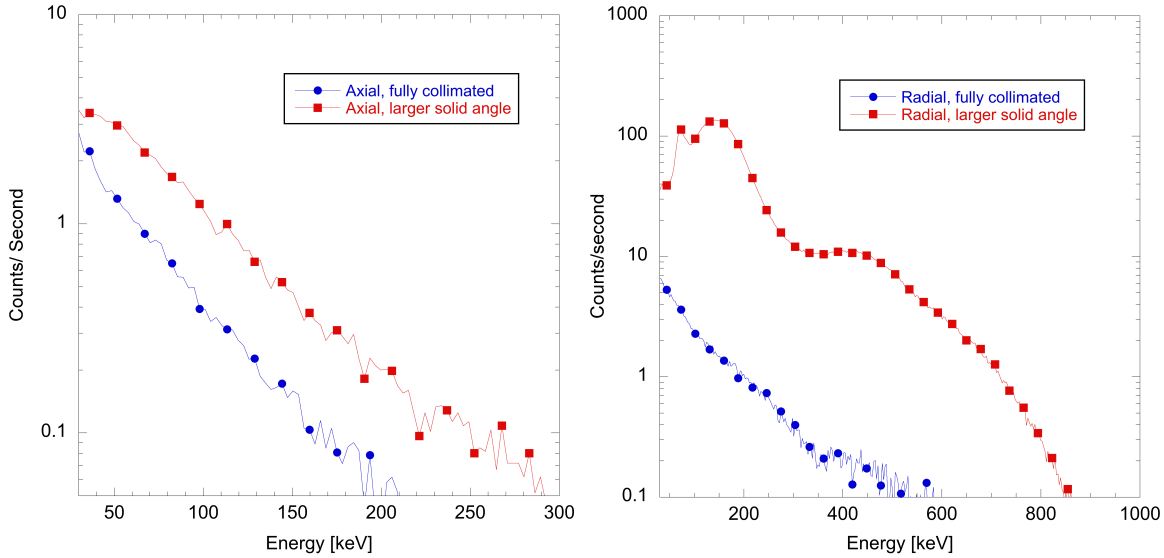


Figure 5.3.2: AECR-U (14 GHz): X-ray spectra with only plasma viewable and with structure viewable. 600 W. Left: axial. Right: radial.

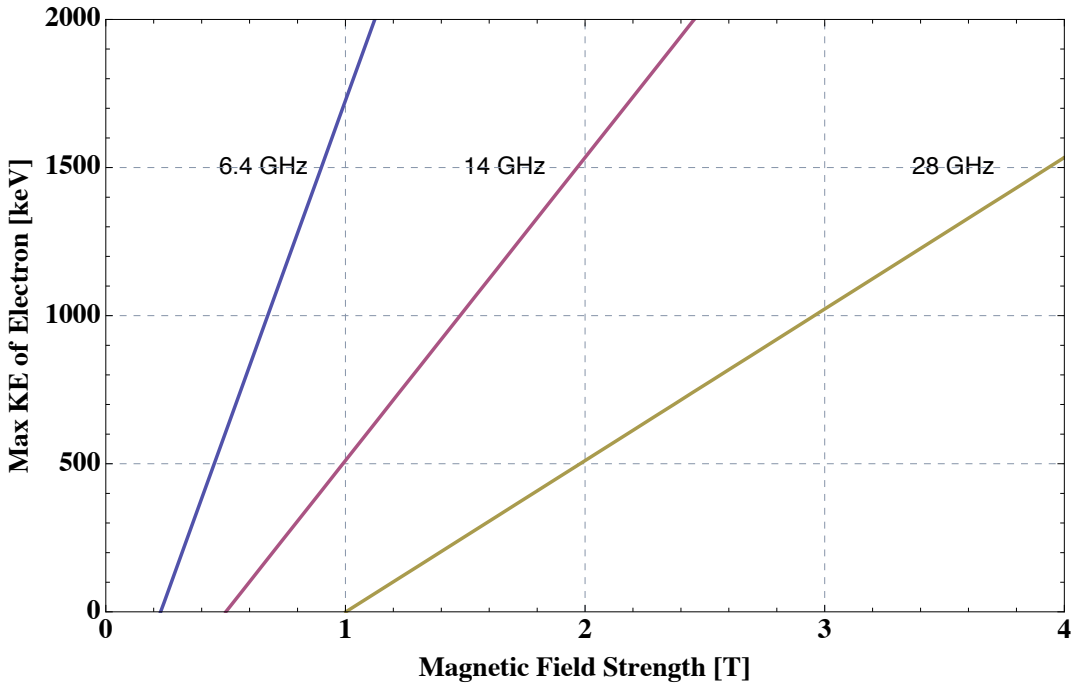


Figure 5.3.3: Predicted maximum energy of an electron as a function of microwave frequency and maximum magnetic field strength.

where $B_{min}$ is the minimum mirror field strength, $B_{rad}$ is the magnitude of the radial magnetic field at the chamber wall, and $B_{Last}$ defines the last closed magnetic surface within the chamber. In the ECR, the maximum radial magnetic field strength within the plasma chamber is 0.4 T and $B_{min} \cong 0.19$ T for the data shown in Fig. 5.3.1, and so $B_{Last} \cong 0.44$ T. This translates to a maximum energy of approximately 470 keV. For the AECR-U the maximum radial field strength is 0.85 T and $B_{min} \cong 0.38$ T for the data shown in Fig. 5.3.2. $B_{Last}$ is thus equal to approximately 0.93 T, which translates to an electron energy of 420 keV. From Chapter 2 we know that there is a small probability that a photon can be created with energy near that of the electron. However it is much more likely that a photon of lower energy will be created. Based on this fact, if we are to believe the results predicted by Eq. 5.3.1, then the maximum photon energy we should detect in the ECR is 470 keV, and 420 keV in the AECR-U. For the ECR, this energy is close to the maximum photon energy detected, however for the AECR-U this energy is much less than the the maximum x-ray energy seen in Fig. 5.3.2.

A second method of calculating the maximum electron energy is to simply use the maximum magnetic field that an electron might encounter in the plasma chamber. This field point may not lie on a closed magnetic field surface. In the AECR-U, for example, the maximum magnetic field is approximately 1.48 T for the data shown in Fig. 5.3.2, and occurs at the surface of the bias disk. If we use this number, then the predicted maximum electron energy based on Eq. 5.3.1 is approximately 1 MeV, well above the x-ray energies seen in Fig. 5.3.2.

Because changing the x-ray collimation system obviously has no effect on the plasma, it can be concluded that these higher energy x-rays (electrons) were always present. Their

appearance in the spectrum is most likely attributed to x-rays, created by unconfined electrons striking solid surfaces, becoming suddenly visible. From Eq. 2.3.3 (Chap. 2), we can see the strong dependence of the cross section on the atomic number. Electrons moving through chamber materials, which are typically made from high Z materials, will have a much larger probability of creating photons. This should lead to an increase in both x-ray count rates and x-ray energy, which is seen in Fig. 5.3.1 and Fig. 5.3.2. It is important to characterize x-rays caused both by confined electrons and lost electrons, as it is the total x-ray flux that deposits energy into the cryostat, but only the former that characterizes the plasma.

## 5.4 Experimental results: effect of magnetic field configuration

In this section we discuss the effect that magnetic field configuration has on the both the radial and axial x-ray production in the AECR-U. To perform this study the currents in the magnet coils were varied from 390 A up to 460 A. The currents in all six magnet coils were set equal. This will not optimize the source for any particular ion charge state. We are not, however, interested in maximizing extracted ion currents, only in observing trends in x-ray production. The AECR-U is run in single frequency mode, operating at 14.3 GHz, with a constant power level of 450 W. Identical NaI(Tl) detectors were used in this study, and so the only correction made to the x-ray spectra are for absorption of photons by intervening materials and differences in the visible plasma volume.

Varying the magnetic field settings results in changes to the mirror ratios and gradients, as well as the volume of the resonance zone and the volumes visible to the individual detectors. A summary of the changes to the mirror ratios and gradients is given in Table 5.1 and the axial field profile is given in Fig. 5.4.1. In Table 5.1 the radial mirror ratio, $R_{rad}$, is defined as the ratio of the radial magnetic field at the wall (0.75 T) to minimum magnetic field, $B_{min}$. We see that increasing the magnetic field strength decreases the mirror ratios and the gradient of the magnetic field in the resonance zone, which we have previously shown to be a key parameter in determining electron behavior. In Table 5.2 we summarize the effect of solenoid current strength on different plasma volumes. The plasma volume and the volume visible to the axial detector both decrease as the magnitude of the coil currents increases. The volume of plasma visible to the radial detector remains nearly constant.

Figure 5.4.2 shows the radial and axial x-ray spectra as a function of $B_{min}/B_{ecr}$. The radial spectra have been scaled by the ratios of the plasma volume visible to axial detector over the plasma volume visible to the radial detector, which are given in Table 5.2. The typical trends of larger x-ray count rates and x-ray energies in the radial direction can again be seen.

In Fig. 5.4.3 we see that the radial spectral temperature increases in a continuous manner as $B_{min}/B_{ecr}$ is increased. This trend was also seen in measurements of low energy x-rays that were discussed in Chapter 3. In that chapter, we saw that higher energy electrons (30-60 keV) were more sensitive to changes in $B_{min}/B_{ecr}$ than lower energy electrons (4-20 keV). The fact that the radial spectral temperature changes dramatically with $B_{min}/B_{ecr}$ makes sense, then, as the mean

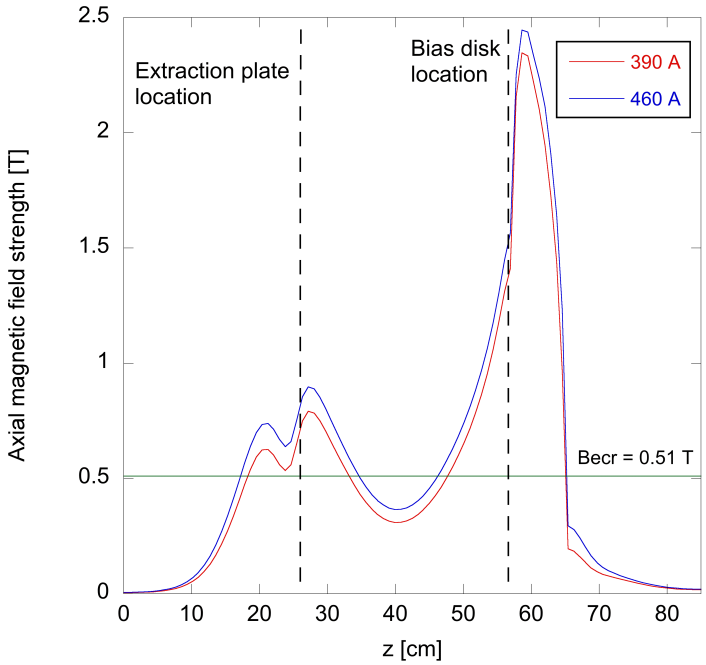


Figure 5.4.1: Axial magnetic field profile.

| Solenoid currents [A] | $B_{min}/B_{ecr}$ | $R_{inj}$ | $R_{ext}$ | $R_{rad}$ | $\nabla B_{inj}$ [G/cm] | $\nabla B_{ext}$ [G/cm] |
|---|---|---|---|---|---|---|
| 390 | 0.606 | 4.19 | 2.56 | 2.43 | 541 | -506 |
| 400 | 0.622 | 4.15 | 2.54 | 2.37 | 536 | -503 |
| 410 | 0.638 | 4.11 | 2.53 | 2.31 | 530 | -499 |
| 420 | 0.653 | 4.07 | 2.51 | 2.26 | 524 | -496 |
| 430 | 0.669 | 4.03 | 2.49 | 2.19 | 518 | -491 |
| 450 | 0.701 | 3.95 | 2.47 | 2.09 | 502 | -478 |
| 460 | 0.717 | 3.92 | 2.45 | 2.06 | 493 | -471 |

Table 5.1: Effect of solenoid current strength on different magnetic field parameters .

| Solenoid currents [A] | Plasma vol. [$cm^3$] | Axial [$cm^3$] | Radial [$cm^3$] |
|---|---|---|---|
| 390 | 628 | 14.1 | 0.9116 |
| 400 | 600 | 13.8 | 0.9115 |
| 410 | 573 | 13.4 | 0.9114 |
| 420 | 544 | 12.8 | 0.9113 |
| 430 | 518 | 12.5 | 0.9111 |
| 450 | 465 | 11.7 | 0.9111 |
| 460 | 438 | 11.3 | 0.9109 |

Table 5.2: Effect of solenoid current strength on plasma volume and the volumes visible to each detector.

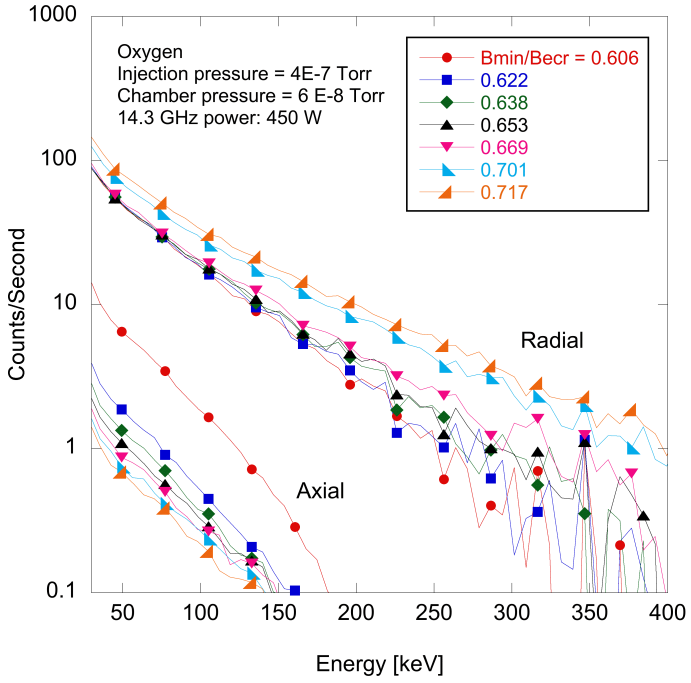


Figure 5.4.2: AECR-U (14.3 GHz): Radial and axial x-ray spectra as function of ratio Bmin/Becr.

energy of the electrons is quite high (> 100 keV). The fact that it increases with $B_{min}/B_{ecr}$ can be attributed to the decrease in the gradient of the magnetic field in the resonance zones. The axial spectral temperature increases until $B_{min}/B_{ecr} = 0.67$, after which it appears to level off. An increase in spectral temperature, measured axially, was also seen in a study by Zhao *et al.*[56]. However, in that study the spectral temperature rose continuously, in a nearly linear fashion with $B_{min}/B_{ecr}$. Finally, we see that the radial spectral temperature is, again, greater than the axial spectral temperature, a trend we see consistently on the AECR-U.

Figure 5.4.4 shows the radial and axial x-ray power as a function of $B_{min}/B_{ecr}$. The radial x-ray power increases, however the axial x-ray power is shown to decrease. This causes the ratio of radial to axial x-ray power to rise rapidly with $B_{min}/B_{ecr}$, as shown in Fig. 5.4.5. An 18% increase in $B_{min}/B_{ecr}$ results in an approximate 2600 % increase in the ratio of radial to axial x-ray power. The increase in radial x-ray power is most likely due to the increased heating efficiency associated with the decrease in the gradient of the magnetic field in the resonance zone (Table 5.1). The decrease in axial x-ray power is harder to explain. From Table 5.1 we can see that as $B_{min}/B_{ecr}$ increases, the mirror ratios at both injection and extraction decrease. This should increase the size of the mirror loss cones (Eq. 2.1.29), and thus increase the number of electrons lost axially. Additionally, as mentioned earlier, a small area of the extraction plate is visible to the axial detector. Unless the electrons are being lost at a radius outside of the collimator view, we would expect to see an increase in the detected x-ray power, not a decrease. Another possible explanation to the fact that the axial x-ray power decreases is that the radial mirror ratio decreases at a faster rate than the extraction mirror ratio, as can be seen in Table 5.1. This

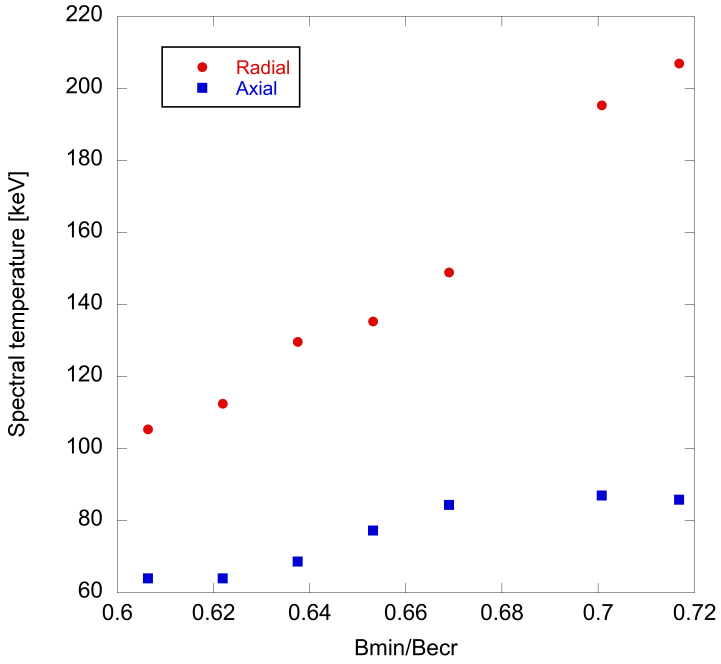


Figure 5.4.3: AECR-U (14.3 GHz): Radial and axial spectral temperatures as function of Bmin/Becr.

would cause more electrons to be lost in a radial direction than in an axial direction as $B_{min}/B_{ecr}$ is increased.

## 5.5 Conclusions

This chapter showed that x-ray production in an ECRIS plasma is highly anisotropic, with radial x-ray counts being much greater than axial x-ray counts. This was shown to be true for both the ECR (6.343 GHz) and the higher performance AECR-U (14.3 GHz). Based on this, we can make the qualitative statement that the electron energy is also highly anisotropic, with a much larger perpendicular energy than parallel energy. The degree of anisotropy correlated with frequency for two different ion sources. This increase is most likely attributable to the higher power density and greater confinement associated with higher performance machines.

The radial spectral temperature on the AECR-U is over twice as large as the axial spectral temperature. However, in the ECR the radial and axial spectral temperatures were similar. Hence, the anisotropy in spectral temperature also shows dependence on the magnetic field strength and operating frequency of the ECRIS. The combination of higher energies, and intensity of high energy x-rays in the radial direction has important implications in the x-ray heat load estimates for superconducting ECR ion source cryostats.

The presence of very high energy electrons is inferred based the measurement of high energy x-rays. It was shown that the energy of the electrons can exceed that predicted by the relativistic change in cyclotron frequency, if we base our estimate on the last closed magnetic

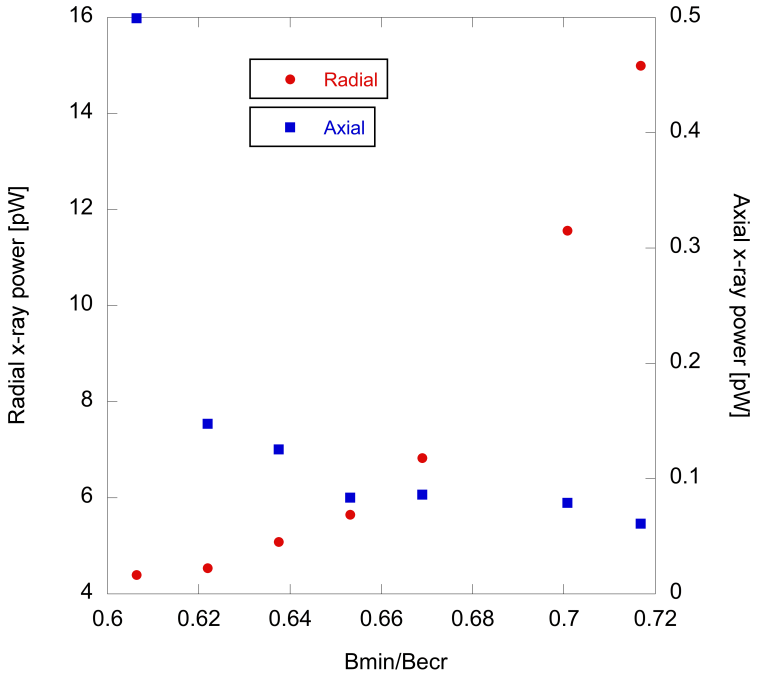


Figure 5.4.4: AECR-U (14.3 GHz): Radial and axial x-ray power as function of Bmin/Becr.

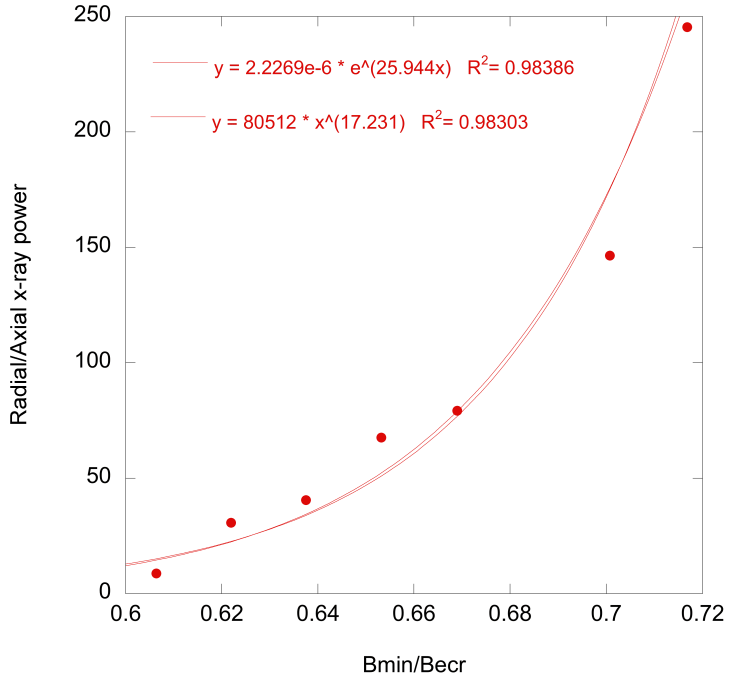


Figure 5.4.5: AECR-U (14.3 GHz): Ratio of radial to axial x-ray power as function of Bmin/Becr.

surface within the plasma chamber . However, if we simply take the maximum magnetic field strength within the plasma chamber (not necessarily on a closed surface), then the detected x-ray energies are reasonable.

Finally, we discussed the effect of the magnetic field on both the radial and axial x-ray counts and energies. We showed that the ratio of radial to axial x-ray power increased dramatically with $B_{min}/B_{ecr}$. We suggested that the reason the axial x-ray power decreased with an increase in $B_{min}/B_{ecr}$ is due to the fact that the radial mirror decreases at a faster rate than the extraction mirror. This would cause a larger loss of electrons in radial direction, rather than in the axial direction.

# Chapter 6

# Conclusions and suggested future work

## 6.1 Conclusions

The goal of this dissertation was to gain an understanding of the relative importance of microwave power, neutral pressure, and magnetic field configuration on the behavior of the hot electrons within an ECRIS plasma. This was carried out through measurement of plasma bremsstrahlung with both NaI(Tl) ($h\nu > 30$ keV) and CdTe (2 keV $< h\nu <$ 70 keV) x-ray detectors, and through measurement of the plasma energy density with a diamagnetic loop placed around the plasma chamber. We also examined the anisotropy in x-ray power by simultaneously measuring the x-ray spectra in two orthogonal directions: radially and axially.

In Chapter 3 we showed that for a 6.4 GHz ECRIS, both the x-ray power due to confined electrons and the plasma energy density behave logarithmically with microwave power. The x-ray flux created by electrons lost from the plasma, however, does not saturate. Thus, the small increase in plasma density that occurs at high microwave powers (> 150 W on the 6.4 GHz ECR) will be accompanied by a large increase in total x-ray power. We suggest that the saturation is due to rf-induced pitch-angle scattering, which was first proposed by Perret *et al.* [41].

X-ray power and plasma energy density are also shown to saturate with neutral pressure, and to increase nearly linearly as the gradient of the magnetic field in the resonance zone is decreased. All of these findings are in agreement with the theoretical models describing ECR ion source plasmas.

In Chapter 4 we discussed the use of a diamagnetic loop as a means of exploring various plasma time scales on a relative basis. Specifically, we focused much of our attention on studying how changing ion source parameters, such as microwave power and neutral pressure, would effect the rise and decay of the integrated diamagnetic signal (which can be related to plasma energy density, see Eq. 2.1.42). We showed that increasing microwave power lowers the e-fold times at both the leading edge and the trailing edge of the microwave pulse. The fact that decay times increase with microwave power, makes sense based on the electron-ion collisional frequency, $\nu_{ei}$. Microwave power, however, has almost no impact on the ignition times of the plasma.

The plasma energy density e-fold times were shown to be insensitive to both neutral pres-

sure and magnetic field setting. Neutral pressure, however, can have a dramatic effect on the time of first appearance of the diamagnetic signal ("plasma ignition time"). In addition to neutral pressure, ignition times are also a function of pulse spacing and whether or not the first stage of the 6.4 GHz ECR is on. We suggest that the insensitivity of decay times to magnetic field setting is due to the fact that the perpendicular diffusion coefficient (Eq. 4.4.1), which is proportional to the ratio of electron energy to magnetic field strength, remains essentially constant as the magnetic field strength is increased. In all cases, the rise time of the integrated diamagnetic signal was seen to be faster than the decay time.

Typically, except for He $1^+$, the ion currents did not appear in measurable amounts until a few milliseconds after the diamagnetic signal. Had we measured the very low charge states of Argon ($1^+$, $2^+$, etc.) it is probable that they would have appeared much sooner in relation to the diamagnetic signal. It was also shown that higher charge states generally appeared later, however, they also decayed away at faster rates. We suggested that peaks superimposed on the decaying portion of the diamagnetic signal at the trailing edge of the microwave pulse were caused by a radial expulsion of charged particles.

By comparing the diamagnetic signal to the ratio of reflected to forward power we theorized that the initial, exponential rise in the diamagnetic signal at the leading edge of the microwave pulse is due to rapid changes in both the average electron energy and density. During the slowly decaying portion of the loop signal, the hot tail of the electron population is increasing. This theory is supported by time resolved, low energy x-ray measurements that showed that the period of rapid change of $P_{ref}/P_{for}$ coincides with a rapid change in average photon energy. Finally, we want to emphasize that the data shown in Chapter 4 should be used for qualitative analysis only. Again, we were interested in observing trends, rather than calculating absolute values.

Chapter 5 showed that x-rays production in an ECRIS plasma is highly anisotropic, with radial x-ray counts being much greater than axial x-ray counts. This was shown to be true for both the ECR (6.4 GHz) and the higher performance AECR-U (14 GHz). Based on this, we can make the qualitative statement that the electron energy is also highly anisotropic, with a much larger perpendicular energy than parallel energy. The degree of anisotropy was shown to increase with the operating frequency of the ion source. This increase is most likely attributable to the higher power density and greater confinement associated with higher performance machines, and implies that superconducting ECRIS operating at very high frequencies will have extremely anisotropic x-ray power deposition.

The radial spectral temperature on the AECR-U is over twice as large as the axial spectral temperature. However, in the ECR the radial and axial spectral temperatures were similar. Hence, the anisotropy in spectral temperature also shows dependence on the magnetic field strength and operating frequency of the ECRIS. The combination of higher energies, and intensity of high energy x-rays in the radial direction has important implications in the x-ray heat load estimates for superconducting ECR ion source cryostats.

The presence of very high energy electrons is inferred based the measurement of high energy x-rays. It was shown that the energy of the electrons exceeds that predicted by the relativistic change in cyclotron frequency as the electron gains energy, if we base our estimate

on the last closed magnetic surface within the plasma chamber. However, if we simply take the maximum magnetic field strength within the plasma chamber (not necessarily on a closed surface), then the detected x-ray energies are reasonable.

Finally, we discussed the effect of the magnetic field on both the radial and axial x-ray counts and energies. We showed that the ratio of radial to axial x-ray power increased dramatically with $B_{min}/B_{ecr}$.

## 6.2 Suggested future work

There are still several experiments that should be carried out in order to complete the studies we discussed in this dissertation. To extend the studies discussed in Chapter 3 and Chapter 4, it would be interesting to take both diamagnetic loop and low energy x-ray measurements on an ECRIS operating at a higher frequency than 6.4 GHz. Particular attention should be paid to the saturation of x-ray power and plasma energy density with microwave power. From a theoretical standpoint, the saturation is expected to occur at larger microwave powers than those used in this study. A comparison of plasma energy density e-fold times (for formation and decay of the plasma) of two ion sources operating at different microwave frequencies would, of course, also be desirable.

Diamagnetic loop measurements are done with the ion source operating in pulsed mode. X-ray measurements were perfomed while the source was in steady state. Both of these diagnostics can be related to the electron denstiy and electron energy. It would be very interesting to, in conjuction with diamagnetic loop measurements, simultaneously make time resolved low and high energy x-ray measurements.

We were able to measure high x-rays ($> 30$ keV) in the axial and radial directions. To extend this, low energy ($< 30$ keV) axial and radial measurements should be made. Based on theoretical considerations discussed in Chapter 2 we would expect that the anisotropy in measured x-ray power would decrease with x-ray energy. If possible, it would be extremely interesting to measure both axial and radial x-rays on a modern, superconducting ECRIS. However, because the cryostat that encloses the plasma chamber in these sources, it will be very difficult to obtain an unobstructed radial x-ray measurement.

# Bibliography


[1] http://www.amptek.com/anczt1.html.

[2] http://www.amptek.com/xr100cdt.html.

[3] C Barué, P Briand, A Girard, G Melin, and G Briffod. Hot electron studies in the minimafios ecr ion source. *Review of Scientific Instruments*, 63(4):2844–2846, 1992.

[4] C Barué, M Lamoureux, P Briand, A Girard, and G Melin. Investigation of hot electrons in electron-cyclotron-resonance ion sources. *Journal of Applied Physics*, 76:2662, 1994.

[5] K Bernhardi. An improved deconvolution method for bremsstrahlung spectra from hot plasmas. *Computer Physics Communications*, 19:17–21, 1980.

[6] K Bernhardi, G Fuchs, MA Goldman, HC Herbert, D Obermann, W Walcher, and K Wiesemann. Studies of electron heating and multiply charged ion production in an electron cyclotron resonance plasma. *Plasma Physics*, 18:77–94, 1976.

[7] K Bernhardi and K Wiesemann. X-ray bremsstrahlung measurements on an ecr-discharge in a magnetic mirror. *Plasma Physics*, 24(8):867–884, 1982.

[8] K.G. Budden. *Radio Waves in the Ionosphere*. Cambridge University Press, 1966.

[9] F.F. Chen. *Introduction to Plasma Physics and Controlled Fusion*. Plenum Press, second edition, 1984.

[10] B Cluggish, L Zhao, and J. S Kim. Simulation of parameter scaling in electron cyclotron resonance ion source plasmas using the gem code. *Review of Scientific Instruments*, 81(2):02A301, Jan 2010.

[11] IJD CRAIG and JC BROWN. Fundamental limitations of x-ray spectra as diagnostics of plasma temperature structure. *Astronomy and Astrophysics*, 49(2):239–250, 1976.

[12] T.J. Fessenden. Technical report 442 mit-3221-19. Technical report, M.I.T, 1966.

[13] R Friedlein, H Tyrroff, C Zippe, and G Zschornack. Characteristic x rays and electron energy distribution function in anisotropical hot plasmas. *Review of Scientific Instruments*, 67(3):1261–1263, Jan 1996.

[14] S Gammino, D Mascali, L Celona, F Maimone, and G Ciavola. Considerations on the role of the magnetic field gradient in ecr ion sources and build-up of hot electron component. *Plasma Sources Science and Technology*, 18:045016, 2009.

[15] S Gammino, J Sijbring, and AG Drentje. Experiment with a biased disk at the kvi ecris. *Review of Scientific Instruments*, 63:2872, 1992.

[16] Richard Geller. *Electron Cyclotron Resonance Ion Sources and ECR Plasmas*. Institute of Physics Publishing, 1996.

[17] A Girard, P Briand, G Gaudart, JP Klein, F Bourg, J Debernardi, JM Mathonnet, G Melin, and Y Su. The quadrumafios electron cyclotron resonance ion source: Presentation and analysis of the results. *Review of Scientific Instruments*, 65:1714, 1994.

[18] A Girard, C Pernot, G Melin, and C Lécot. Modeling of electron-cyclotron-resonance-heated plasmas. *Physical Review E*, 62(1):1182–1189, 2000.

[19] R.J. Goldston and P.H. Rutherford. *Introduction to Plasma Physics*. Taylor and Francis Group, 1995.

[20] David J. Griffiths. *Introduction to Electrodyamics*. Prentice Hall, New Jersey, 1999.

[21] Frederick W. Grover. *Inductance calculations: working formulas and tables*. Dover Publications, 1973.

[22] D Hitz. Recent progress in high frequency electron cyclotron resonance ion sources. *Advances in Imaging and Electron Physics*, 144:1–164, 2006.

[23] D Hitz, G Melin, and A Girard. Fundamental aspects of electron cyclotron resonance ion sources: From classical to large superconducting devices (invited). *Review of Scientific Instruments*, 71:839, 2000.

[24] Amptek Inc. Dead time, throughput, and pile-up in the dp4. October 2006.

[25] IV Izotov, AV Sidorov, VA Skalyga, VG Zorin, T Lamy, L Latrasse, and T Thuillier. Experimental and theoretical investigation of the preglow in ecris. *Plasma Science, IEEE Transactions on*, 36(4):1494–1501, 2008.

[26] John David Jackson. *Classical Electrodynamics*. John Wiley and Sons, Inc., New York, third edition, 1999.

[27] F Jaeger, AJ Lichtenberg, and MA Lieberman. Theory of electron cyclotron resonance heating. i. short time and adiabatic effects. *Plasma Physics*, 14:1073–1100, 1972.

[28] Y. Jongen, C. Pirate, and G. Ryckewaert. In *Proceedings of the 6th International Workshop on ECR Ion Sources, Lawrence Berkeley National Laboratory, LBNL*, pages 238–255, 1985.

[29] Y Kato, Y Kubo, and S Ishii. Pulse height analysis using si-pin diode of x-ray irradiated from a 2.45 ghz electron cyclotron resonance multicharged ion source. *Review of Scientific Instruments*, 69(2):1179–1181, Jan 1998.

[30] Glenn F. Knoll. *Radiation Detection and Measurement*. John Wiley and Sons, Inc., New York, 2000.

[31] H Koivisto, P Heikkinen, V Hänninen, A Lassila, H Leinonen, V Nieminen, J Pakarinen, K Ranttila, J Ärje, and E Liukkonen. The first results with the new jyfl 14 ghz ecr ion source. *Nuclear Instruments and Methods in Physics Research Section B: Beam Interactions with Materials and Atoms*, 174(3):379–384, 2001.

[32] AF Kuckes. Resonant absorption of electromagnetic waves in a non-uniformly magnetized plasma. *Plasma Physics*, 10:367–380, 1968.

[33] M Lamoureux, P Waller, P Charles, and NB Avdonina. Bremsstrahlung from thick targets and a diagnostic for electron energy distributions. *Physical Review E*, 62(3):4091–4095, 2000.

[34] D Leitner, JY Benitez, CM Lyneis, DS Todd, T Ropponen, J Ropponen, H Koivisto, and S Gammino. Measurement of the high energy component of the x-ray spectra in the venus electron cyclotron resonance ion source. *Review of Scientific Instruments*, 79:033302, 2008.

[35] D Leitner, CM Lyneis, SR Abbott, D Collins, RD Dwinell, ML Galloway, M Leitner, and DS Todd. Next generation ecr ion sources: First results of the superconducting 28ghz ecris–venus. *Nuclear Inst. and Methods in Physics Research, B*, 235(1-4F):486–493, 2007.

[36] Michael A. Lieberman and Allan J. Lichtenberg. *Principles of Plasma Discharges and Materials Processing*. Wiley-Interscience, second edition, 2005.

[37] C.M. Lyneis. Operating experience with the lbl ecr source. In J. Parker, editor, *International Conference on ECR Ion Sources and their Applications*, pages 42–56, 1987.

[38] G Melin, F Bourg, P Briand, J Debernardi, M Delaunay, R Geller, B Jacquot, P Ludwig, T. K N'guyen, L Pin, M Pontonnier, J. C Rocco, and F Zadworny. Some particular aspects of the physics of the ecr sources for multicharged ions. *Review of Scientific Instruments*, 61(1):236, Jan 1990.

[39] D.R. Nicholson. *Introduction to Plasma Theory*. Krieger Publishing Company Florida, 1983.

[40] J Noland, J. Y Benitez, D Leitner, C Lyneis, and J Verboncoeur. Measurement of radial and axial high energy x-ray spectra in electron cyclotron resonance ion source plasmas. *Review of Scientific Instruments*, 81(2):02A308, Jan 2010.

[41] C Perret, A Girard, H Khodja, and G Melin. Limitations to the plasma energy and density in electron cyclotron resonance ion sources. *Physics of Plasmas*, 6:3408, 1999.

[42] T Ropponen, O Tarvainen, P Jones, and P Peura. The effect of magnetic field strength on the time evolution of high energy bremsstrahlung radiation created by an electron cyclotron resonance ion source. *Nuclear Inst. and Methods in Physics Research*, Jan 2009.

[43] T Ropponen, O Tarvainen, P Jones, P Peura, T Kalvas, P Suominen, and HA Koivisto. Time evolution of high-energy bremsstrahlung and argon ion production in electron cyclotron resonance ion-source plasma. *Plasma Science, IEEE Transactions on*, 37(11):2146–2152, 2009.

[44] T Ropponen, O Tarvainen, V Toivanen, P Peura, P Jones, T Kalvas, H Koivisto, J Noland, and D Leitner. The effect of rf pulse pattern on bremsstrahlung and ion current time evolution of an ecris. *Review of Scientific Instruments*, 81(2):02A302, Jan 2010.

[45] George B. Rybicki and Alan P. Lightman. *Radiative Processes in Astrophysics*. Wiley-VCH, 2004.

[46] JE Stevens and JL Cecchi. Wave propagation and plasma uniformity in an electron cyclotron resonance plasma etch reactor. *Jpn. J. Appi. Phys. Vol*, 32:3007–3012, 1993.

[47] T.H. Stix. *Waves in Plasmas*. Springer-Verlag New York, 1992.

[48] O Tarvainen, T Ropponen, T Thuillier, J Noland, V Toivanen, T Kalvas, and H Koivisto. The role of seed electrons on the plasma breakdown and preglow of electron cyclotron resonance ion source. *Review of Scientific Instruments*, 81(2):02A303, Jan 2010.

[49] O Tarvainen, T Ropponen, and V Toivanen. Diagnostics of plasma decay and afterglow transient of an electron cyclotron resonance ion source. *Plasma Sources Science and Technology*, 19(045027), July 2010.

[50] O Tarvainen, T Ropponen, V Toivanen, and J Ärje. Plasma breakdown diagnostics with the biased disc of electron cyclotron resonance ion source. *Plasma Sources Science and Technology*, 18(035018), June 2009.

[51] O Tarvainen, P Suominen, and H Koivisto. A new plasma potential measurement instrument for plasma ion sources. *Review of Scientific Instruments*, 75:3138, 2004.

[52] MC Williamson, AJ Lichtenberg, and MA Lieberman. Self consistent electron cyclotron resonance absorption in a plasma with varying parameters. *Journal of Applied Physics*, 72:3924, 1992.

[53] NC Wyeth, AJ Lichtenberg, and MA Lieberman. Electron cyclotron resonance heating in a pulsed mirror experiment. *Plasma Physics*, 17:679–688, 1975.

[54] Z Xie. Production of highly charged ion beams from electron cyclotron resonance ion sources (invited). *Review of Scientific Instruments*, 69(2):625–630, Jan 1998.

[55] Z Xie, CM Lyneis, RS Lam, and SA Lundgren. Enhanced ecr ion source performance with an electron gun. *Review of Scientific Instruments*, 62(3):775–778, 1991.

[56] HY Zhao, HW Zhao, LT Sun, H Wang, DZ Xie, BH Ma, XZ Zhang, XX Li, XW Ma, and YH Zhu. Effects of magnetic configuration on hot electrons in highly charged ecr plasma. *Plasma Sources Science and Technology*, 18(025021), 2009.

# Appendix A

# Diamagnetic loop

## A.1 Effect of the aluminum support ring on the diamagnetic loop signal

The electric field created by the time varying diamagnetic current will also cause a current to flow in the aluminum support ring. The current in the aluminum ring will add to the magnetic flux passing through the diamagnetic loop. In this section we propose a possible correction that can be made to the recorded signal to account for this effect.

To correct for the effect of the aluminum ring on the recorded diamagnetic loop signal a simple circuit model is used. The model, shown in Fig. A.1.1, consists of two magnetically linked circuits: one representing the copper loop and one representing the aluminum support ring. In Fig. A.1.1, $L$ is the self inductance, $R$ is the resistance, $M$ is the mutual inductance, $V_{\mathrm{Meas}}$ is the measured voltage, $\mathbf{B}_0$ is the direction of the static magnetic field, and $V_{\mathrm{P}}$ represents the electromotive force caused as the plasma forms.

Summing the voltage changes around each circuit, using the assumed current directions shown in Fig. A.1.1, and assuming that potential rises are negative, the following equations are

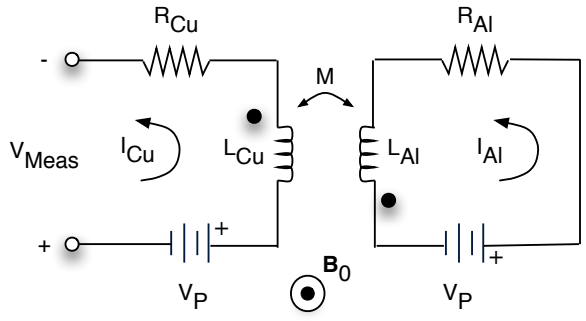


Figure A.1.1: Equivalent circuit for modeling effect of aluminum ring.

derived:

$$0 = -V_P + R_{Al} I_{Al} + L_{Al} \frac{dI_{Al}}{dt} + M \frac{dI_{Cu}}{dt}, \tag{A.1.1}$$

and

$$0 = -V_{Meas} - V_P + R_{Cu} I_{Cu} + L_{Cu} \frac{dI_{Cu}}{dt} + M \frac{dI_{Al}}{dt}. \tag{A.1.2}$$

If the plasma formation causes small induced voltages, then the currents flowing in the copper loop and the aluminum ring will be negligible, and the resistive terms in equations A.1.1 and A.1.2 can be dropped. Assuming this to be true, and using Eq. A.1.1 to eliminate $dI_{Al}/dt$, the following equation for $V_P(t)$ is derived:

$$V_P(t) = \alpha V_{Meas}(t) + \beta \frac{dI_{Cu}}{dt}, \tag{A.1.3}$$

where

$$\alpha = -\frac{1}{1 - M/L_{Al}},$$

and

$$\beta = \frac{L_{Cu} - M^2/L_{Al}}{1 - M/L_{Al}}.$$

If Eq. A.1.3 is integrated with respect to time, the following equation is obtained:

$$\int_0^\tau V_P(t)\,dt = \alpha \int_0^\tau V_{Meas}(t)\,dt + \beta \left[ I_{Cu}(\tau) - I_{Cu}(t=0) \right]. \tag{A.1.4}$$

The current in the loop is initially zero before the plasma is ignited, i.e., at time $t = 0$. At any other time, during plasma formation, the current in the loop approaches $V_{Meas}/R_{Cu}$, for simplicity, however, we assume that the current is equal to $V_{Meas}/R_{Cu}$. Making these substitutions, Eq. A.1.4 can be rewritten as:

$$\int_0^\tau V_P(t)\,dt = \alpha \int_0^\tau V_{Meas}(t)\,dt + \beta \frac{V_{Meas}(\tau)}{R_{Cu}}. \tag{A.1.5}$$

Equation A.1.5 relates the integral of the measured voltage to the integral of the induced voltage due to the plasma. Recall, from Eq. 2.1.42, that it is the latter integral that is directly relatable to the plasma energy density, and is thus the quantity of interest.

As discussed above, the formation and decay of the plasma will also induce currents in the aluminum support structure. However, if the conductivities of the loop and aluminum ring are approximately constant over the range of frequencies of interest, then the ratio of loop current to structure current will also be approximately constant, and a relative comparison of loop signals is valid. This eliminates the need to correct for the presence of the aluminum ring. As the conductivity of metals is approximately constant at frequencies below 10 GHz[26], and typical plasma formation and decay times are tens of milliseconds, the effect of the aluminum support structure on the recorded signal is neglected.

It is possible to minimize the effects of the aluminum ring physically, of course. For in-

stance, by dividing the ring into segments along a radial axis, and isolating the segments from one another with insulating material, the formation of large scale currents would be eliminated.

# Appendix B

# Xray detectors and analysis

## B.1 X-ray detectors

### B.1.1 Amptek XR-100T-CdTe detector

The XR-100T-CdTe is a semiconductor detector. Ionizing radiation interacts with the semiconductor to create electron-hole pairs. The motion of the electron-hole pairs in an applied electric field creates the current signal. For CdTe at 300 K, each electron-hole pair requires an average of 4.43 eV of energy to create. The relative smallness of the ionization energy means that a large number of electron hole pairs are generally created for each incident photon. The energy resolution of a detector is proportional to $1/\sqrt{N}$, where $N$ is the number of charge carriers, so a larger number of charge carriers leads to greater energy resolution.

The band gap of CdTe is 1.52 eV. Even at room temperature many electrons will have an energy in excess of this, and thus, they will be able to transition to the conduction band from the valence band. Because of this, when a large bias voltage is applied across the CdTe crystal, a large leakage current can appear. To counter this the CdTe crystal is actively cooled.

The actual CdTe crystal is located behind a very thin (approximately 0.01 cm) Beryllium window. This allows a detection efficiency of approximately 20% at 2 keV. A crystal thickness of 1 mm translates to a detection efficiency of, again, approximately 20% at 200 keV. Because the CdTe is placed behind a thin Beryllium window, the nose of the detector assembly must be placed in the vacuum chamber.

### B.1.2 NaI(Tl) detectors

Thallium doped sodium iodide, or NaI(Tl) detectors, like CdTe detectors, produce a pulse of electrical current whose magnitude is proportional to the detected x-ray. However, sodium iodide detectors create the electrical pulse in a different manner than CdTe detectors. When an x-ray interacts with the NaI(Tl) crystal, it produces scintillation photons through the process of fluorescence. To enhance the likely hood of producing visible radiation, impurities, such at Thallium, are introduced into the crystal. The impurities create more energy states that can be accessed by the electrons.

The scintillation photons are guided to a photomultiplier tube (PMT) where they are converted into current pulses. The PMT is typically held at high voltage (kV), and consists of two major components: the photocathode and the photomultiplier. The photocathode converts light photons into low energy electrons. The photocathode pulse is similar to the scintillation pulse. The photomultiplier amplifies the electron signal. Thermionic emission off of the photocathode results in noise in the signal. NaI(Tl) typically have lower energy resolution than semiconductor detectors[30]. A complete detector consists of the NaI(Tl) crystal, a light guide, the PMT, and supporting circuitry.

## B.2 X-ray detection and analysis

### B.2.1 Collimation and shielding considerations

Interaction of energetic electrons with ions within the plasma volume, and with any of the surrounding solid material produce these x-rays. An electron interacting with a so called thick-target, for example, the wall of the vacuum chamber, will produce a different bremsstrahlung spectra than an identical electron interacting with a thin-target, for example, the plasma in an ECRIS. Proper deconvolution of a bremsstrahlung spectrum that includes both thick and thin-target interactions becomes much more difficult. As the ultimate goal of many x-ray measurements is often to determine the electron energy distribution function of the confined electrons, the collimation system should be designed such that the radiation detector cannot "see" any solid material, e.g., the plasma chamber wall or the extraction plate. Thus, proper collimator design is paramount.

The detection of Compton scattered x-rays should also be minimized. Compton scattering of x-rays can take place in the plasma chamber walls or in the collimator system itself. A Compton scattered photon may not accurately represent the energy of the electron that emitted it. Say, for instance, a 500 keV electron exists in the plasma, and it emits a 500 keV photon while undergoing an interaction with an ion. The direction of photon emission depends on the details of the interaction. If we have a well collimated system (one that does not allow Compton scattered x-rays into the detector) the photon would have to be created in an area that is seen by the detector, and be travelling in the proper direction after creation to have a chance of discovery. If detected, we would then be able to infer that somewhere in the plasma an electron with a minimum energy of 500 keV existed. Conversely, in a poorly collimated system, a 500 keV photon, created in an arbitrary location, might first undergo scattering before finally reaching the detector with an energy of 300 keV (say). Instead of recording a photon at 500 keV, a 300 keV photon is recorded. Applying the same logic as before, the only conclusion that we can come to in this case is that there is a 300 keV electron somewhere in the plasma. Thus, a large amount of scattering can distort the true energy spectrum.

The change in energy that takes place in a Compton scattering event is given by:

$$E^{'} = \frac{E}{1 + \frac{E}{m_0 c^2}(1 - \cos\theta)}$$

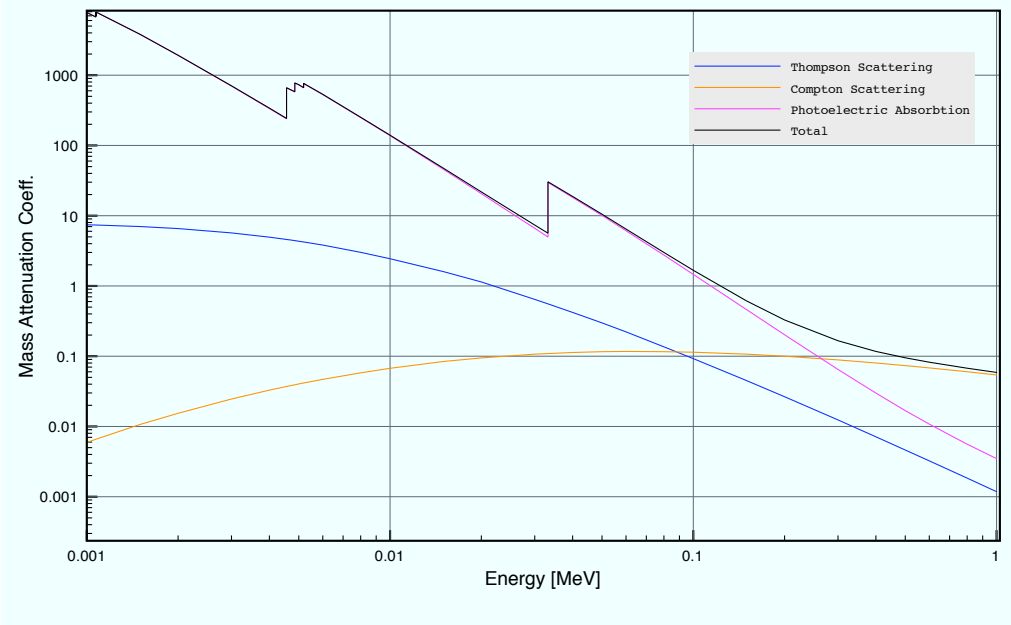


Figure B.2.1: Mass attenuation coefficient for NaI.

It is seen that, for a given energy, a larger scattering angle will cause a larger change in photon energy. We are primarily concerned, then, with limiting the number of large-angle scattered x-rays that reach the detector, as small-angle scattering will have less impact on the recorded energy spectrum. This is accomplished by placing enough material in between the plasma (x-ray source) and the detector such that most of the scattered radiation is completely attenuated.

X-rays interact with matter in three major ways: photoelectric absorption, Compton scattering, and pair production. Each of these processes tends to be dominant over certain energy ranges. Photoelectric absorption dominates in the low energy regime, pair production dominates the high energy regime (greater than 1.022 MeV), and Compton scattering bridges the gap. Recent studies involving the latest generation of ECRIS show that some photons can reach energies of over 1 MeV[34]. The total number of photons with these energies, however, is quite small. It is expected, then, that the main interaction mechanisms of the x-rays produced by ECRIS with any surrounding material, including the collimators, will be photoelectric absorption and Compton scattering.

Attenuation of x-rays in matter is characterized by the mass attenuation coefficient. It essentially takes into account all of the interaction processes mention above in order to estimate a "stopping power" of the material of interest. The mass attenuation coefficient is a function of both material and x-ray energy. An example for NaI is shown in Fig. B.2.1. The attenuation law takes the form of a simple exponential:

$$\frac{I}{I_0} = \exp\left(-\frac{\mu}{\rho}\rho t\right)$$

where $\mu/\rho$ is the mass attenuation coefficient, $\rho$ is the density of the material, and t is the

thickness of the specific piece of material. As can be seen in this equation attenuation depends on a product of density and thickness. Denser materials are much better at stopping x-rays, which is why almost all collimation systems use lead. With this equation it is easy to calculate the required thickness of material to absorb all photons below a certain energy. For instance if one wants to stop all photons with an energy less than 400 keV, a piece of copper with a thickness of around 6 cm would do.

### B.2.2 X-ray data analysis

Analysis of the x-ray spectra is done using a simple Mathematica notebook. A background spectra, taken when the ECR is not running, is subtracted from the x-ray spectra. In the case of the actively cooled CdTe detector, the background spectra is negligible compared to the x-ray spectra, even at microwave powers as low as 30 W the total background counts make up less than 1% of the total recorded counts. For the NaI(Tl) detectors, on the other hand, the background can make up a significant portion of the total counts.

Energy calibration of both the NaI(Tl) and CdTe detectors is done using a $^{207}$Bi sealed source (occasionally a $^{133}$Ba is used). For NaI(Tl) peaks at 74.9 keV, 569.7 keV, and 1063.7 keV are used. For the CdTe detector x-ray peaks at 10.6 keV, 12.6 keV, and 72.8 keV, are used. Because the energy calibration of the NaI(Tl) detectors tends to drift with ambient temperature, an energy calibration is generally taken before and after each data point. Then, an average is used for the final energy calibration. As the CdTe detector is located within the vacuum chamber, calibration is done once, before the measurements are started. Drift of the energy calibration, though, is negligible. The position of the Argon K-shell peak at 3.2 keV varied by less than 1.5% over the course of 4 weeks of measurements.

Energy calibrated spectra obtained with NaI(Tl) detectors are corrected for absorption by the quartz window separating the vacuum side from the air side. Air also absorbs some x-rays, but this effect is minimal. The spectra are not corrected for dead time losses, but the count rates when using the NaI(Tl) detectors were low, and so dead time losses should not be an issue. We also do not account for the response function of the NaI(Tl) detectors.

When using the CdTe detector, the calibrated spectra are corrected for detector efficiency[1] and dead time losses[24]. After making these corrections, the x-ray power and spectral temperature can be calculated.

To calculate the x-ray power at a particular energy the following formula is used:

$$P_{h\nu} = \frac{N_{h\nu} h\nu}{t_{acq}}, \tag{B.2.1}$$

where $N_{h\nu}$ is the number of counts a certain energy, $h\nu$ is the energy, and $t_{acq}$ is the acquisition time of the spectra. To calculate the total x-ray power in a given spectra, the power at each energy are simply summed up:

$$P_{Total} = \sum_{h\nu} P_{h\nu} = \sum_{h\nu} \frac{N_{h\nu} h\nu}{t_{acq}}. \tag{B.2.2}$$

The spectral temperature is calculated by using a linear least-squares fit to a semi-logarithmic plot of x-ray power, Eq. B.2.1, versus x-ray energy, over some predefined energy range. The inverse of this line's slope is defined as the spectral temperature. The spectral temperature and x-ray power are used as relative indicators of an ECR ion sources performance, and is not a true temperature.

# Appendix C

# Summary of time resolved, low energy x-ray experiments at JYFL

## C.1 Introduction

This appendix summarizes a portion of a set of experiments performed at the Accelerator Laboratory in the Department of Physics (JYFL), at the University of Jyvaskyla in 2010. My main interest in these experiments was to have a second set of measurements that I could compare to the diamagnetic loop measurements, and hence, the experiments that are summarized in this appendix, examined the effect that microwave power, neutral gas pressure, and magnetic field strength have on plasma bremsstrahlung production. The unique feature of these measurements is that they examine x-rays with energies as low as approximately 1 keV, and are done in a time resolved manner.

Time resolved plasma bremsstrahlung measurements allow one to qualitatively study the temporal evolution of the electron energy distribution function (EEDF) during plasma breakdown. A quantitative examination of the EEDF would require a full deconvolution of the recorded x-ray spectra, and as mentioned in an earlier chapter, may be of limited usefulness. Despite this, it is still worthwhile to compare the time resolved x-ray measurements to the plasma diamagnetic signal, as both are related to the product of electron energy and electron density.

Over the course of making the measurements it was observed that some of data seemed to compliment recent theoretical work discussing a possible explanation for the preglow peak that is sometimes observed when an ECRIS is operated in pulsed mode[25]. This finding, however, lies well outside of the scope of my dissertation, and will not be discussed.

The time resolved x-ray data acquisition was developed by T. Ropponen[42]. The other data acquisition systems were developed and implemented by physicists at JYFL. I was responsible for the design of the x-ray collimation system and providing the Amptek XR-100T-CdTe used to detect the plasma bremsstrahlung. The data included in this appendix is provided courtesy of Dr. T. Ropponen, currently of the National Superconducting Cyclotron Laboratory, at Michigan State University, and is shown as it compliments the diamagnetic loop data presented in main body of this dissertation.

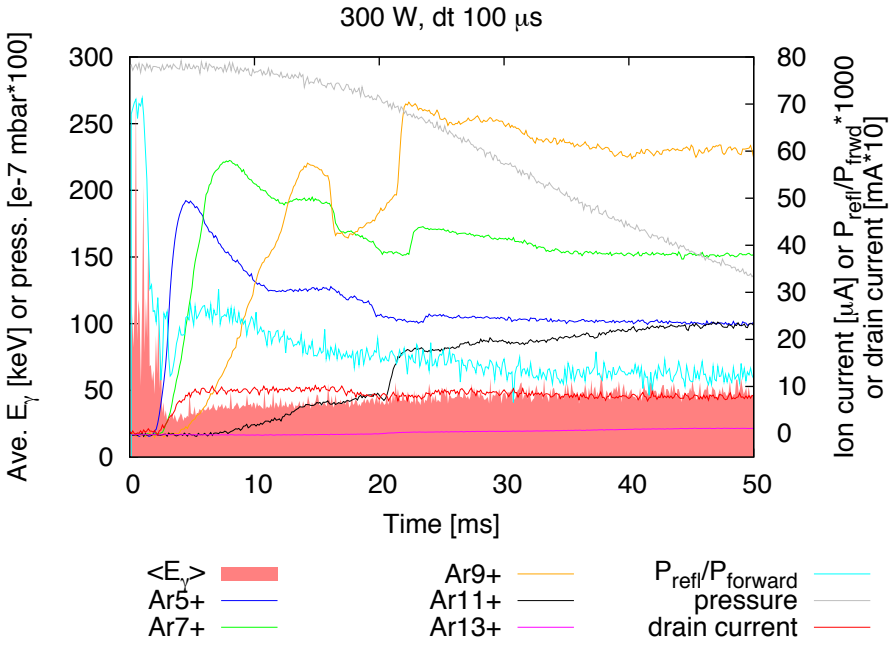


Figure C.2.1: Average detected photon energy, argon ion currents, reflected to forward microwave power, neutral pressure, and drain current as function of time at plasma ignition. Microwave power: 300 W.

Experimental data were taken on the JYFL 14 GHz ECRIS[31]. The XR-100T-CdTe detector was positioned in a radial access port of the source, and was connected to the time resolved x-ray data acquisition system. The collimation was designed to prevent the detector from seeing photons created by lost electrons striking solid surfaces. However, the shielding was not adequate, and as a result some Compton scattered photons could reach the detector. A more detailed description of the experimental setup, and results will be given in a future article by T. Ropponen *et al.*, ( to be submitted to Plasma Sources Science and Technology) entitled: "*Studies of Plasma Breakdown and Electron Heating on a 14 GHz ECR Ion Source through Measurement of Plasma Bremsstrahlung.*"

## C.2 Effect of microwave power

Figures C.2.1 to C.2.3 show the average detected photon energy, argon ion currents, reflected to forward microwave power, neutral pressure, and drain current as function of time at plasma ignition for three different microwave powers. The most interesting feature of this figure is that for all three microwave powers the average detected photon energy is high during the first approximately 3 ms, and then collapses to some final, steady state value. This behavior is repeated again and again. The timestep (temporal resolution) used in these plots is 100 $\mu$s.

Figure C.2.4 shows the the average detected photon energy over a period of 50 ms after initiation of microwave pulse. The final steady state value of average detected photon energy

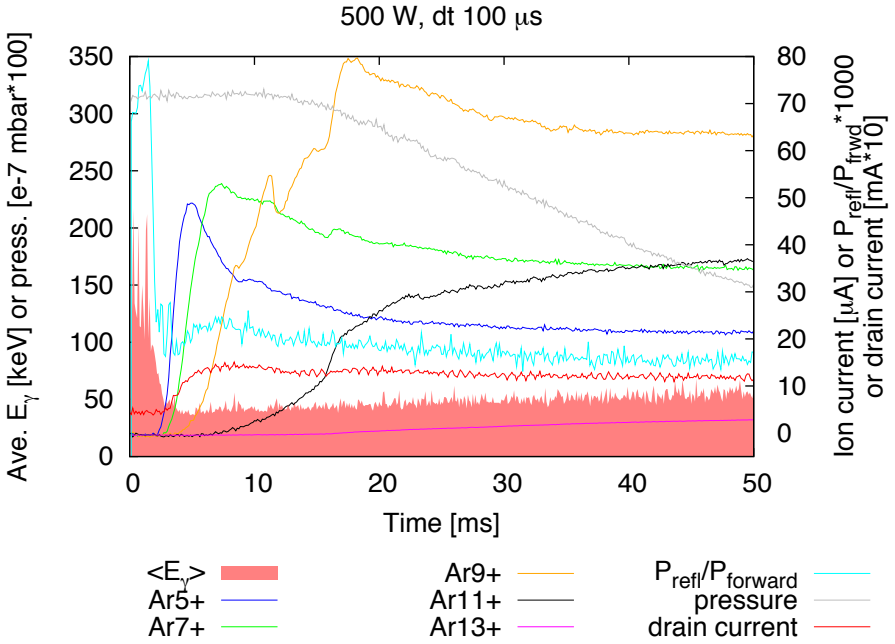


Figure C.2.2: Average detected photon energy, argon ion currents, reflected to forward microwave power, neutral pressure, and drain current as function of time at plasma ignition. Microwave power: 500 W.

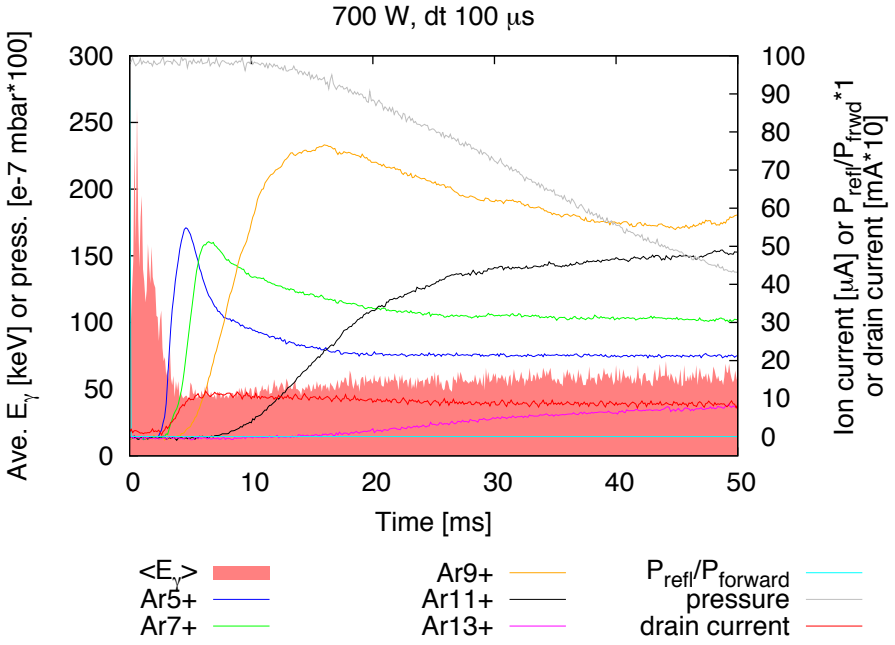


Figure C.2.3: Average detected photon energy, argon ion currents, reflected to forward microwave power, neutral pressure, and drain current as function of time at plasma ignition. Microwave power: 700 W.

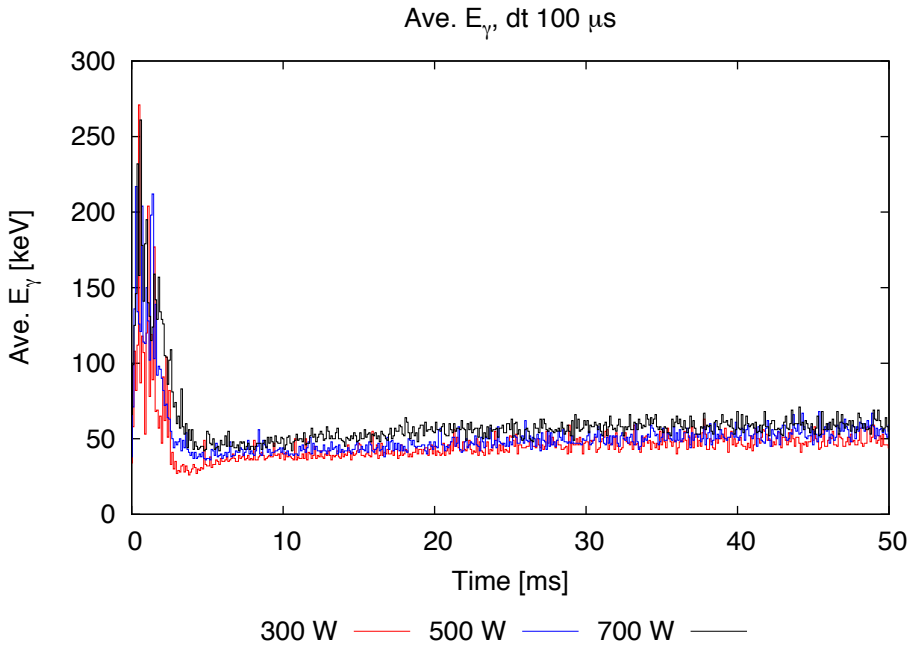


Figure C.2.4: Average detected photon energy as function of time for three different microwave powers.

is approximately equal for all three microwave powers.

Figure C.2.5 shows the relative count rate as a function of time, as measured from initiation of microwave pulse, and microwave power. It is shown that larger microwave powers produce higher count rates. The time to reach a steady state value of relative count rate, however, is insensitive to microwave power, and occurs at approximately 100 ms.

## C.3 Effect of neutral pressure

Figures C.3.1 to C.3.3 show the average detected photon energy, argon ion currents, reflected to forward microwave power, neutral pressure, and drain current as function of time at plasma ignition for three different neutral pressures. Similar to plots C.2.1 to C.2.3, the average detected photon energy is high during the first approximately 3 ms. The average energy then collapses to some final, steady state value. The timestep (temporal resolution) used in these plots is again 100 $\mu$s.

Figure C.3.4 shows the the average detected photon energy over a period of 50 ms after initiation of microwave pulse. The final steady state value of average detected photon energy is largest for the lowest neutral pressure of 1.8e-7 mbar.

Figure C.3.5 shows the relative count rate as a function of time, as measured from initiation of microwave pulse, and neutral pressure. The steady state value of relative count rate first increases as the neutral pressure is raised from 1.8e-7 mbar to 3.1 mbar, but then decreases when the neutral pressure is further increased to 4.1e-7 mbar. The time to reach a steady state

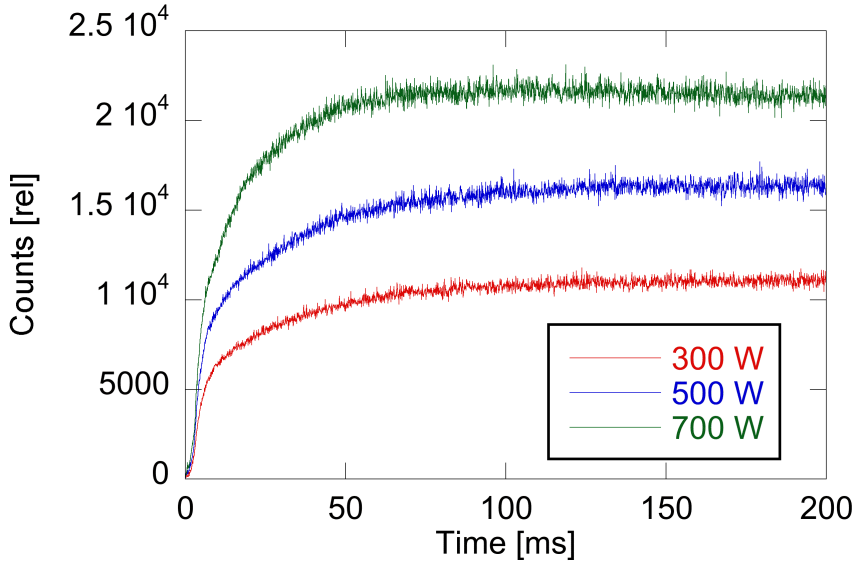


Figure C.2.5: Relative photon count rate as a function of time and microwave power.

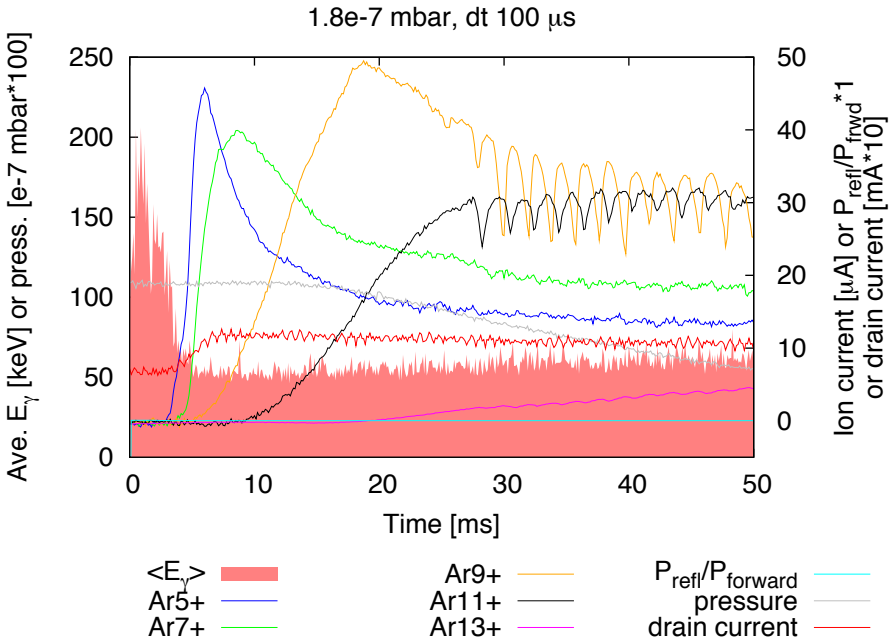


Figure C.3.1: Average detected photon energy, argon ion currents, reflected to forward microwave power, neutral pressure, and drain current as function of time at plasma ignition. Neutral pressure: 1.8e-7 mbar.

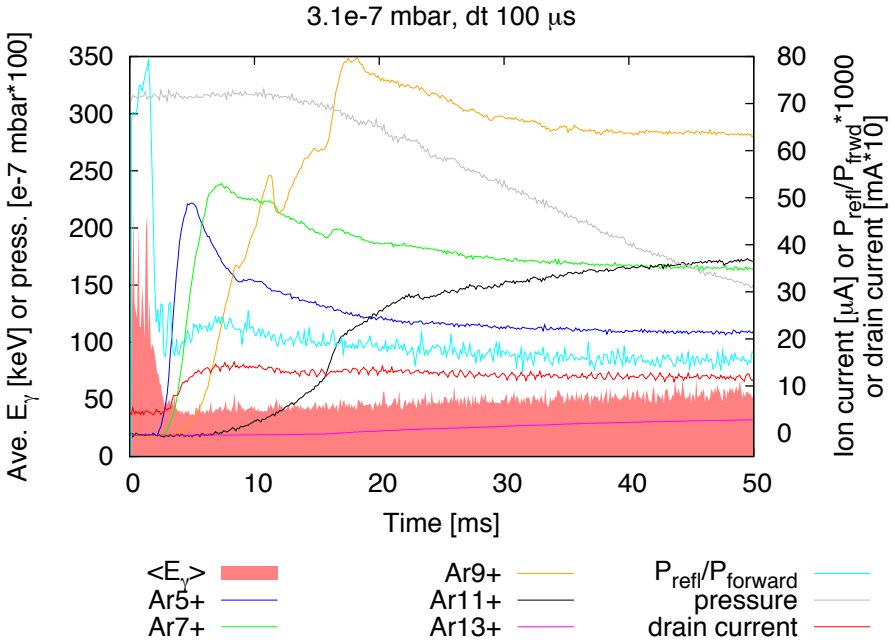


Figure C.3.2: Average detected photon energy, argon ion currents, reflected to forward microwave power, neutral pressure, and drain current as function of time at plasma ignition. Neutral pressure: 3.1e-7 mbar.

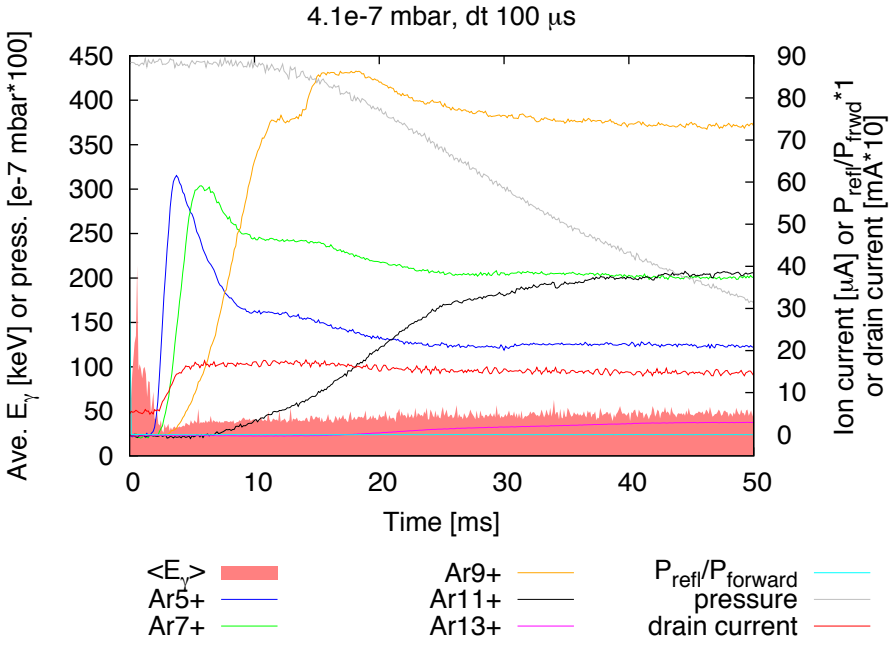


Figure C.3.3: Average detected photon energy, argon ion currents, reflected to forward microwave power, neutral pressure, and drain current as function of time at plasma ignition. Neutral pressure: 4.1e-7 mbar.

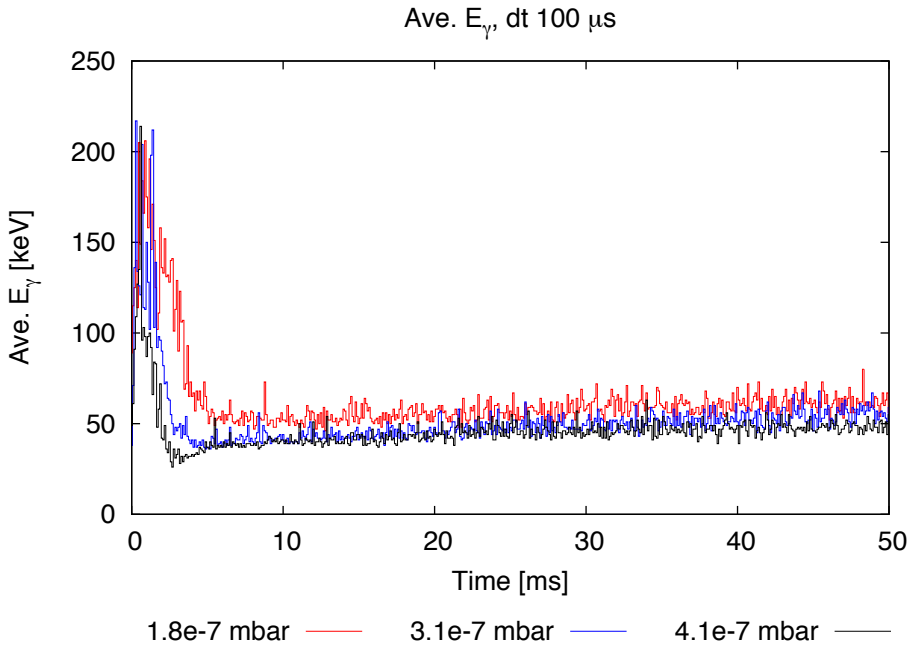


Figure C.3.4: Average detected photon energy as function of time for three different neutral pressures.

| Coil current [A] | $B_{inj}/B_{ext}/B_{min}$ [T] | $\nabla B^{res}{}_{inj}/\nabla B^{res}{}_{ext}$ [T/m] | $D_{res}$ [mm] |
|---|---|---|---|
| 470/470 | 1.95/0.9/0.32 | 6.2/5.8 | 121 |
| 500/500 | 2.01/0.95/0.35 | 5.9/5.5 | 111 |
| 550/550 | 2.11/1.02/0.39 | 5.1/4.9 | 92 |

Table C.1: Summary of magnetic field settings.

value of relative count rate is insensitive to neutral pressure.

## C.4 Effect of magnetic field configuration

Figures C.4.1 to C.4.3 show the average detected photon energy, argon ion currents, reflected to forward microwave power, neutral pressure, and drain current as function of time at plasma ignition for three different solenoid current strengths. As in the previous sections the average detected photon energy is high during the first approximately 3 ms. The average energy then collapses to some final, steady state value. The timestep (temporal resolution) used in these plots is once again 100 $\mu$s. Table C.1 provides a summary of the magnetic fields used in this set of experiments. $D_{res}$ is the axial distance between resonance points.

Figure C.4.4 shows the the average detected photon energy over a period of 50 ms after initiation of microwave pulse. The final steady state value of average detected photon energy is largest for a coil current of 550 A, and increases with solenoid current strength.

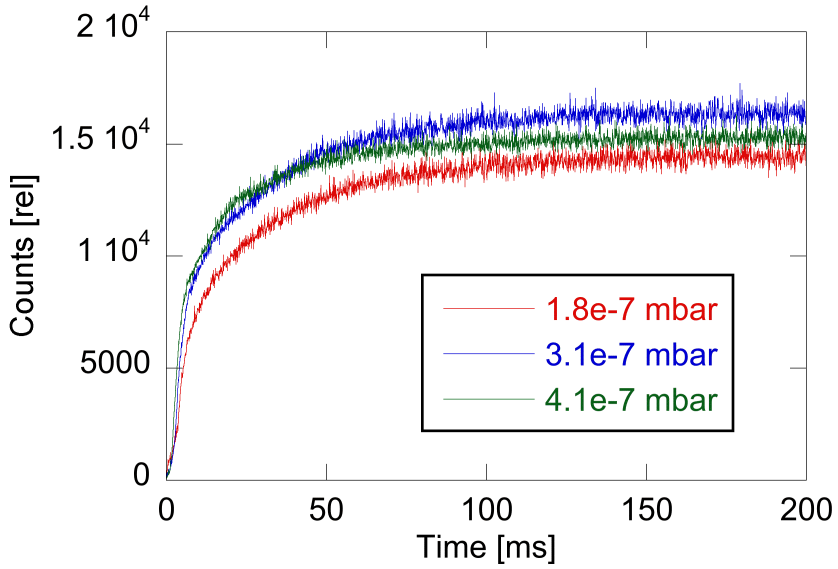


Figure C.3.5: Relative photon count rate as a function of time and neutral pressure.

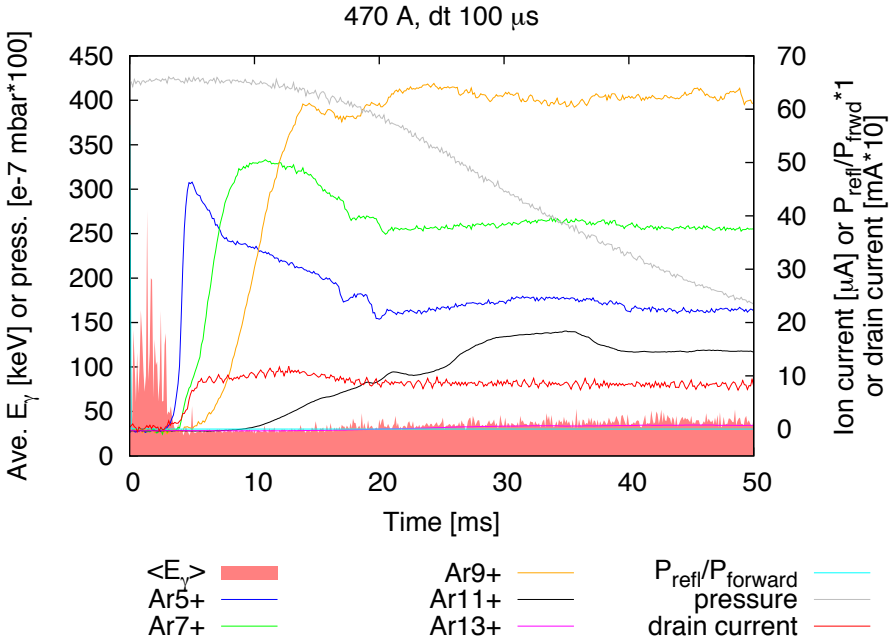


Figure C.4.1: Average detected photon energy, argon ion currents, reflected to forward microwave power, neutral pressure, and drain current as function of time at plasma ignition. Solenoid current: 470 A.

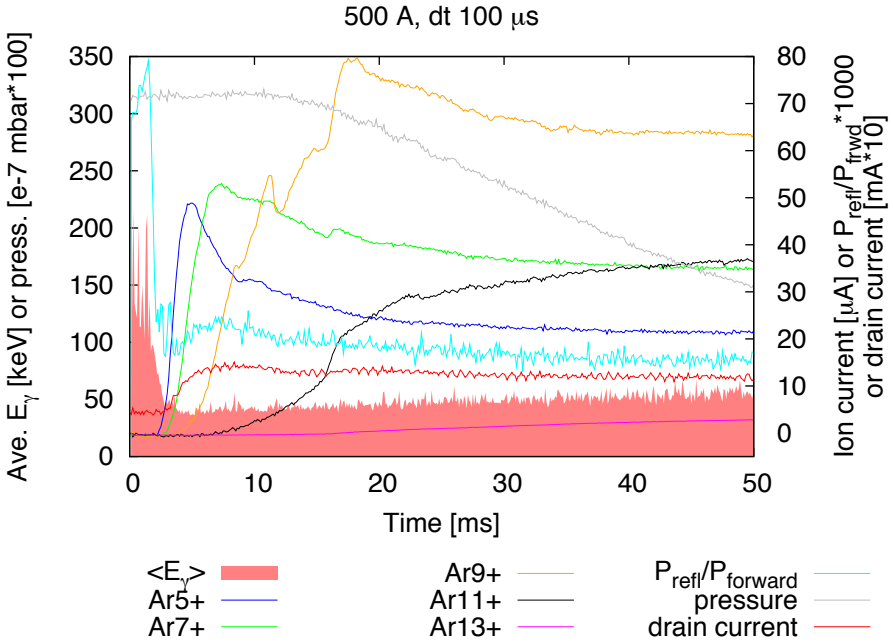


Figure C.4.2: Average detected photon energy, argon ion currents, reflected to forward microwave power, neutral pressure, and drain current as function of time at plasma ignition. Solenoid current: 500 A.

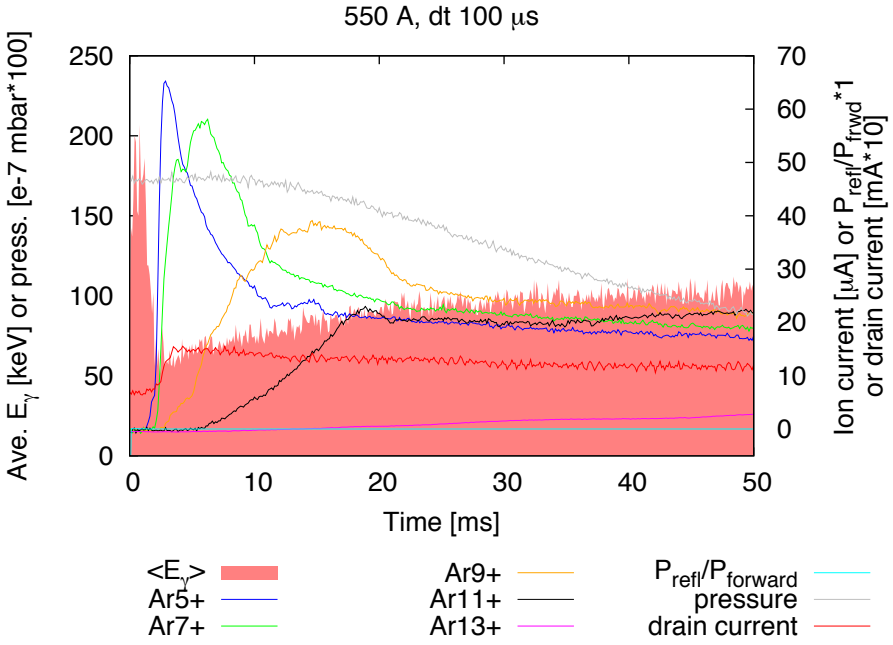


Figure C.4.3: Average detected photon energy, argon ion currents, reflected to forward microwave power, neutral pressure, and drain current as function of time at plasma ignition. Solenoid current: 550 A.

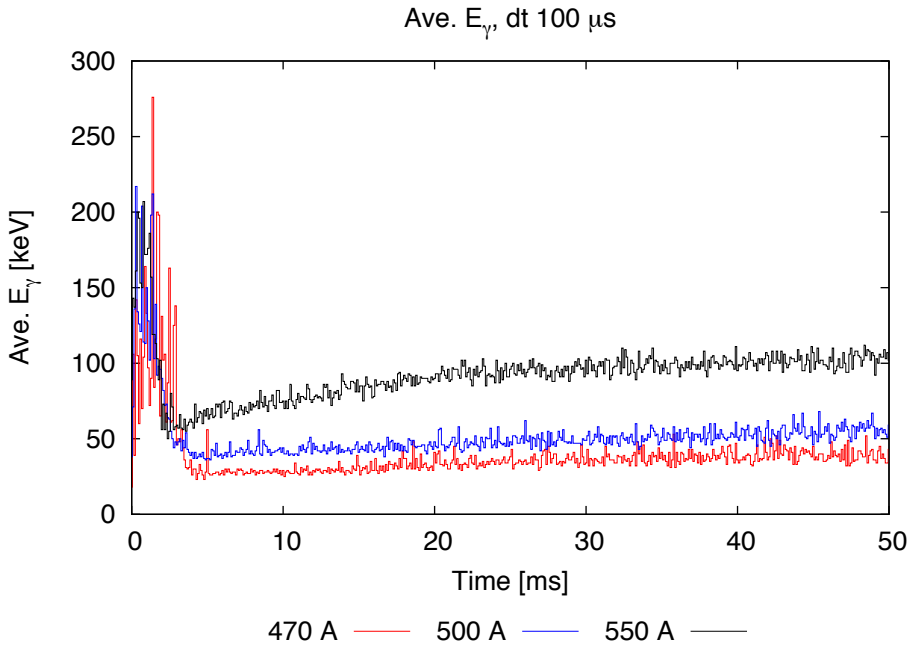


Figure C.4.4: Average detected photon energy as function of time for three different magnetic field settings.

Figure C.4.5 shows the relative count rate as a function of time, as measured from initiation of microwave pulse, and solenoid current strength. The steady state value of relative count rate is seen to increase with coil current strength. The time to reach a steady state value of relative count rate is also seen be relatively insensitive to the strength of coil current below 500 A (reaching steady state between 50 to 100 ms). At 550 A, however, the relative count rate appears to still be increasing at 200 ms.

## C.5 Effect of source tune on bremsstrahlung production

For this experiment the ion source was tuned to optimize the extracted current of different argon charge states, in particular: Ar $5^+$, Ar $9^+$, and Ar $14^+$. Figure C.5.1 indicates that the the x-ray spectra shifts to higher energies as the charge state distribution is shifted higher. Similar evidence indicating the link between x-ray energies and charge state distribution is shown in Appendix D. It is also interesting to point out that the high energy electrons (we infer that there are high energy electrons present based on the x-ray data), which do not contribute to the ionization of argon atoms in a significant manner because of the rapidly diminishing ionization cross sections, seem to be necessary to produce very high charge state ions.

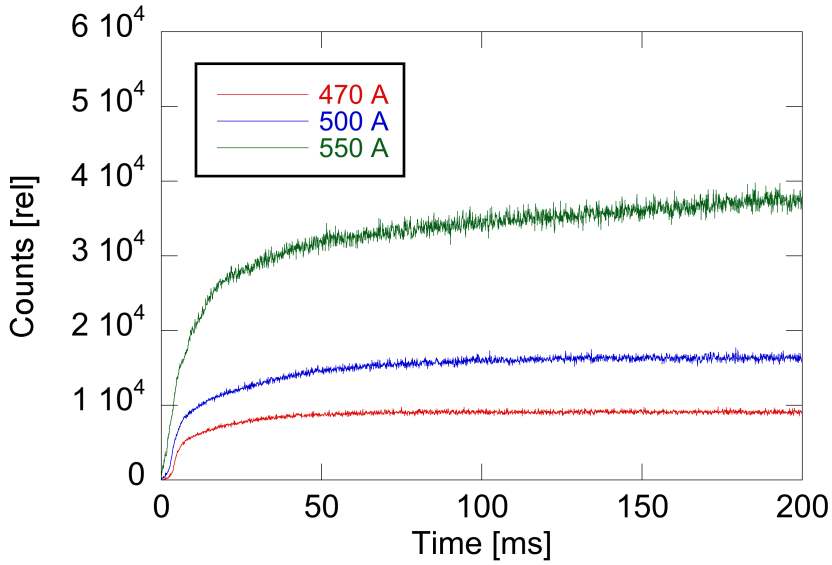


Figure C.4.5: Relative photon count rate as a function of time and coil current strength.

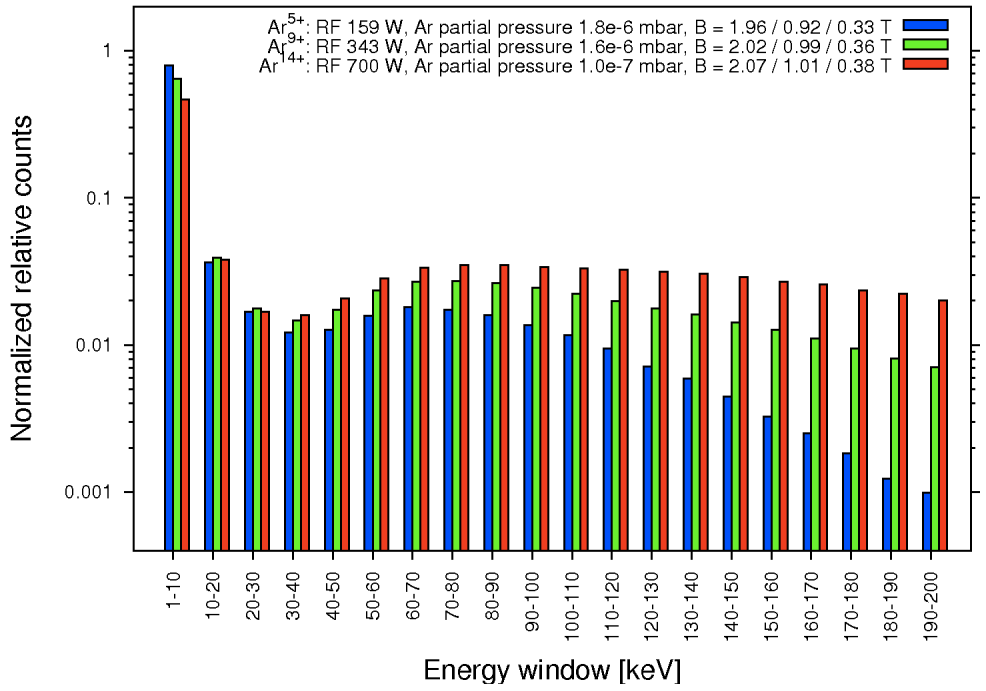


Figure C.5.1: X-ray count rates in 10 keV bins for three different ion source tunes: Ar $5^+$, Ar $9^+$, and Ar $14^+$. Count rates are normalized with respect of the total count rate for each ion source tune.

# Appendix D

# Miscellaneous data

This appendix includes both low energy and high energy x-ray data taken on the 6.4 GHz ECR and the 14.3 GHz AECR-U. It is included as it may be useful to future researchers, however it did not fit into the framework of the dissertation.

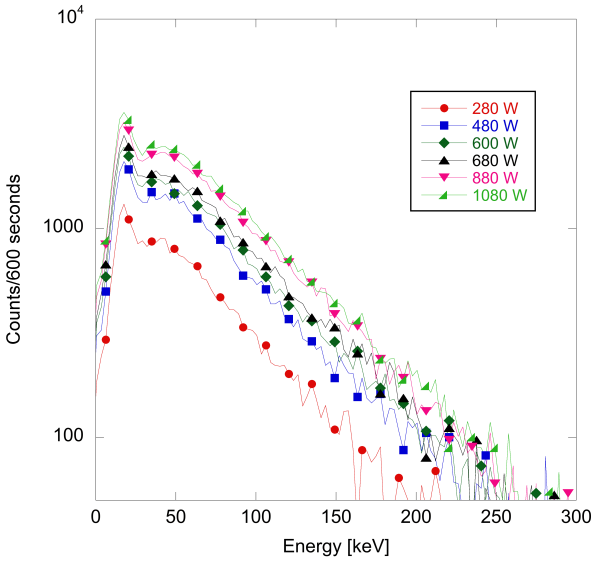


(a) Recorded radial x-ray spectra.

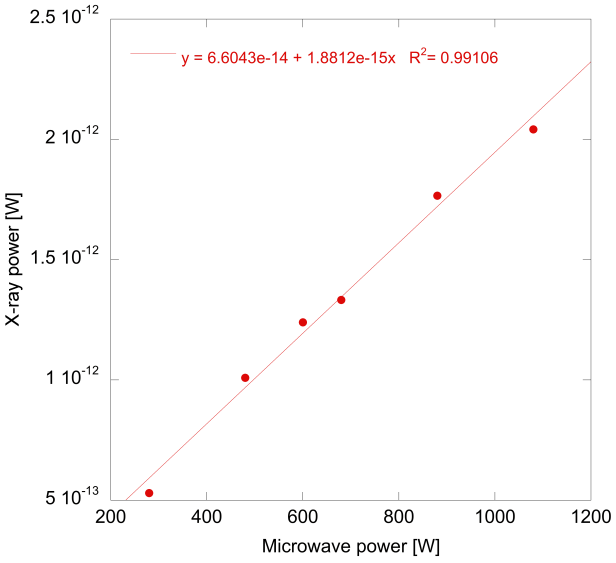


(b) Detected x-ray power.

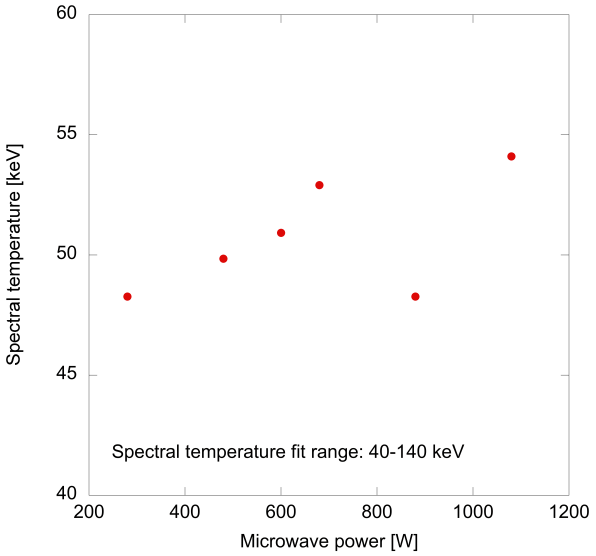


(c) Spectral temperature.

Figure D.0.1: Radial x-ray data taken on AECR-U with NaI(Tl) detector as function of microwave power. Argon/Oxygen plasma. Source tuned to peak on Argon $9^{+}$. Neutral pressure: $9.0 \times 10^{-8}$ Torr. Injection magnet currents [A]: 423/423/415. Extraction magnet currents [A]: 379/379/382.

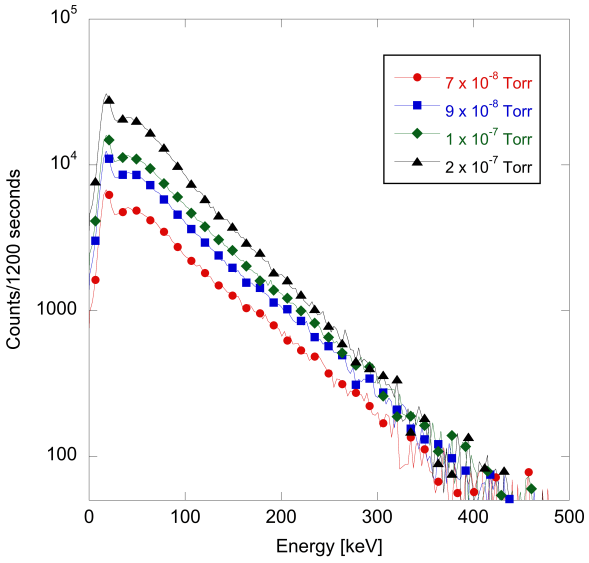


(a) Recorded radial x-ray spectra.

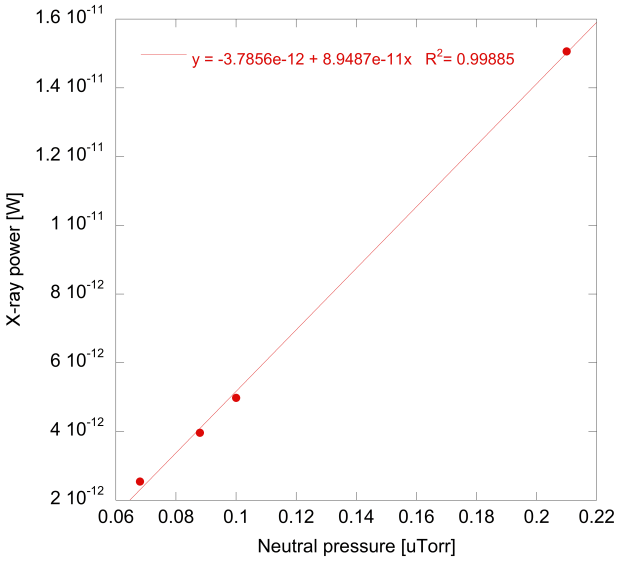


(b) Detected x-ray power.

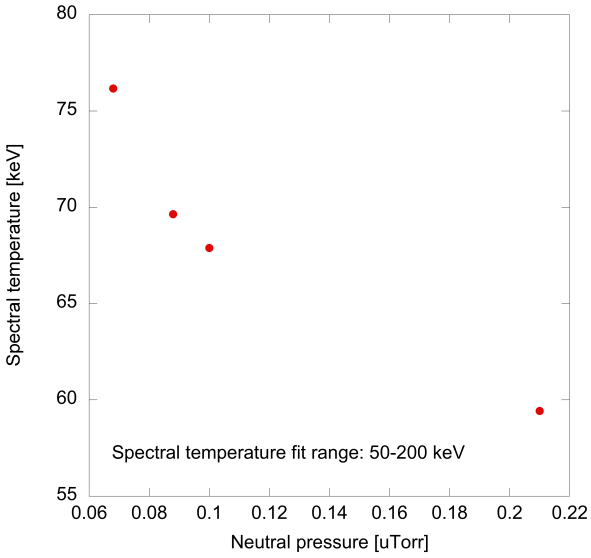


(c) Spectral temperature.

Figure D.0.2: Radial x-ray data taken on AECR-U with NaI(Tl) detector as function of neutral pressure. Argon/Oxygen plasma. 14.3 GHz power: 1000 W. Injection magnet currents [A]: 450/455/442. Extraction magnet currents [A]: 427/427/428.

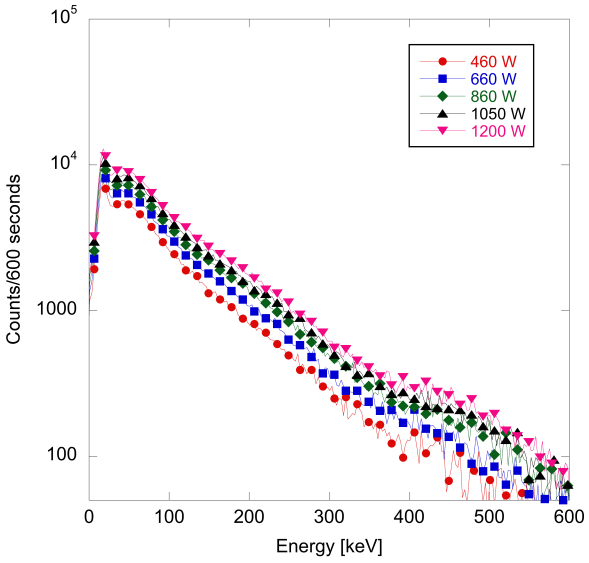


(a) Recorded radial x-ray spectra.

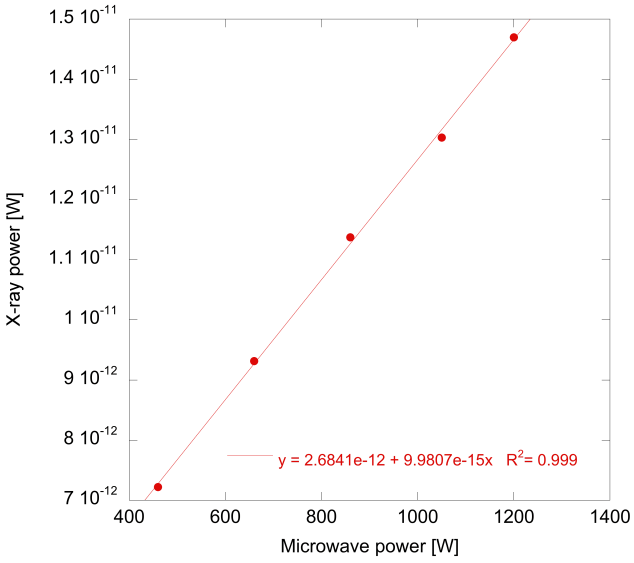


(b) Detected x-ray power.

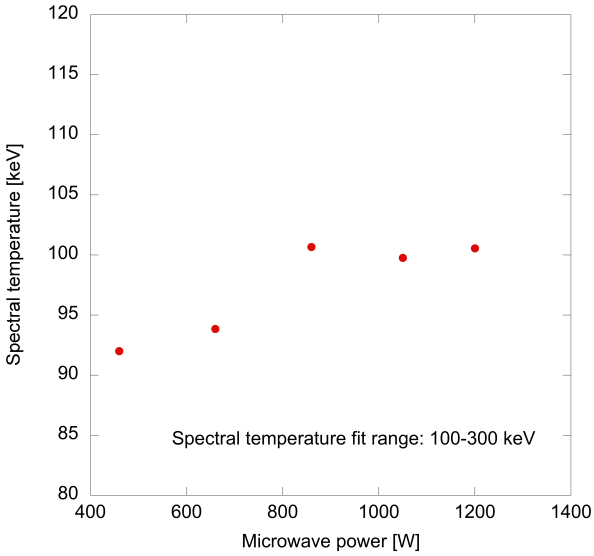


(c) Spectral temperature.

Figure D.0.3: Radial x-ray data taken on AECR-U with NaI(Tl) detector as function of microwave power. Argon/Oxygen plasma. Source tuned to peak on Argon $12^{+}$. Neutral pressure: $9.0 \times 10^{-8}$ Torr. TWTA 12.33 power: 260 W. Injection magnet currents [A]: 492/497/486. Extraction magnet currents [A]: 483/484/483.

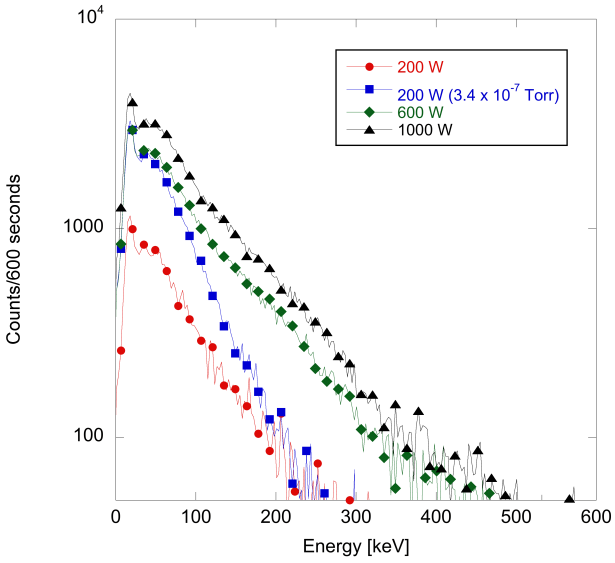


(a) Recorded radial x-ray spectra.

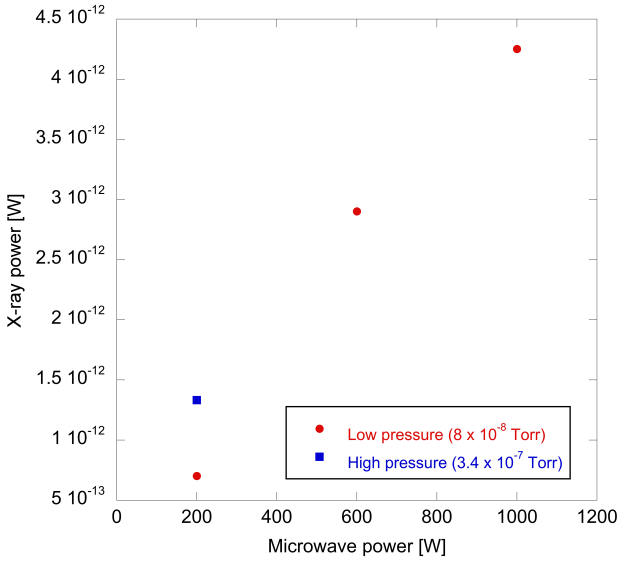


(b) Detected x-ray power.

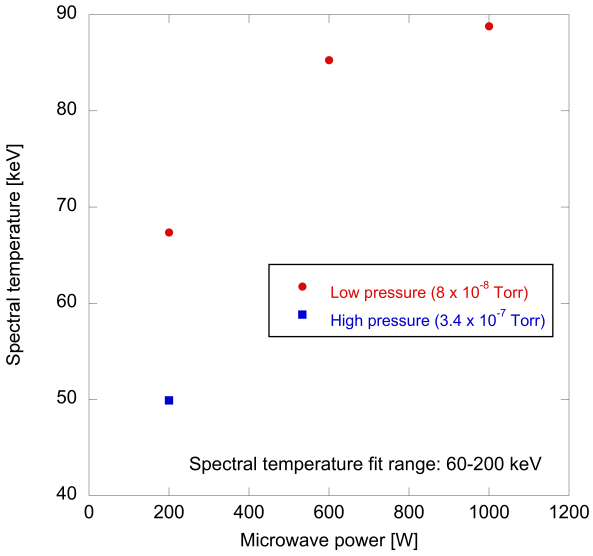


(c) Spectral temperature.

Figure D.0.4: Radial x-ray data taken on AECR-U with NaI(Tl) detector as function of microwave power and neutral pressure. Oxygen plasma. Neutral pressure: $8.0 \times 10^{-8}$ Torr. Low pressure injection magnet currents [A]: 450/450/450. Low pressure extraction magnet currents [A]: 500/500/500. High pressure injection magnet currents [A]: 520/520/520. High pressure extraction magnet currents [A]: 475/475/475.

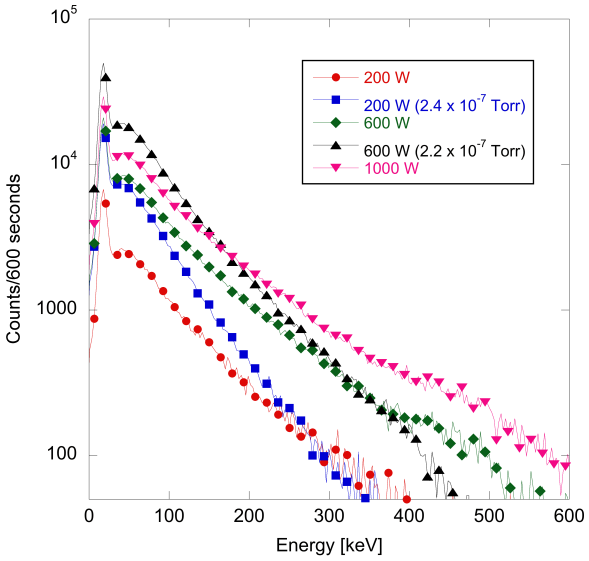


(a) Recorded radial x-ray spectra.

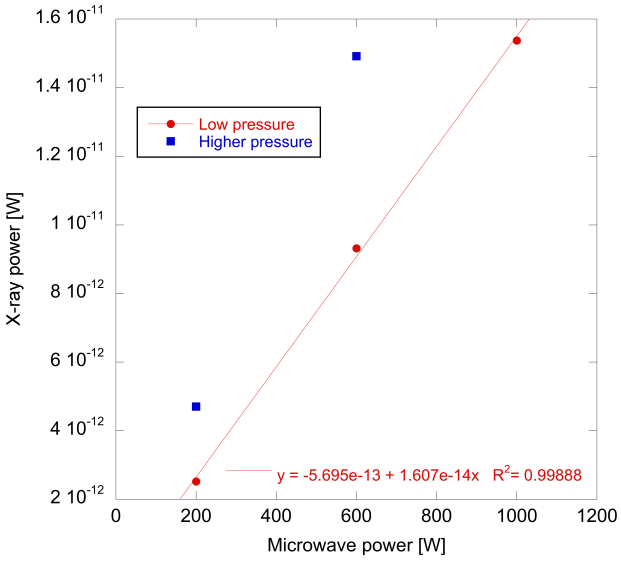


(b) Detected x-ray power.

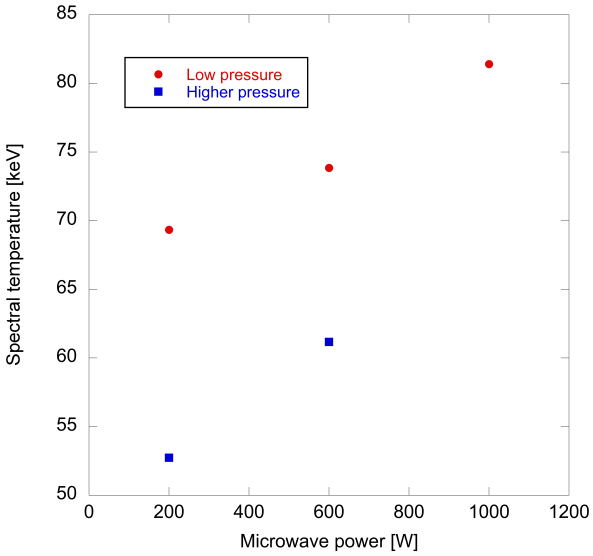


(c) Spectral temperature.

Figure D.0.5: Radial x-ray data taken on AECR-U with NaI(Tl) detector as function of microwave power and neutral pressure. Xenon plasma. Neutral pressure: $1 \times 10^{-7}$ Torr. Low pressure injection magnet currents [A]: 520/520/520. Low pressure extraction magnet currents [A]: 475/475/475. High pressure injection magnet currents [A]: 518/518/518. High pressure extraction magnet currents [A]: 442/442/445.

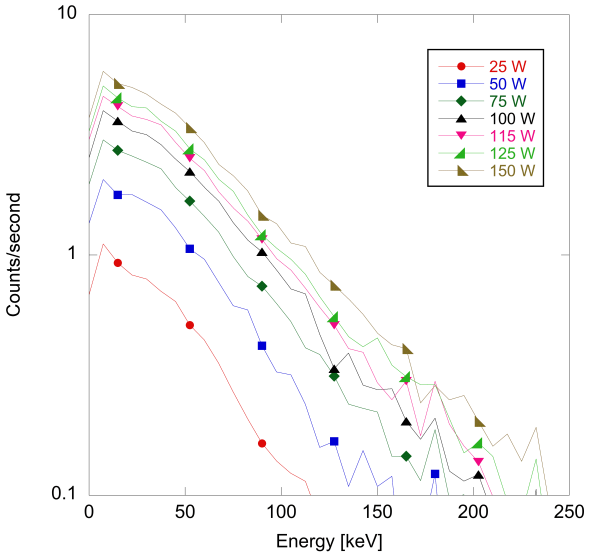


(a) Recorded radial x-ray spectra.

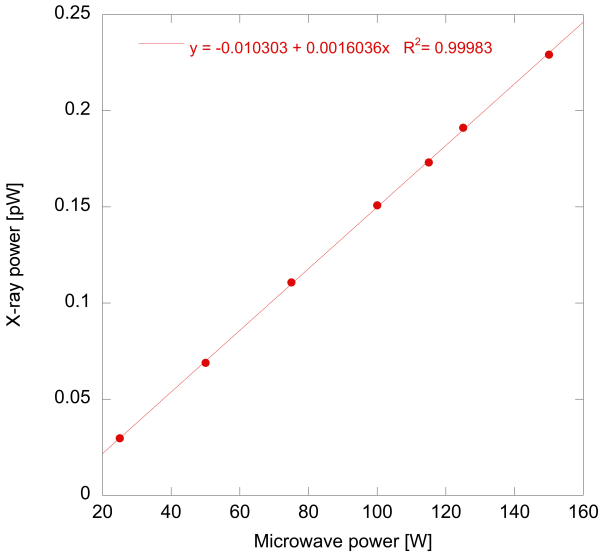


(b) Detected x-ray power.

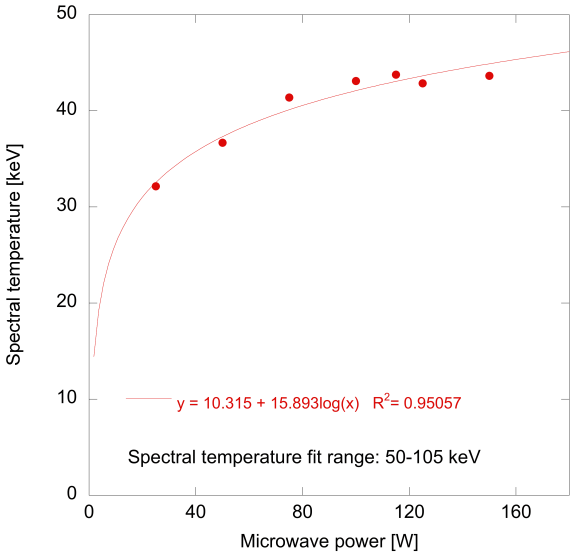


(c) Spectral temperature.

Figure D.0.6: Radial x-ray data taken on AECR-U with NaI(Tl) detector as function of microwave power. Oxygen plasma. Neutral pressure: $3 \times 10^{-7}$ Torr. Injection magnet currents [A]: 491/491/491. Extraction magnet currents [A]: 469/469/471.

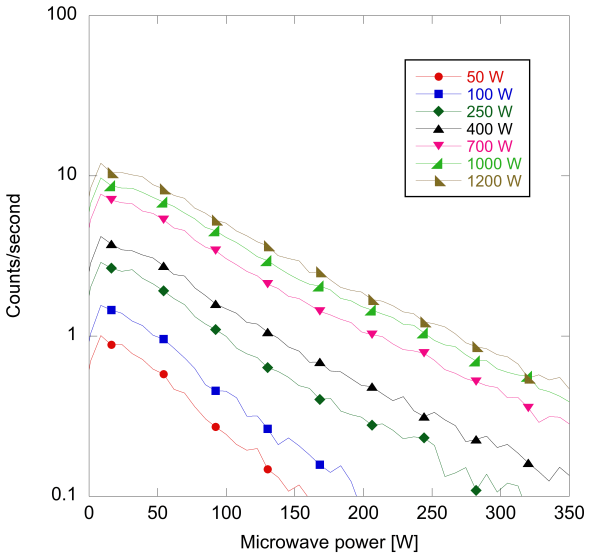


(a) Recorded radial x-ray spectra.

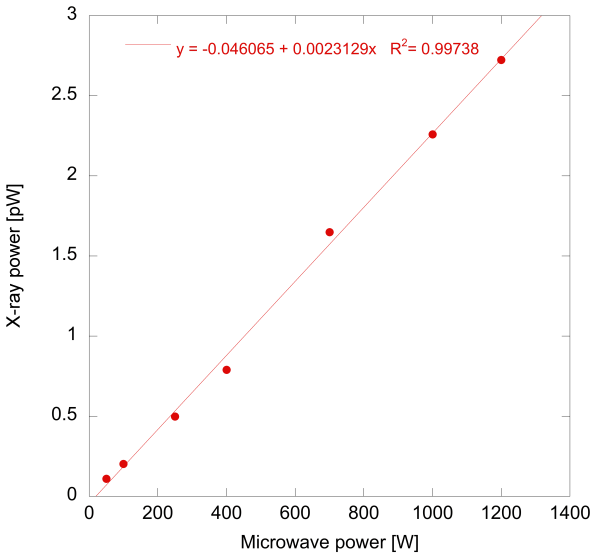


(b) Detected x-ray power.

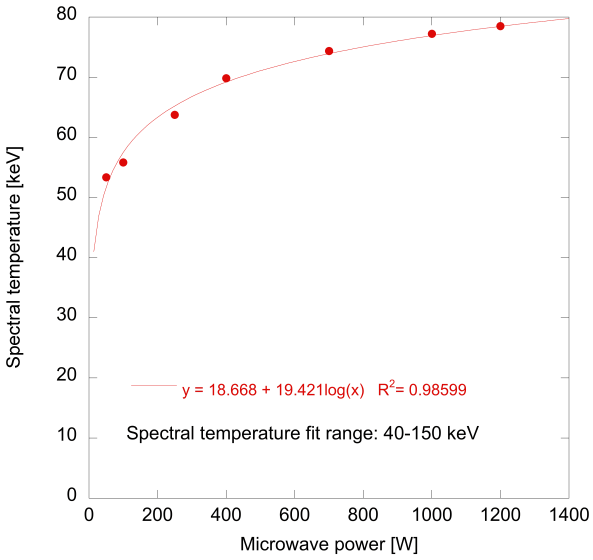


(c) Spectral temperature.

Figure D.0.7: Radial x-ray data taken on AECR-U with NaI(Tl) detector as function of microwave power. Oxygen plasma. Neutral pressure: $8 \times 10^{-8}$-$1 \times 10^{-7}$ Torr. Injection magnet currents [A]: 490/490/490. Extraction magnet currents [A]: 469/469/471.

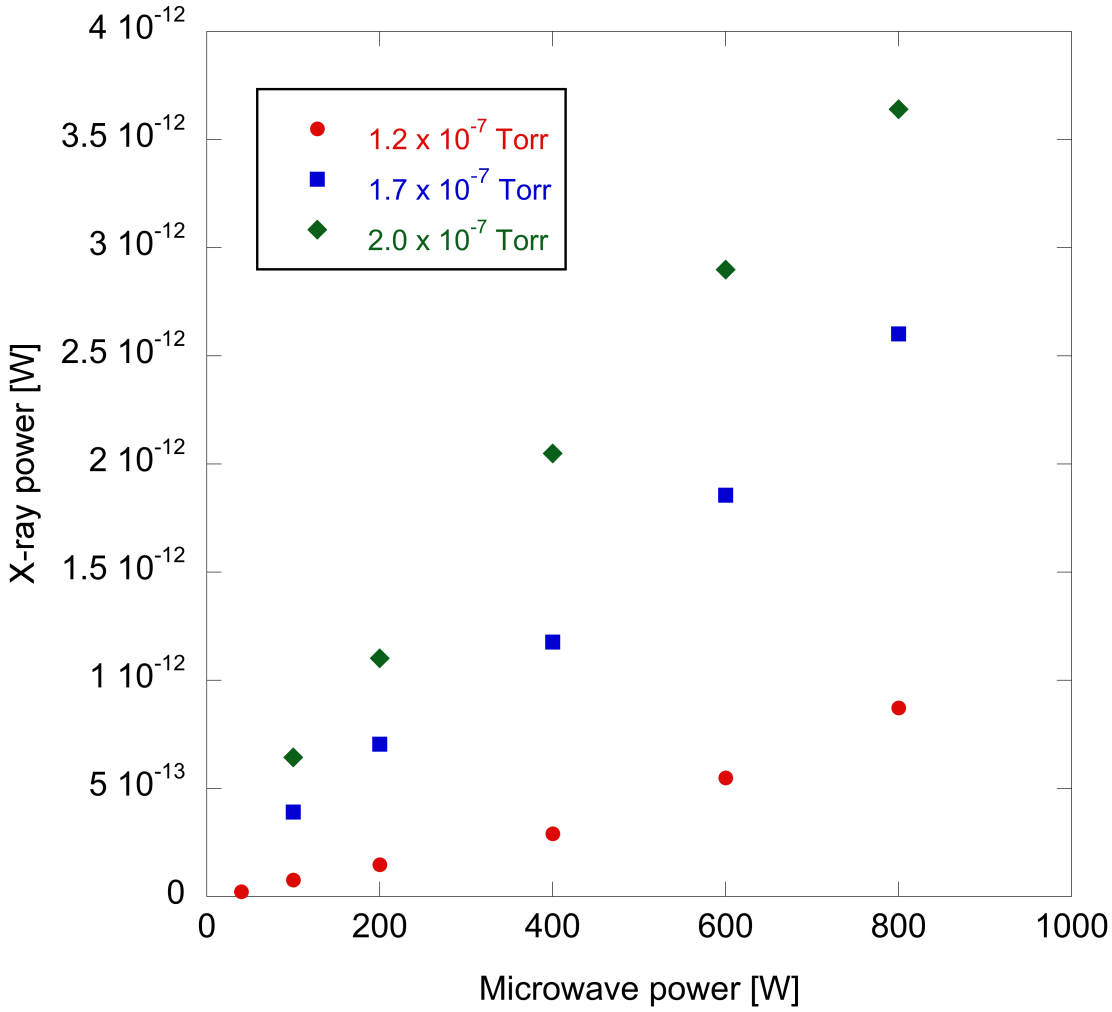


Figure D.0.8: Radial low energy (< 70 keV) x-ray power taken on AECR-U with Amptek CdTe detector as function of microwave power and neutral pressure. Argon plasma. Injection magnet currents [A]: 444/445/445. Extraction magnet currents [A]: 441/439/439. X-ray power does not saturate with microwave power, however shielding was not sufficient to block Compton scattered x-rays from reaching the detector.

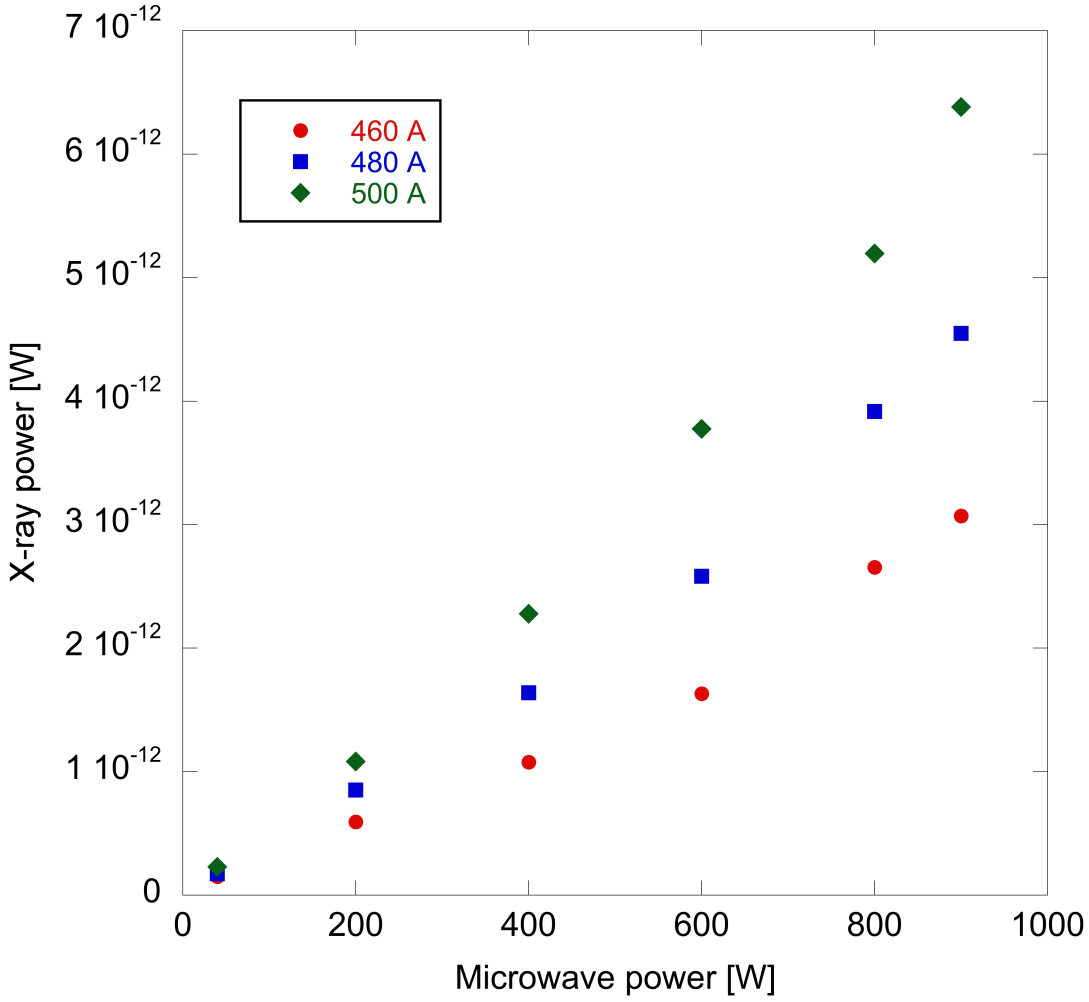


Figure D.0.9: Radial low energy (< 70 keV) x-ray power taken on AECR-U with Amptek CdTe detector as function of microwave power and magnetic field strength. Coil currents were set equal (460 A means that 460 A was used in all six coils). Argon plasma. Neutral pressure: $1.5 \times 10^{-7}$-$2.2 \times 10^{-7}$ Torr. Shielding was not sufficient to block Compton scattered x-rays from reaching the detector.